

1

2

π^+ Cross Section on Argon for the LArIAT Experiment

3

A Dissertation Submitted to the

4

College of Arts and Sciences

5

of Syracuse University

6

in partial fulfillment of the

7

requirements for the degree of

8

DOCTORATE OF PHILOSOPHY (Ph.D.)

9

2019

10

by Gregory Pulliam

11

B.S., University of North Carolina-Chapel Hill, 2012

12

M.S., Syracuse University, 2015

13

Committee Chair: Professor Mitchell Soderberg

14

© 2019

15

All Rights Reserved

Abstract

17 LArIAT (Liquid Argon in a Testbeam) was a LArTPC experiment exposed to a charged-particle
18 beam at the test-beam facility at Fermi National Accelerator Laboratory. This analysis measures
19 the π^+ -Ar cross section over an interacting energy range of 50-1100 MeV, accounting for background
20 species and reconstruction effects. This is the first such measurement of this process. The result
21 can be useful in tuning simulations for future liquid argon experiments such as DUNE and SBN.

22 Acknowledgements

23 Any analysis is a collaborative effort. Not only have I relied on research colleagues to bring updates
24 or improvements to the analysis, but also on family and friends for support when things become
25 difficult. Though by no means an exhaustive list, there are those I would like to thank for their
26 help in getting me to where I am today.

27 First, I wish to thank my parents for all of their support. Their sacrifices that allowed me the
28 opportunity to attend university and then graduate school were immense, and I wouldn't be where
29 I am without all they've done. Even in recent weeks, when I struggled to see the light at the end of
30 the tunnel, their support and optimism was comforting, and gave me the strength to push forward
31 and finish. This is as much their accomplishment as it is mine.

32 To my advisor, Mitch Soderberg, thanks for taking a chance on me and allowing me to work for
33 you, for the support when I needed extra guidance, for trusting me to work independently when I
34 felt like I knew what I was doing, and for providing some sense of grounding in the final weeks when
35 there seemed to be too much to do and too little time to do it. For my postdoc, Pip Hamilton,
36 thanks for being a "rubber ducky" and letting me explain to you what I was doing from time
37 to time, just so I could prove to myself I wasn't doing something dumb, as well as the US-UK
38 political discussion, random owl memes, and the ASCII troll art that reminded me every hour that
39 "Britannia Rules the Waves".

40 To Elena Gramellini, my work wife, thank for you for showing me how this analysis should be
41 done by graduating first and forging a path I could follow when our analyses dovetailed. Becoming
42 a better scientist means learning from people who are smarter than you. From you, I learned a
43 lot, which made the Imposter Syndrome a little less. To my spokespeople, Jen Raaf and Jonathan
44 Asaadi, thank you for not only your excellent leadership of LArIAT, but also for challenging me

45 to improve this analysis while supporting me when the paranoia and stress kicked in and I was
46 pulling out my non-existent hair. To the rest of LArIAT, thank you for all of your contributions.
47 These analyses are a group effort, and I've relied on all of you multiple times when I wasn't as
48 knowledgeable on a topic. Next time though, fewer ponies.

49 To my closest friends: Tyler, Matt, Angel and Zach, you've made Chicago feel like home, and
50 provided me a second family. You guys have been there whenever I needed you, even if that meant
51 midnight rants with a bottle of wine or providing a welcomed weekend distraction as a respite from
52 the stress. Finally, to my boyfriend, Mike. You've supported me for the last 3 years, during the
53 paranoia, panic attacks, and sleep-deprived irritability. Thank you so much for staying with me on
54 this journey, and wherever the adventure takes us next.

Contents

56	Acknowledgements	3
57	1 Theory	5
58	1.1 The Particle Zoo	5
59	1.2 Neutrinos and Beyond Standard Model Phenomena	8
60	1.2.1 Neutrino Oscillations	8
61	1.2.2 Other Open Questions	10
62	1.3 Neutrino Interactions	13
63	1.4 Pion Cross Sections and Understanding Neutrino Interactions	14
64	1.4.1 Pion Interactions Considered for Cross Section	16
65	2 LArTPC	21
66	2.1 Time Projection Chambers Using Liquid Argon	21
67	2.2 LArTPC Operational Concept	22
68	2.3 Energy Deposition and Screening Effects	25
69	2.3.1 Ionization Charge	25
70	2.3.2 Scintillation Light	30
71	2.4 Event Reconstruction	34
72	2.4.1 Deconvolution	34

73	2.4.2	Hit Reconstruction	34
74	2.4.3	Clustering	36
75	2.4.4	3D Track Reconstruction	37
76	2.4.5	Calorimetry	37
77	3	The LArIAT Experiment	39
78	3.1	Fermilab Test Beam Facility	39
79	3.1.1	Accelerator Beam Conditions	41
80	3.2	LArIAT Auxiliary Detectors	42
81	3.2.1	Time of Flight	42
82	3.2.2	Wire Chambers and Bending Magnets	43
83	3.3	Cryogenic System	44
84	3.3.1	Cryostat	44
85	3.3.2	Liquid Argon Purification System	47
86	3.4	LArIAT Time Projection Chamber	47
87	3.4.1	Cathode Voltage and Field Cage	47
88	3.4.2	Anode Wire Planes	49
89	3.4.3	TPC Readout	50
90	3.4.4	Light Collection Systems	51
91	3.5	Trigger Conditions	53
92	4	Reconstruction Methods	55
93	4.1	TOF Reconstruction	55
94	4.1.1	Hit Matching Within a TOF Paddle	55
95	4.1.2	Calculating The Time of Flight	57

96	4.2	Wire Chamber Reconstruction	58
97	4.2.1	Wire Chamber Hit Finding	59
98	4.2.2	Wire Chamber Track Building	60
99	4.2.3	Four Point Track Reconstruction	60
100	4.2.4	Quality Cuts on 4 Point Tracks: Aperture Cuts and Track Extrapolations . .	64
101	4.2.5	Three Point Track Reconstruction	65
102	4.2.6	Three Point Calibration	66
103	5	Pion Event Selection	73
104	5.1	Charge Selection, and TOF/WCTrack Existence	73
105	5.2	Mass Hypothesis	74
106	5.3	Wire Chamber Quality Cuts	75
107	5.4	TPC Quality Cuts	75
108	5.5	WC To TPC Match	77
109	5.6	Shower Filter	78
110	5.6.1	Cone Dimensions and Orientation	78
111	5.6.2	Tuning Shower Filter in Simulation	81
112	5.7	Proton Filter	83
113	6	Simulation	89
114	6.1	Data-Driven Monte Carlo	89
115	6.1.1	Simulation of Pileup	92
116	6.2	Beamline Material Energy Loss	93
117	6.3	Beamline Composition	97
118	6.3.1	Simulation Geometry, Spill Creation and Trigger Finding	97

119	6.3.2	WC Tracking and TOF Reconstruction	100
120	6.4	Beamline Composition Analysis	103
121	6.4.1	Four Point Analysis	103
122	6.4.2	Three Point Analysis	114
123	6.5	Selection of DDMC Events	115
124	6.6	Proton Contamination Comparison Between Data and DDMC	120
125	7	Cross Section Analysis	123
126	7.1	Thin Slice Method	123
127	7.2	Calculation of Energy for a Given Slice	124
128	7.3	Underlying Data and MC Plots	125
129	7.3.1	$\frac{dE}{dX}$ and Pitch Comparisons	125
130	7.3.2	$\frac{dE}{dX}$ vs Residual Range Comparison	125
131	7.4	Calculating the Cross Section	127
132	7.5	Corrections to the Cross Section	129
133	7.5.1	Background Subtraction	130
134	7.5.2	Tracking Resolution and Reconstruction Efficiency	132
135	7.5.3	Angular Resolution	133
136	7.5.4	Defining Reconstruction Efficiency	136
137	7.6	Corrected Cross Section	137
138	8	Systematic Uncertainty and the Final Cross Section	141
139	8.1	Systematic Uncertainty	141
140	8.1.1	Uncertainty on Reconstructed Energy	141
141	8.1.2	Systematic on the Momentum	142

145 List of Tables

146	1.1	Table of Fermions and Their Quantum Numbers	6
147	1.2	Experimental results of neutrino mass, mixing angles, and CP violating phase	10
148	1.3	Example Topologies of Pion Interactions	18
149	2.1	LAr vs LXe properties	23
150	3.1	Voltages for Cathode and Wire Planes by Run Period	50
151	4.1	Parameters for Three Point Track Calibration	71
152	5.1	Data Event Reduction Table	87
153	6.1	Material Budget Between WC	96
154	6.2	Fit Parameters for TOF Accidentals	109
155	6.3	Event Reduction Table for +60 A DDMC	120
156	6.4	Event Reduction Table for +100 A DDMC	121
157	8.1	Effect of 3 mm Uncertainty From WCTrack Projections on Beamline Composition .	148

List of Figures

158		
159	1.1	Experimental ν_μ and $\bar{\nu}_\mu$ Cross Sections 14
160	1.2	Experimental Pion Cross Sections on Various Nuclei 17
161	1.3	Candidate event examples of topologies considered for analysis 19
162	1.4	Geant4 Predicted Cross Section for π^+ -Ar 20
163	2.1	General Schematic of TPC 24
164	2.2	Bethe-Bloch Plot for Muons on Copper 26
165	2.3	δ -ray Event in LArIAT 27
166	2.4	Electron Lifetime During LArIAT Data Taking Operation 28
167	2.5	Light Emission Spectra of Argon, Xenon and Krypton 31
168	2.6	Flow Chart of Track Reconstruction 35
169	3.1	Simulated DUNE CC Daughter Momentum Spectra and LArIAT Data Momentum
170		Spectra 40
171	3.2	Fermilab and FTBF 41
172	3.3	Schematic of LArIAT Beamline Auxiliary Detectors and TPC 43
173	3.4	Maximum Magnetic Field for LArIAT Magnets 45
174	3.5	LArIAT Cryostat Before and After Sealing 46
175	3.6	Screenshot of LArIAT Cryogenic Monitor 48

176	3.7	Schematic of Cathode and Wire Plane Placement in TPC	49
177	3.8	Diagram of LArIAT Electronic Readout	52
178	3.9	LArIAT's Light Collection System	52
179	4.1	Example PMT Pulse in a TOF Paddle	56
180	4.2	First Derivative of TOF Pulses for Hit Finding	56
181	4.3	Hit Matching Δt for USTOF and DSTOF PMTs	57
182	4.4	All TOF Possibilities in Run II	58
183	4.5	Residual Distance For +100A WCTrack	61
184	4.6	Excitation Curve for NDB Magnet	63
185	4.7	WC Track Momentum Reconstruction: Positive Polarity Four Point High Yield Tracks	63
186	4.8	Collimator Scattering Cut Explanation	65
187	4.9	Midplane Extrapolation Cut Explanation	66
188	4.10	Midplane Projection Matching for +100 A WC Tracks	67
189	4.11	Realistic Midplane Projection	68
190	4.12	60A Three Point and Four Point Track Comparison	69
191	4.13	100A Three Point and Four Point Track Comparison	69
192	4.14	Fitting Fractional Error for Three Point Scaling Factors	70
193	4.15	Wire Chamber: Corrected Miss WC2 Fractional Error	72
194	5.1	Time of Flight vs WC Momentum and Mass Hypothesis	74
195	5.2	Midplane Matching ΔY vs ΔX after WC Quality cuts	76
196	5.3	Upstream Track Existence Cut Efficiency	76
197	5.4	Pileup Event Cut Efficiency	77
198	5.5	Wire Chamber to TPC Track Matching	79

199	5.6	WC to TPC Match: ΔY vs ΔX and α for WC to TPC Tracks	80
200	5.7	Shower Filter Cone ROI	81
201	5.8	MC Shower Filter Pass Rates For Pions and Positrons	82
202	5.9	Data Shower Filter Pass Rate	84
203	5.10	$\frac{dE}{dX}$ vs Residual Range for Pion and Proton Test Samples	85
204	5.11	Theoretical PIDA for Pions, Muons, Kaons and Protons	86
205	5.12	PIDA for Cross Section Worthy Tracks for Proton Filter	88
206	6.1	Data XY Start Position For +100 A DDMC	90
207	6.2	Data Momentum for +100 A DDMC	91
208	6.3	Data XY Start Position For +60 A DDMC	91
209	6.4	Data Momentum for +60 A DDMC	92
210	6.5	True Energy Loss Between WC4 and Active Volume of TPC	94
211	6.6	Visualization of Halo Paddle Between WC4 and the DSTOF Paddle	95
212	6.7	P_x vs x Phase Space for Halo Hitting and Missing Particles	97
213	6.8	Detector Geometry Used for G4BL Simulation	98
214	6.9	Comparison of Data and Beam Sim WC Residual.	100
215	6.10	Comparison of True Momentum in WC4 to Reconstructed Momentum	102
216	6.11	Comparison of Midplane Matching ΔX and ΔY : Data and +100 A Simulation . . .	102
217	6.12	Time of Flight and Momentum for +100 A: Data and Sim	104
218	6.13	Reconstructed Mass for +100 A: Data and Sim	105
219	6.14	ACNET Intensity for Spills	107
220	6.15	Fractional Content of Low Mass Particles: +100A	108
221	6.16	Time of Flight and Momentum for +60 A: Data and Sim	110
222	6.17	Reconstructed Mass for +60 A: Data and Sim	111

223	6.18 TOF Accidental Rate in +60 A Proton TOF Peak	112
224	6.19 Fractional Content of Low Mass Particles: +60 A	113
225	6.20 +100A Three Point Track Momentum Comparison: Simulation and Data	114
226	6.21 Percentage Error of Momentum Reconstruction: Four Point and Three Point Tracks	115
227	6.22 +60 A DDMC Upstream Track Existence and Pileup Filter	116
228	6.23 +100 A DDMC Upstream Track Existence and Pileup Filter	117
229	6.24 WC-TPC α Comparison Between +60 A and +100 A Protons	118
230	6.25 +60 A DDMC Positron Event Shower Pass Rate	119
231	7.1 Depiction of Thin Slice Method	124
232	7.2 Energy Deposition and Pitch Comparison: +60 A Data and MC Cross Section Tracks	126
233	7.3 Energy Deposition and Pitch Comparison: +100 A Data and MC Cross Section Tracks	126
234	7.4 Energy Deposition vs Residual Range Comparison: +60 A Data and MC Cross	
235	Section Tracks	127
236	7.5 Energy Deposition vs Residual Range Comparison: +100 A Data and MC Cross	
237	Section Tracks	128
238	7.6 +60 A Observed Incident and Interacting Histograms: Data and MC Cross Section	
239	Tracks	128
240	7.7 +100 A Observed Incident and Interacting Histograms: Data and MC Cross Section	
241	Tracks	129
242	7.8 Background Correction Factors for +60 A MC	131
243	7.9 Background Correction Factors for +100 A MC	132
244	7.10 Examples of Reconstruction Inefficiency Using Elastic Scattering Event	133
245	7.11 Average Spacepoint Distance from Line of Best Fit	134
246	7.12 Depiction of Angular Resolution Method	135
247	7.13 Angular Resolution Plot for Data and MC	136

248	7.14 +60 A MC Reconstruction Efficiency Corrections	138
249	7.15 +100 A MC Reconstruction Efficiency Corrections	139
250	7.16 Background and Efficiency Corrected Cross Section: Stats Only	140
251	8.1 Comparison of Total Energy Loss Per Slice	143
252	8.2 Systematic of 2 mm Smearing of Hit Reconstruction	144
253	8.3 Energy Systematics for +60 A Data Cross Section	146
254	8.4 Energy Systematics for +100 A Data Cross Section	147
255	8.5 +60 A Final Cross Section	149
256	8.6 +100 A Final Cross Section	150
257	8.7 Comparison of +60 A and +100 A Cross Section	151
258	8.8 Combined Cross Section with Geant4 Prediction	152

Introduction

260 The Standard Model is the cornerstone of particle physics interactions. Many types of interactions
261 have been described or predicted by its formulation. For example, the discovery of the Higgs
262 boson in 2012 was a significant achievement of the predictive power of the model [1]. However,
263 the Standard Model does not explain all observed phenomena. For example, though the existence
264 of the neutrino was postulated 80 years ago by Wolfgang Pauli and discovered 60 years ago, the
265 discovery of neutrino oscillations, where one flavored neutrino has a probability to transmute into
266 another flavor, has no explanation within the Standard Model [2].

267 Such Beyond Standard Model (BSM) physics in the neutrino sector has launched a new dis-
268 covery era of research to find and measure other theorized phenomena. Simultaneously, neutrino
269 experiments are being developed to more precisely measure already known physics, with higher
270 statistics and reduced uncertainty. Neutrino cross sections and neutrino oscillation parameters
271 are two examples. Unfortunately, neutrinos are unlikely to interact in matter, compared to other
272 fundamental particles. Moreover, neutrinos are neutrally charged and have relatively small, but
273 non-zero, mass. This makes direct detection of neutrinos difficult, requiring experiments to rely on
274 measurements of daughter particles from an neutrino interaction has a indirect observation of the
275 initial neutrino's kinematics.

276 Many technologies exist to detect neutrino interactions. One of these technologies is the Time
277 Projection Chamber (TPC) using liquid argon as the active medium (LArTPC). LArTPCs can
278 provide precise measurements of both position and energy of charged particles that are the daughters
279 of a neutrino interaction. The US neutrino program is highly invested in LArTPCs, launching a
280 series of scalable experiments designed to probe various neutrino physics, from ArgoNeuT, a 0.25
281 ton table-top sized experiment in 2010, to DUNE, a 40k ton experiment currently being designed

and scheduled to begin operation in 2026 [3] [4]. Currently, MicroBooNE, a 170 ton LArTPC is operating at Fermilab in a ν_μ beam, measuring oscillation parameters and low energy cross sections, as well as searching for exotic particle and astroparticle physics[5].

As mentioned before, LArTPCs do not directly measure the neutrino, but instead observe the daughters of a neutrino interaction. A vital part of tagging a neutrino interaction is the precise measurement of the kinematics of the interaction and accurate identification of particle species created by the interaction. For oscillation experiments, often the flavor oscillation that is measured is $\nu_\mu \rightarrow \nu_e$. When a neutrino interacts in matter, the lepton associated to the neutrino is produced, for example, in a charged current interaction, $\nu_\mu + n \rightarrow \mu^- + p$. It is not uncommon for a pion to be produced in an interaction: $\nu_\mu + p(n) \rightarrow \mu^- + \pi^+ + p(n)$. However, without a magnetic field, it can be difficult to identify the pion from the muon, as both have similar masses and leave similar signatures within a LArTPC. Developing reconstruction techniques capable of distinguishing the two becomes important, as failure to correctly tag the pion or muon will change the topology of the interaction and attribute the event as part of a different interaction channel. Also, pions can re-interact within the detector volume. Understanding how often these re-interactions occur via a cross-section measurement can inform detector simulation and help identify a pion when it interacts.

To test detector response and refine reconstruction techniques, a test beam experiment was founded. The LArIAT experiment (Liquid Argon In A Testbeam) operates a LArTPC in a charged test beam, and is dedicated to the development of reconstruction techniques and detector research, as well as measurement of a π -LAr cross section that can be used as input for simulation for the greater LArTPC neutrino program. Operating in charged test beam provides a benefit compared to neutrino experiments, as auxiliary beamline instruments can provide additional information about the incoming charged particle, and the TPC can directly measure the energy of the interacting particle as well as the charged daughters.

This dissertation is composed of 8 chapters. Chapter 1 describes the theoretical framework of neutrino interactions and explains the necessity for a π^+ -LAr cross section measurement. Chapter 2 describes the LArTPC detector technology in general, while chapter 3 focuses on the LArIAT experiment and auxiliary detectors. Chapter 4 discusses the reconstruction of the various detectors

311 used in LArIAT. Using the reconstructed variables described in chapter 4, the method of selection
312 of π^+ for a cross section analysis is given in chapter 5. Chapter 6 discusses the preparation of the
313 Monte Carlo simulation and analysis of the beamline simulation. In Chapter 7, an explanation
314 how the cross section is measured, along with the necessary corrections to account for background
315 species and reconstruction effects if given, and the cross section is shown with statistical uncer-
316 tainty. Chapter 8 accesses the systematic uncertainty for the analysis, shows the cross section with
317 both statistical and systematic uncertainty and compares to the GEANT4 predicted cross section.
318 Finally, Chapter 9 provides conclusions and improvements for future analyses.

Chapter 1

Theory

In the realm of particle physics, the Standard Model (SM) [2] is a framework that aims to describe all phenomena on the subatomic level, including strong, electromagnetic, and weak interactions, incorporating quantum field theory as well. It is not an all-encompassing theory, as there is a well-documented tension between the macro-level predictions the SM makes and the observation and theory around gravity and relativity. However, for the subatomic world, the SM precisely explains and predicts most of the phenomena that has been observed.

1.1 The Particle Zoo

The Standard Model is a gauge theory based on the local symmetry group

$$G_{SM} = SU(3)_C \otimes SU(2)_L \otimes U(1)_Y \quad (1.1)$$

$SU(3)_C$ represents the strong force, where the C is shorthand for the “charge” associated with the strong force, “color”. The combination of $SU(2)_L$ and $U(1)_Y$ represent the interaction of weak and electromagnetic processes, though in slightly different notation. Many fundamental particles exist, though not all particles interact through the strong, weak, and electromagnetic forces. For example, quarks, which form bound states of baryons, such as protons, and mesons, such as pions, interact through all three forces. Electrons and muons interact via the weak and electromagnetic forces. Neutrinos only interact via the weak force. Each particle species also has different sets of

Generation	I	II	III	T	Y	Q
Leptons	$\nu_{e,L}$	$\nu_{\mu,L}$	$\nu_{\tau,L}$	1/2	-1	0
	e_L	μ_L	τ_L	-1/2	-1	-1
	e_R	μ_R	τ_R	0	-2	1
Quarks	u_L	c_L	t_L	1/2	1/3	2/3
	d_L	s_L	b_L	-1/2	1/3	-1/3
	u_R	c_R	t_R	0	4/3	2/3
	d_R	s_R	b_R	0	-2/3	-1/3

Table 1.1: SM elementary fermionic fields with isospin (T), hypercharge (Y) and electric charge (Q). Subscripts L and R represent negative chirality (left-handed) and positive chirality (right handed).

quantum mechanical numbers, such as electric charge, Q, hypercharge, Y, and isospin, T. Table 1.1 reviews the various fundamental particles described in this section. Currently, there are 6 known quarks, which exist in three pairs. There is the up-down pair, charm-strange pair, and top-bottom pair, along with their anti-particle versions; up and down quarks make up most of the quark-based matter in the universe, such as protons and neutrons, and are the lightest of the quarks. Charm and strange quarks are heavier and are more rare; kaons are a common example of a particle that has a strange quark as part of its composition. Top and bottom quarks are the heaviest quarks, and were the last to be discovered. Particles with bottom quark content are usually produced in particle accelerators. Though CERN is the primary producer of bottom quark-comprised particles, Fermilab-based experiments first observed the bottom quark in 1977, and the top quark in 1995. The top quark is not capable of forming hadrons, given the top quark lifetime is shorter than the time scale for strong interactions.

Leptons are another type of particle that have no quark content, and therefore do not interact via the strong force. There are 3 charged leptons: the electron, the muon, and the tau, in ascending order of mass. Each lepton also has an associated electro-neutral neutrino: ν_e , ν_μ , ν_τ . Neutrinos were thought to be massless. However, observation of neutrino flavor oscillation proved neutrinos to have small, but non-zero masses, which is not accounted for by the Standard Model. Beyond Standard Model phenomena are discussed in a future section.

Quarks and leptons differ in their quark content, however they both share one quality, in that all quarks and leptons have half-integer spin, which classifies them as “fermions”, and as such, follow Fermi-Dirac statistics.

Another way to classify fermions is by chirality. Chirality is the relationship between the spin of a particle and the momentum. If the spin and momentum vectors of a particle are parallel, the particle is said to be right-handed. Similarly, particles where the spin and momentum vectors are anti-parallel are left-handed. Generally, only left-handed fermions and right-handed anti-fermions interact via the weak force. Interestingly, though right-handed charged leptons have been observed, there has yet to be an observation of a right-handed neutrino or left-handed anti-neutrino. Given this, right-handed neutrinos are not listed in table 1.1.

There also exist integer spin particles, called “bosons”, that follow Bose-Einstein statistics and are the particles that “carry” the force of an interaction from one particle to another. For example, the photon (γ), which is the mediator for electromagnetic interactions, is a spin-1 boson. The strong force is mediated by a group of eight gluons (g), and the weak force is mediated by three bosons (W^\pm, Z^0). When a particle undergoes a “force”, it is transferring these bosons from one particle to another. For example, in π^+ decay, the pion, which is composed of $u\bar{d}$, interacts, creating a W^+ , which then creates a μ^+ and a ν_μ .

$$u + \bar{d} \rightarrow W^+ \rightarrow \mu + \nu_\mu \quad (1.2)$$

Initially, the gauge theory used in the SM was not able to accommodate massive particles. However, it was well established that many particles were massive, including the W and Z bosons, requiring alterations to the theory. This was done through the addition of a scalar iso-doublet, $\Phi(x)$, or the Higgs field, which would give mass to the W and Z bosons through the electroweak symmetry breaking and to fermions through Yukawa coupling. This field would have a boson associated to it, called the Higgs boson, and was theorized to exist in the 1960s. Discovery of the Higgs boson in 2012 at CERN was a massive accomplishment for the SM.

1.2 Neutrinos and Beyond Standard Model Phenomena

Neutrinos are the most abundant fermions in the universe; on Earth, billions of neutrinos pass through a square centimeter area every second. Moreover, though the SM can incorporate the existence of the neutrino, there are many phenomena that cannot be explained. In this section, these phenomena are outlined as well as the overview of experimental data probing these oddities.

As stated in the previous section, there has yet to be an observation of a right-handed neutrino. While curious in and of itself, the non-existence of the right-handed neutrino poses a problem within the Standard Model and the Higgs mechanism. Fermions acquire mass through the coupling of left-handed and right-handed fermions. For the charged fermions, this is not an issue, as both types exist, and so can be given a mass naturally. However, without a right-handed neutrino, there can be no coupling. Therefore, without a right-handed neutrino, the Standard Model would suggest the neutrino is massless. Direct measurement of the mass of the neutrino would suggest physics beyond what the Standard Model could predict.

Unfortunately, direct observation of the mass of the neutrino is difficult. Analyzing the kinematics of weak interactions where a neutrino was produced, the suggested mass of the neutrino was vanishingly small, and a massless neutrino would be well within the uncertainty of any calculation. Current measurements of the neutrino mass can only put an upper bound, but not preclude through direct measurement the possibility of a massless neutrino. For example, from tritium decay spectroscopy, the current estimation for the positron contribution to the anti-neutrino masses ($m_e = (\sum_i |U_{ei}|^2 m_{\nu_i}^2)^{0.5}$) is <2 MeV [6].

1.2.1 Neutrino Oscillations

The solution to our inability to measure directly the mass of the neutrino was to find an indirect method to prove if the neutrino was massive. If neutrinos were massive, there should exist a basis of three mass eigenstates, $|\nu_i\rangle$, each with a distinct mass eigenvalue. If the flavor eigenstates of the weak interaction, $|\nu_\alpha\rangle$, are not identical to the mass eigenstates, and are instead a superposition of the mass eigenstates, then a neutrino, which begins in a flavor eigenstate would begin to oscillate flavors as it travels. This would occur because each of the mass eigenstates with a different mass

eigenvalue would evolve differently under the Hamiltonian describing motion of a free particle. Therefore, a ν_μ may become a ν_e without undergoing any other weak process. It is this exact phenomena that was being observed during the 1960s Solar Neutrino Problem, when fewer ν_μ from the sun were being observed given expectations from the sun's luminosity[7].

Many experiments documented the disappearance of certain flavors of neutrinos in various energy ranges. In 1998, Super-Kamiokande announced discovery of neutrino oscillations, proving that neutrinos must be massive; Takaaki Kajita and Arthur McDonald were awarded Nobel Prizes for the discovery in 2015[8]. The mixing matrix of mass eigenstates, $|\nu_i\rangle$, and flavor eigenstates, $|\nu_\alpha\rangle$, is given by $|\nu_\alpha\rangle = U_{PMNS}^* |\nu_i\rangle$, using the Pontecorvo-Maki-Nakagawa-Sakata matrix [9]:

$$U_{PMNS} = \begin{pmatrix} 1 & 0 & 0 \\ 0 & c_{23} & s_{23} \\ 0 & -s_{23} & c_{23} \end{pmatrix} \begin{pmatrix} c_{13} & 0 & s_{13}e^{-i\delta} \\ 0 & 1 & 0 \\ -s_{13}e^{-i\delta} & 0 & c_{13} \end{pmatrix} \begin{pmatrix} c_{12} & s_{12} & 0 \\ -s_{12} & c_{12} & 0 \\ 0 & 0 & 1 \end{pmatrix} \begin{pmatrix} 1 & 0 & 0 \\ 0 & e^{i\alpha_2/2} & 0 \\ 0 & 0 & e^{i\alpha_3/2} \end{pmatrix} \quad (1.3)$$

where c,s indicate cosine or sine of the mixing angles $(\theta_{12}, \theta_{13}, \theta_{23})$, δ is the phase of CP violation, and α_1 and α_2 are the Majorana CP violation phases, if neutrinos are Majorana particles. It is these mixing angles that define how each mass eigenstate evolves over time. Neutrino oscillations allow experiments to probe some of these parameters. Oscillations also allow an indirect measurement of the relative scale of the neutrino mass eigenvalues. As an example, though complicated when discussing mixing of three neutrinos, when only a two neutrino case is considered, the mixing matrix, U, becomes a simple 2x2 rotation matrix with one mixing angle, θ and the probability of oscillation is given by:

$$P_{\alpha \rightarrow \beta, \alpha \neq \beta} = \sin^2(2\theta) \sin^2\left(\frac{\Delta m^2 L}{4E_\nu}\right), \Delta m^2 = m_1^2 - m_2^2 \quad (1.4)$$

where L is the distance the neutrino has travelled from the source, and E is the energy of the neutrino. This shows that in neutrino oscillations, it is not the mass eigenvalues which are measured, but the difference in the squares of the mass eigenvalues. Therefore, while the relative difference between the mass eigenstates can be measured, the absolute mass scale and the order, lightest to heaviest, of m_1, m_2, m_3 cannot. Current experimental values from global fits of data for some of the terms in the PMNS matrix and the mass differences are given in table 1.2 [6].

Parameter	best-fit	3σ
$\Delta m_{21}^2 [10^{-5} eV^2]$	7.37	6.93-7.96
$\Delta m_{31(23)}^2 [10^{-3} eV^2]$	2.56 (2.54)	2.45-2.69 (2.42-2.66)
$\sin^2 \theta_{12}$	0.297	0.250-0.354
$\sin^2 \theta_{23}, \Delta m_{31(32)}^2 > 0$	0.425	0.381-0.615
$\sin^2 \theta_{23}, \Delta m_{32(31)}^2 < 0$	0.589	0.384-0.636
$\sin^2 \theta_{13}, \Delta m_{31(32)}^2 > 0$	0.0215	0.0190-0.0240
$\sin^2 \theta_{13}, \Delta m_{32(31)}^2 < 0$.0216	0.0190-0.0242
δ/π	1.38 (1.31)	2σ : (1.0-1.9) (2σ : (0.92-1.88))

Table 1.2: Global fit value of neutrino oscillation data. Values (values in brackets) correspond to the normal (inverted) hierarchy of $m_1 < m_2 < m_3$ or $(m_3 < m_1 < m_2)$. Indices on Δm^2 indicate which mass splitting gap is being measured or assumed, e.g $\Delta m_{31}^2 = m_3^2 - m_1^2$.

1.2.2 Other Open Questions

Along with neutrino oscillations, there are other open questions about physics in the neutrino sector which are not explained or predicted to exist through the Standard Model. A few of these possibilities are given here.

Mass Hierarchy and Absolute Mass Scale

From experimental measurements of the mass splitting via Δm^2 , it is known that two of the neutrinos, ν_1 and ν_2 are close in mass, while a larger gap exists between these neutrinos and ν_3 . However, it is unknown in which order these neutrinos exist, allowing for two mass hierarchies. The normal hierarchy has ν_3 as the heaviest with a large gap to ν_2 followed by a small gap to ν_1 . The inverted hierarchy has ν_2 as the heaviest neutrino, with ν_1 slightly lighter and ν_3 being significantly lighter than the others. Moreover, the absolute mass of these neutrinos is still unknown. The goal of some neutrino experiments, such as NOvA and KATRIN, is to understand the absolute scale of the neutrino mass and to place them in the correct mass ordering.

441 Sterile Neutrinos

442 Using the theory of neutrino oscillations and a well defined neutrino beam, neutrino oscillation
 443 experiments can predict an appearance rate for other neutrinos, for example, the appearance of
 444 $\nu_e(\bar{\nu}_e)$ from oscillations of a $\nu_\mu(\bar{\nu}_\mu)$ beam. Results from the Liquid Scintillator Neutrino Detector
 445 (LSND) and MiniBooNE [10, 11] found an excess of ν_e and $\bar{\nu}_e$ appearing in their experimental
 446 detectors, given their experimental conditions. These anomalies suggest there may be a way for ν_e to
 447 be created from the oscillation of a fourth neutrino species. This fourth neutrino, ν_4 , would not only
 448 have to be much heavier than the other neutrino species, but also not interact via the electroweak
 449 force. The term “sterile” neutrino is used for these non-electroweak-interacting theorized neutrinos.

450 CP Violation

451 In early theories on particle physics, it was thought that the physics of a system should be the
 452 same if a particle was switched for its anti-particle (Charge conjugation) while also inverting its
 453 spatial coordinates (Parity symmetry). Therefore, the universe should be subject to Charge-Parity
 454 symmetry (CP). However, in experiments for neutral kaon decay, it was found that the probability
 455 for decay for the long-lifetime component of K_L^0 , $K_L^0 \rightarrow \pi^+ + e^- + \bar{\nu}_e$ was slightly lower than the
 456 probability of decay of the long-lifetime component of \bar{K}_L^0 , $\bar{K}_L^0 \rightarrow \pi^- + e^+ + \nu_e$. These interactions
 457 are identical under CP conjugation, so the breaking of the symmetry between decay lifetimes showed
 458 that CP is violated by some interactions in the weak sector. CP violation allows an explanation
 459 for the asymmetry between baryons and anti-baryons in the universe; though possibly beginning
 460 in equal amounts in the early universe, CP violation could have allowed baryon production to be
 461 favored to anti-baryon production. CP violation can also be measured in the neutrino sector, and
 462 could also explain the baryon asymmetry through leptogenesis [12]. Using the PMNS matrix (1.3),
 463 the difference in the probability of electron to muon neutrino oscillation and positron to anti-muon
 464 neutrino oscillation [13] is given by:

$$P_{\nu_e \rightarrow \nu_\mu} - P_{\bar{\nu}_e \rightarrow \bar{\nu}_\mu} = J \cos(\pm\delta - \frac{\Delta_{31}L}{2}) \sin(\frac{\Delta_{21}L}{2}) \sin(\frac{\Delta_{31}L}{2}) \quad (1.5)$$

465 where

$$J = \cos(\theta_{13}) \sin(2\theta_{13}) \sin(2\theta_{12}) \sin(2\theta_{23}) \quad (1.6)$$

is the Jarlskog invariant [14], L is the length from neutrino source to detector, and

$$\Delta_{ij} = \frac{\Delta m_{ij}^2}{2E_\nu} \quad (1.7)$$

Constraining the uncertainty in the mixing angles, in particular θ_{23} which isn't as precisely known, as well as the mass splittings can allow a more precise measurement of the CP violation phase, δ .

Neutrinos: Majorana or Dirac Particles?

Each particle that exists also has an anti-particle to associate with it. Most particles can easily be distinguished from its anti-counterpart; for example, it is easy to tell an electron, e^- , from a positron, e^+ , by measuring the sign of the electric charge. Particles that are distinct from their anti-particles are called “Dirac particles”. All charged fermions are Dirac Particles, as the sign of the electric charge of the particle is different between a charged particle and its anti-particle. However, for some uncharged particles, it is possible that the particle and its anti-particle are the same thing: the photon is the most common example where $\gamma = \bar{\gamma}$. Neutrons, though uncharged, are not identical to anti-neutrons, given the sign of the magnetic moment of the two differ. Fermions that are identical to their anti-particles are called “Majorana” fermions.

Given neutrinos are uncharged, it is possible they are Majorana particles. Neutrinos have no signed measurable value, like charge or magnetic moment, that could easily be measured between the neutrino and anti-neutrino to prove they are distinct. If neutrinos are Majorana particles, then there are some theoretically allowable interactions which would not be possible if neutrinos are Dirac particles. A candidate process that would suggest neutrinos are Majorana particles is that of neutrino-less double beta decay, $0\nu\beta\beta$.

In standard $2\nu\beta\beta$ events, two neutrons decay into protons, emitting an electron and $\bar{\nu}_e$ each. This process is rare and restricted to only a few isotopes, but is allowed and well-documented. However, if neutrinos and anti-neutrinos are identical, as would be the case if they were Majorana particles, then it is just as rational to say one of the $\bar{\nu}_e$ is actually a ν_e , allowing this $\nu_e \bar{\nu}_e$ pair to annihilate, leaving no neutrinos in the final state. This would be an even rarer process, if at all possible, and easily lost in the background of other more common topologies, requiring $0\nu\beta\beta$ experiments to have exceptionally low noise. However, were such an event be observed, it would

prove neutrinos are actually Majorana particles, would be a massive accomplishment for neutrino research, and require a re-write of our understanding of neutrinos.

1.3 Neutrino Interactions

There are many open questions about neutrinos, but all are probed, directly or indirectly, after a neutrino has interacted. Therefore, it is fundamental to understand how neutrinos interact within matter and how the daughters of those interactions would appear inside a detector. Most neutrino accelerator experiments operate in the range of 0.1-10 GeV, and within this range there are three interaction modes available: charged current quasi-elastic (CCQE), resonant (RES), and deep inelastic (DIS) scattering.

Quasi-elastic scattering, which is dominant at lower energies, occurs when a neutrino interacts with one of the nucleons in the nucleus producing a charged lepton:

$$\nu_l + n \rightarrow l^- + p \quad (1.8)$$

$$\bar{\nu}_l + p \rightarrow l^+ + n \quad (1.9)$$

In this case, the topology is straight forward, ignoring final state interactions. Assuming the detector can only “see” charged particles, a lepton appears in the detector, possibly with a proton. In the $\bar{\nu}_l$ case, the neutron may not be visible initially, but can undergo scattering off of many argon atoms, creating “neutron sparkle”, a small charge deposition from nuclear recoil with each argon atom.

The second interaction, resonant scattering, occurs within the 1-10 GeV range. In this case, the neutrino is at the appropriate energy to excite one of the nucleons, creating either a Δ or N^* . This resonant particle then de-excites, producing a number of pions along with the lepton:

$$\nu_l + N \rightarrow l + \Delta/N^* \rightarrow l + n\pi + N' \quad (1.10)$$

In this case, the topology may be complicated. These de-excitations occur on the order of 10^{-24} s, which would be before the excited particle can escape the nucleus. Therefore, the created pions would also have to escape the nucleus to be seen in the detector, allowing many instances for re-interactions inside the nucleus. This can greatly alter the pion’s energy or cause other particles to be created or destroyed, making reconstruction of this event difficult.

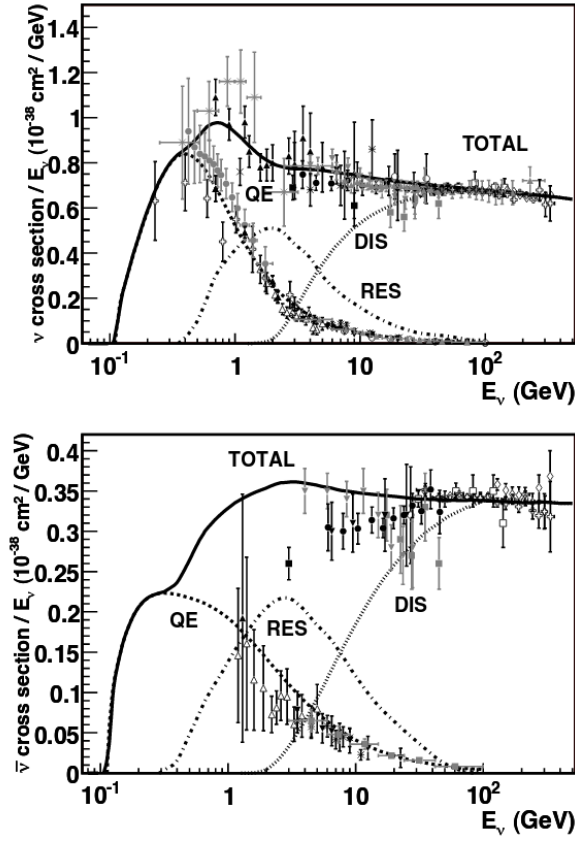


Figure 1.1: Total ν_μ (top) and $\bar{\nu}_\mu$ (bottom) cross sections per nucleon, divided by neutrino energy, as a function of energy over the range of 0.1-100 GeV [15]. Plotted curves are given by the NUANCE generator[16], showing the total cross section (solid) and the three constituent parts: CCQE (dashed), resonance (dot-dash), and deep inelastic scattering (dotted).

At higher energies, a neutrino can undergo DIS, where the neutrino can penetrate the nucleon itself, and interact with quarks within the nucleon, producing many hadrons in the final state. Figure 1.1 summaries the various measurements of ν_μ and $\bar{\nu}_\mu$ across this energy range of 0.1 to 100 GeV [15].

1.4 Pion Cross Sections and Understanding Neutrino Interactions

Neutrino experiments interact on nuclear targets. However, experiments cannot directly measure the physics that occurs within the nucleus. Instead, in order to understand what type of interaction occurred between the neutrino and nucleus, experiments must use the daughters that escape

the nucleus, and use the kinematics of those particles to reconstruct the event as a whole, using simulated nuclear models to inform what might have occurred in the nucleus. Unfortunately, as the nuclear effects are not fully known, there are many models and simulation packages to choose from, each with different approximations for inter-nuclear effects. Moreover, the differences in the nuclear models predict different distributions for measurable quantities, such as particle multiplicity, kinematics, and scattering angles. A goal for neutrino and other related experiments is to provide experimental constraints that can be used to tune models to reflect more accurately the data, or in some cases, preclude a model entirely. With more data and more advanced models, a better understanding of the nuclear structure and the interactions that occur within the nucleus can be achieved.

Given this, it is imperative to be able to identify correctly and measure the kinematics of the daughters of a neutrino interaction. In particular, as they are relatively common as daughter of an interaction, understanding the kinematics of the pions that are created is necessary, including how the pions deposit energy in the detector and how often they re-interact in the detector after escaping the neutrino-interacting nucleus through a cross section measurement.

For neutrino detectors, liquid argon (LAr) is becoming a common detector medium, so a measurement of a π -LAr cross section is vital for neutrino experiments to use as input to their simulation packages. Interestingly, though pion cross sections have been measured for many nuclei, and shown in figure 1.2 [17], there has yet to be a π^+ or π^- cross section measurement on argon. For simulation packages and nuclear modeling, this is a problem, as it requires an extrapolation of data on other nuclei to estimate the effects on argon, and imposes large uncertainties on the extrapolated cross section the models use.

Directly measuring the π^+ -LAr cross section can greatly reduce these uncertainties and better inform nuclear models, as well as provide physics measurements not yet known. This is especially true in the energy range where Δ resonance is dominant. From figure 1.2, in this energy range, the cross section curves take on different shapes, other than a simple scaling relative to the number of nucleons in the target nucleus. Not only does each cross section vary in how it rises and falls away from the peak, but the peak for each curve is at a different energy, due to different inter-nuclear effects dependent on mass number. A cross section extrapolation for argon would not be as simple

as scaling by a constant the cross section from another nuclei; a direct measurement of the cross section is necessary.

1.4.1 Pion Interactions Considered for Cross Section

Generally speaking, a pion cross section can be separated into the elastic and reaction channels.

$$\sigma_{total} = \sigma_{Elastic} + \sigma_{Reaction} \quad (1.11)$$

Elastic scattering includes the pion scattering off of a nucleus without creating new particles as part of the process. In this case, the initial and final state pion are considered to be the same particle. The question becomes how to decide the definition of “reaction” for a measurement. For this analysis, the hadronic interaction cross section is considered, where interaction occurs through the strong force. Electromagnetic processes and weak processes, such as pion decay, are excluded from the analysis. Accounting for the various interaction channels available via the strong force the reaction cross section can be written as:

$$\sigma_{Reaction} = \sigma_{Inel} + \sigma_{Abs} + \sigma_{Chex} + \sigma_{\pi prod} \quad (1.12)$$

where the inelastic scattering, pion absorption with the ejection of protons, charge exchange and pion production channels are included. Table 1.3 lists the topologies for each of these interaction channels. Figure 1.3 shows event display candidates for each of these topologies, as recorded by the LArIAT experiment, which will be described in chapter 3 [18]. Various terminologies can be used to describe the non-elastic interactions considered. When discussing certain channels, the individual terms, such as charge exchange, will be used. However, when considering in aggregate all non-elastic interactions in this analysis, the term “inelastic” will be used instead of “reaction”. LArIAT uses Geant4 as the simulation package, and uses the FTFP_BERT physics model list, based on the Bertini cascade model, to inform pion propagation through the detector[19]. Using this physics list, and extrapolating from other data sets, the cross section Geant4 assumes for π^+ -LAr is given in figure 1.4.

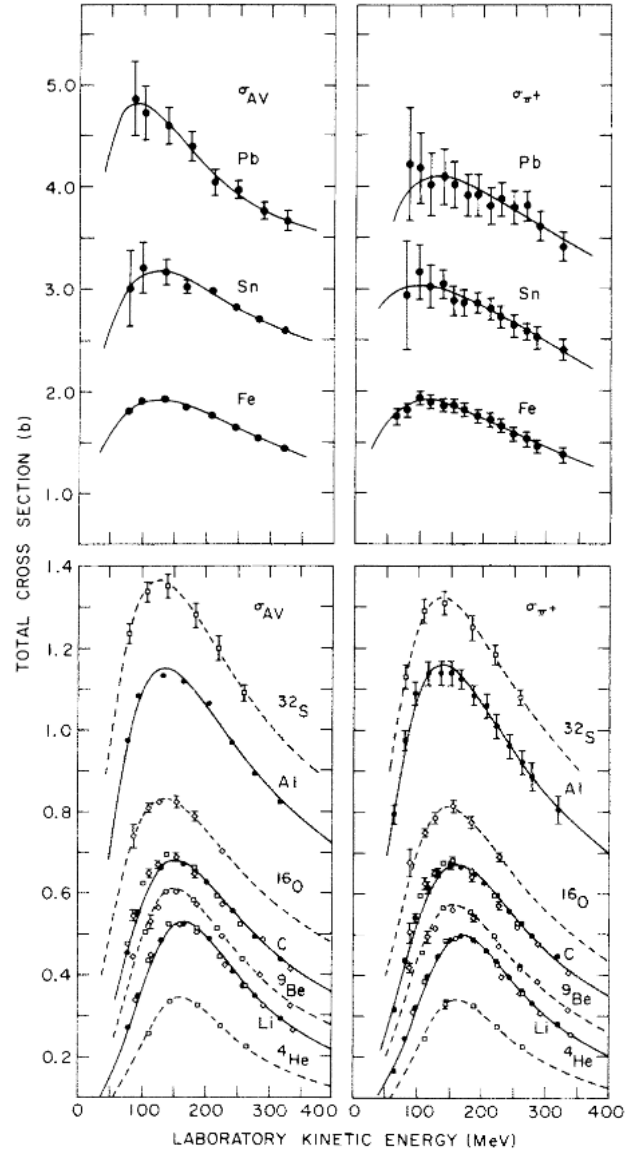


Figure 1.2: Pion-nucleus cross section on various nuclei: σ_{π^+} (right) and σ_{AV} (left), where σ_{AV} is the average of the π^- and π^+ cross section measurements[17]. The energy range is in the Δ resonance region of 100-400 MeV.

N π in Final State	Channel Name	Reaction	Notes
0	Pion Absorption , σ_{abs}	$\pi^+(nn) \rightarrow np$ (two-body abs) $\pi^+(mm) \rightarrow mnp$ (three-body abs) $\pi^+(mnp) \rightarrow (npp)$ (three-body abs) $\pi^+(mnp) \rightarrow (ppn)$ (multi-body abs)	Suppressed absorption on single nucleon due to energy conservation, requiring interaction on multi-nucleon systems.
1	Elastic Scattering , σ_{El}	$\pi^+ + N \rightarrow \pi^+ N$	Scattering on nucleon while leaving system in a ground state
1	Charge Exchange , σ_{Chex}	$\pi^+ + n \rightarrow \Delta^+ \rightarrow \pi^0 + p$	Charged pion changes to neutral pion
1	Inelastic Scattering , σ_{Inel}	$\pi^+ + n \rightarrow \Delta^+ \rightarrow \pi^+ + n$ (knockout) $\pi^+ + p \rightarrow \Delta^{++} \rightarrow \pi^+ + p$ (knockout)	Pion interacts within nucleus, knocking out one or more nucleons
2+	Pion Production , $\sigma_{\pi prod}$	$\pi^+ + N \rightarrow \geq 2\pi + \text{nucleons}$	Possible if pion K.E $\geq 2m_\pi$

Table 1.3: Example topologies considered for “reaction” π^+ cross section as function of pion multiplicity in final state.

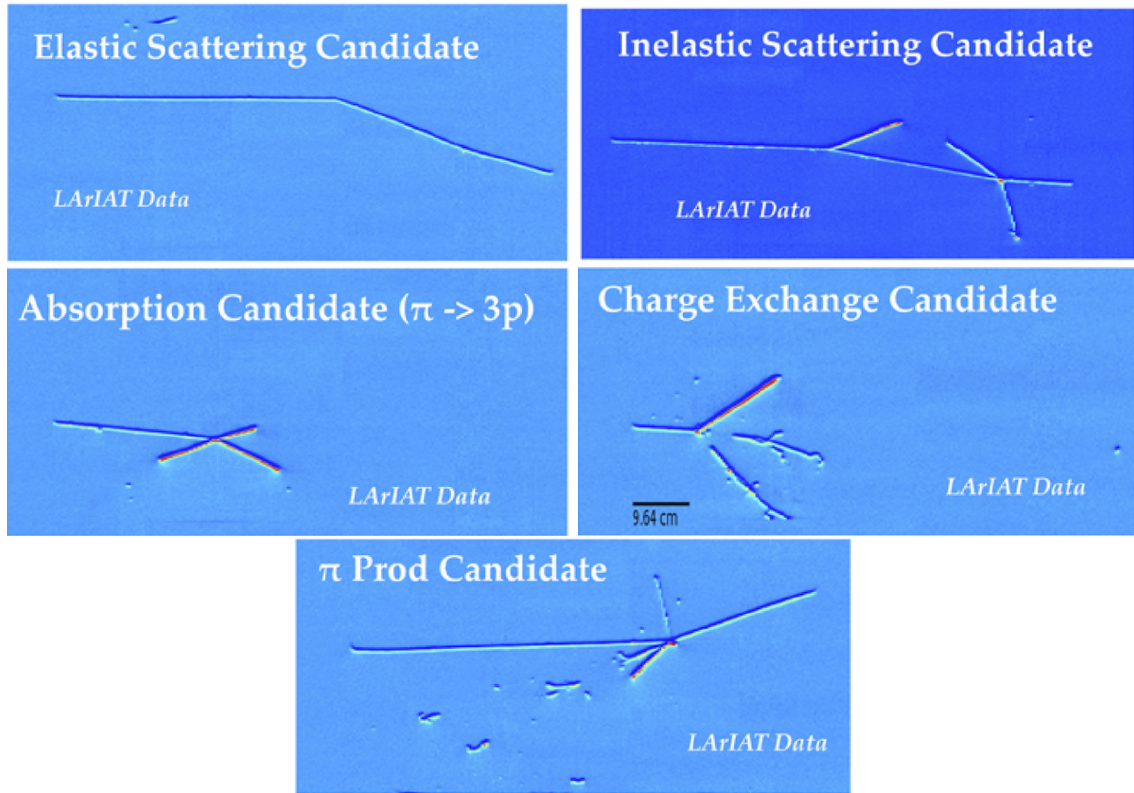


Figure 1.3: Data event candidates for elastic and inelastic scattering, pion absorption, charge exchange and pion production. Event displays of the collection plane. [18]

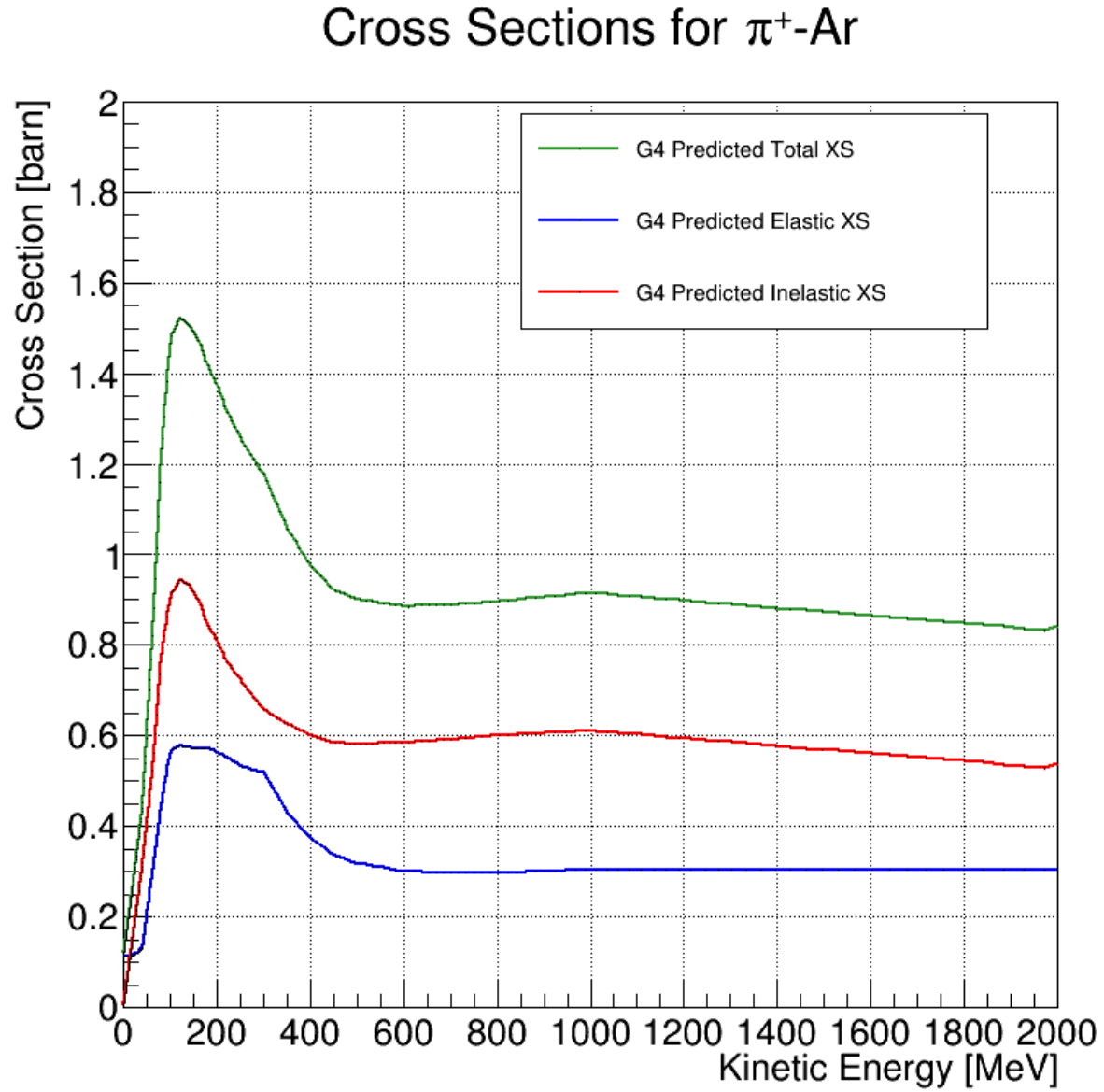


Figure 1.4: Predicted π^+ -Ar total cross section (green), separated into elastic (red) and inelastic (blue) components, as a function of interacting kinetic energy. Simulation was done in Geant4 10.01.p3 using the FTBF_BERT physics list [19].

Chapter 2

LArTPC

This chapter discusses the LArTPC technology, including how a TPC works, the rationale behind using liquid argon as a medium, and the method for reconstructing an event from the information collected by the TPC.

2.1 Time Projection Chambers Using Liquid Argon

The time projection chamber (TPC) was initially proposed by David Nygren in 1974 [20] as part of the PEP-4 experiment, which probed e^+/e^- collisions at SLAC. Since then, the TPC design has been tailored for many experiments using various active media, such as e^+/e^- interactions with PEP-4, dark matter experiments (ArDM), rare decay experiments (TRIUMP), neutrino experiments (SBND, ICARUS, DUNE, MicroBooNE) and neutrinoless double beta decay experiments (EXO); a major benefit of the TPC technology is its versatility as an experimental design. An overview of TPC designs and active media is given in [21]. As a detector technology, TPCs are the only ionization detector design available that allows for electronically read, 3D track and energy reconstruction. With this, track and energy-based particle identification over a large range of particle momenta is possible.

The first TPC designs, including the original PEP-4 experiment, used gases as the detector active medium. Soon after, a liquid based detector media was proposed, with Carlo Rubbia proposing a liquid argon detector in 1977 [22]. A liquid noble-element detector medium has numerous ad-

vantages over a gaseous medium, particularly when discussing viability for a neutrino experiment. Liquids are approximately 1000 times more dense compared to a gas. Therefore, for the same volume detector, there are many more target nuclei for a neutrino to interact. As the cross-section scales with target density, a denser liquid increases the probability of a neutrino interaction. Moreover, as the energy loss of a charged particle is proportional to the density of the target, a liquid detector medium allows better calorimetric reconstruction, as a particle will leave a more distinct energy deposition in a liquid compared to a gas. Liquids have a much lower ionization compared to gases, so more electrons will be ionized in a liquid compared to its gaseous counterpart. This causes a higher energy loss to ionization, and forces a particle to deposit its energy over a shorter range. A particle that deposits its energy over a shorter range is more likely to be fully contained inside the TPC, allowing for a complete measure of its energy deposition.

However, there are drawbacks to using a noble liquid as an active medium, and some choices to be made determining which noble element to use. Noble liquids require an expensive cryogenic system to maintain the liquid state. The boiling point of nobles scales with the atomic number, so lighter nuclei have to be cooled more to create the liquid form. Argon is the current choice for many neutrino experiments, while xenon is preferred for dark matter experiments. Table 2.1 gives a comparison between these two nuclei. Though xenon has some more desirable qualities for neutrino experiments, such as a higher density, lower ionization energy threshold, and a higher light yield, the cost of xenon makes it unfeasible for large, ton scale experiments.

2.2 LArTPC Operational Concept

Simplistically, a LArTPC is similar to a capacitor, with a high voltage cathode and a series of anode planes. Depending on the size of the detector, the cathode voltage may change, but is usually set to maintain an electric field near 500 V/cm. To ensure the electric field remains uniform throughout the TPC, conducting metal rings are placed along the walls of the TPC at regularly spaced intervals. By connecting resistors between each ring, the rings gradually step down the voltage across the volume of the TPC, maintaining a constant electric field throughout.

When a charged particle passes through the detector, it will ionize electrons from the liquid argon. Given the electric field in the detector, the electrons will drift toward the anode side of

Element	LAr	LXe
Atomic Number	18	54
Atomic Weight A	40	131
Boiling Point at 1atm	87.3 K	165.0 K
Density	$1.4 \frac{g}{cm^3}$	$3.0 \frac{g}{cm^3}$
Radiation Length	14 cm	2.8 cm
Moliere Radius	10 cm	5.7 cm
Work Function	23.6 MeV	15.6 MeV
Electron Mobility at $E_{field} = 10^4 \frac{V}{m}$	$0.047 \frac{m^2}{Vs}$	$0.22 \frac{m^2}{Vs}$
Average $\frac{dE}{dx}$ MIP	$2.1 \frac{MeV}{cm}$	$3.8 \frac{MeV}{cm}$
Average Scintillation Light Yield	$40000 \frac{\gamma}{MeV}$	$42000 \frac{\gamma}{MeV}$
Scintillation Wavelength	128 nm	175 nm
Cost per kg	< \$10	> \$1000

Table 2.1: Summary of LAr and LXe properties relevant for neutrino detectors.

the detector. At the anode are a series of wire planes, typically three. Each wire plane has the same wire to wire distance (pitch), but each plane's wires are oriented at a different angle. For example in LArIAT, the planes are oriented at 0, +60 and -60 degrees with respect to the vertical, with a 4mm wire-to-wire distance. Each plane is held a particular voltage to satisfy transparency conditions; when deposited charge reaches the wire planes, the transparency conditions, which are a function of the geometry of the wire planes and the potential at which each wire plane is held, ensure the charge passes by the first two wire planes, and is collected on the final wire plane. Given the charge is collected on the final plane, it is commonly referred to as the collection plane. The other planes that do not collect charge are called induction planes, as when charge passes by a wire on these planes, it will induce a current on the wire, via Faraday's Law. A cartoon of a TPC design is given in figure 2.1. Each wire probes the region of the TPC that is co-planar with the wire. Therefore, when a signal, or hit, occurs on a given wire, the position where the electrons were sourced, or where the charged particle was in the detector, can be narrowed to a 2-D region of the TPC. These electrons will also leave a signal on a wire on another wire plane, tracing another 2-D

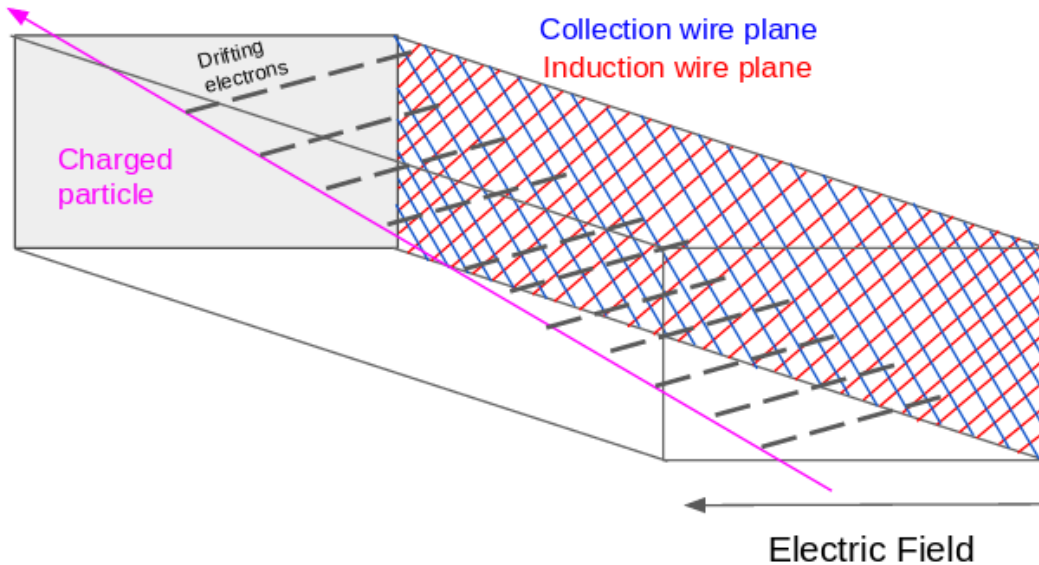


Figure 2.1: As a charged particle travels through the detector medium, it ionizes electrons, which are collected on a set of wire planes. The final plane, or collection plane, is where the charge is physically collected, while the previous planes are called induction planes.

region of the TPC. By matching these hits to each other, the position can be narrowed to a line through where the two wires overlap, confirming the two of the three coordinates of the particle, with only the distance along the electric field left unknown. However, as the electric field has a constant magnitude through the active volume, the electrons will drift through the TPC with a constant velocity. The two matched hits across two wire planes should occur at the same time. By knowing when the particle entered the detector, and measuring the time when these two matched hits occurred, the position along the drift direction can easily be calculated using the time of the hit and the drift velocity, and a 3-D position of a point along the trajectory of the ionizing particle is known. By time matching many pairs of hits, then using that matched time with the drift velocity, many points along the trajectory can be sampled, creating a discretized 3-D view of the particle passing through the detector.

A LArTPC can also be augmented with a light collection system placed behind the wire planes to collect light produced from argon scintillation in the detector. As this light arrives almost

instantly at the light collection system, this can provide a T_0 for the start of the event in the TPC. Also, this light can be used for calorimetry, as this light is another way, along with charge deposition, that a particle can lose energy traversing the active volume of the TPC. Moreover, the light yield and the charge depositions are related to each other, which will be discussed later in the chapter.

2.3 Energy Deposition and Screening Effects

In this section, how energy is deposited in the LAr is discussed, as well as the screening effects due to the bulk argon that can affect the charge and light produced before it reaches the anode wire planes.

2.3.1 Ionization Charge

The mean energy loss for a particle can be described by the Bethe-Bloch equation [6]:

$$-\frac{dE}{dx} = Kz^2 \frac{Z}{A} \rho \frac{1}{\beta^2} \left[\frac{1}{2} \ln \frac{2m_e c^2 \beta^2 \gamma^2 T_{max}}{I^2} - \beta^2 - \frac{\delta \beta \gamma}{2} \right] \quad (2.1)$$

where z is the number of unit charge of the ionizing particle, Z and A are the atomic number and mass number, ρ is the density of the medium, m_e is the mass of the electron, γ is the Lorentz factor, T_{max} is the maximum kinetic energy that can be imparted onto a free electron, I is the mean excitation energy in eV, δ is the density correction and $K=0.307075 \frac{MeVcm^2}{g}$, a conversion factor. This equation is useful, as $\frac{dE}{dx}$ of a particle is one of the fundamental measurements a LArTPC makes, and is direct input into the calculation of a cross section. Figure 2.2 plots the density normalized energy loss, $\frac{dE}{\rho dx}$ for muons in copper over a large range of momentum. As this plot is normalized for density, the only difference between this plot and the plot for argon would be a small re-scaling for the difference in the ratio of $\frac{Z}{A}$ between copper and argon. Given particles in LArIAT are on the scale of $100 \frac{MeV}{c}$ and $1 \frac{GeV}{c}$, the energy loss is in the minimum ionization zone.

Ionizing collisions occur randomly, but the number of collisions, k , per segment of the track, s , can be described by a Poissonian function:

$$P(k) = \frac{(sN_e\sigma_i)^k}{k!} e^{-sN_e\sigma_i} \quad (2.2)$$

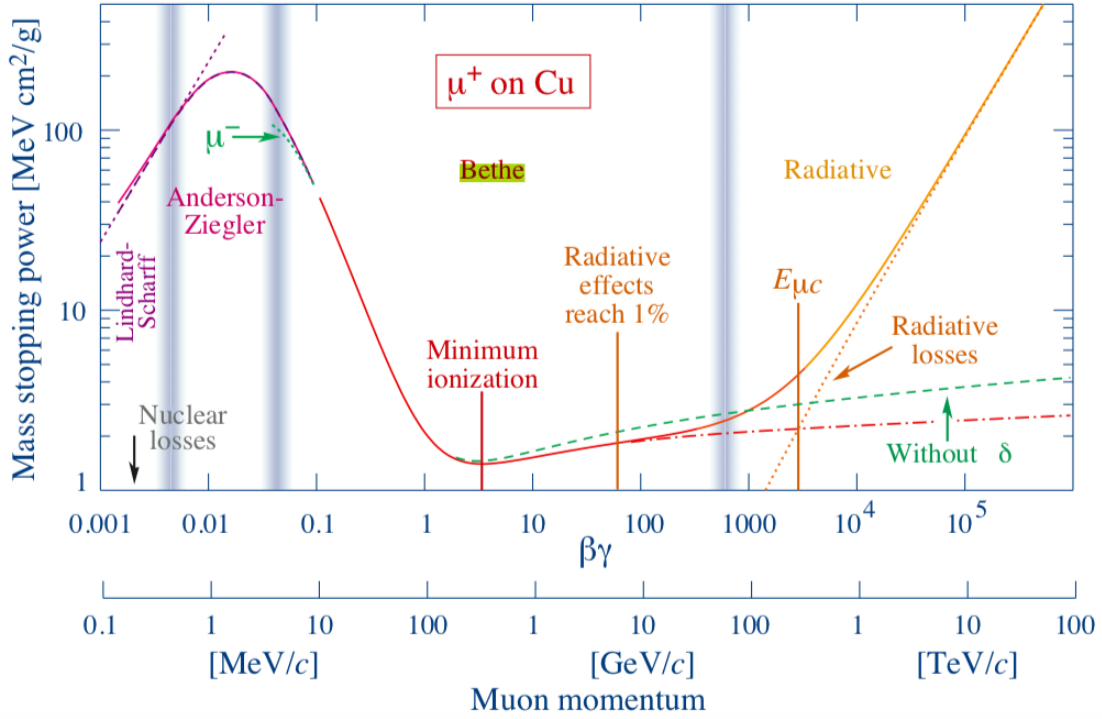


Figure 2.2: Density normalized energy loss, $\frac{dE}{\rho dx}$, vs momentum for muons in copper. The curve for argon would be similar, with a small re-scaling for $\frac{Z}{A}$. Particles in LArIAT have a momentum between $100 \frac{\text{MeV}}{c}$ to $1 \frac{\text{GeV}}{c}$.

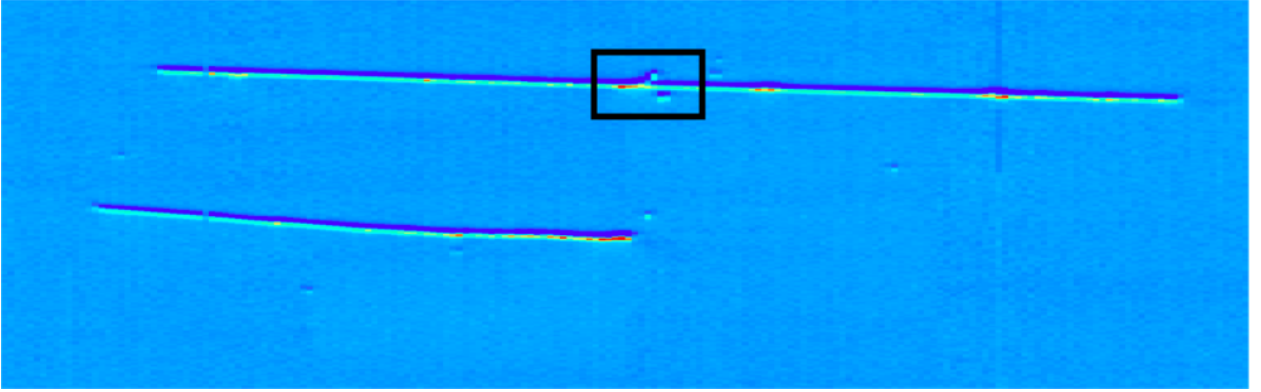


Figure 2.3: An event display from LArIAT of a muon with a δ -ray (black box). Event display is from the induction plane. (Run, Subrun, Evt)=(11201, 242, 26)

where N_e is the electron density and σ_i is the ionization cross section per electron. Usually, only one ionizing collision occurs, however it is possible for that initial ionization to liberate other electrons. Also, high energy electrons can be produced from the collision, which produce δ -rays: short, but detectable tracks branching from the original colliding particle. An event display showing a δ -ray is in figure 2.3.

Purity & Electron Lifetime

After the charged particle liberates electrons from the argon, those electrons drift toward the anode planes. However, there are multiple ways that this drift charge can be attenuated as it moves through the bulk of the detector. Electronegative contaminants in the LAr, such as oxygen, nitrogen, and water, can capture the electrons as they drift by. This will quench the charge that is collected at the anode planes. Moreover, this quenching is dependent on where the initial charge is deposited: tracks that pass through the TPC close to anode planes will deposit charge that must traverse a smaller amount of argon and impurities, and therefore be quenched less. Similarly, tracks that pass closer to the cathode will undergo more quenching of the deposited charge, as the ionized charge has a higher probability to encounter an impurity and be collected on it. Generally, the charge collected at the anode planes decays exponentially as a function of the distance from the anode planes. Moreover, as the distance can be translated into a drift time, a characteristic electron lifetime, τ_e can be calculated during running conditions. A lower

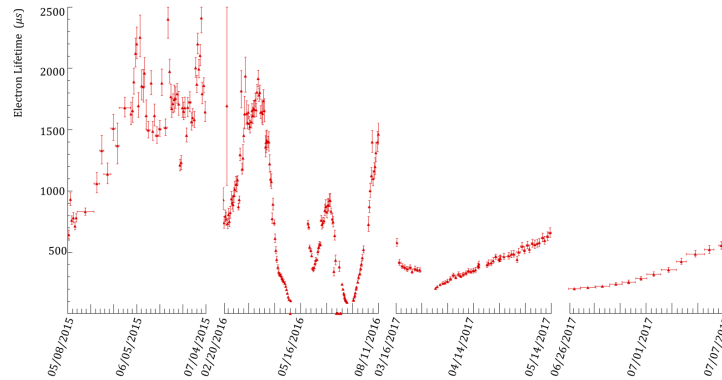


Figure 2.4: The electron lifetime during running conditions. A lower lifetime corresponds to dirtier argon.

electron lifetime corresponds to more contaminants in the argon. Figure 2.4 shows the electron lifetime for LArIAT for its experiment runtime. Depending on the maximum drift distance in an experiment, an acceptable electron lifetime may change. Smaller experiments like LArIAT can tolerate a lower electron lifetime, while larger experiments, such as MicroBooNE, another LArTPC neutrino experiment based at FermiLab, which has a 2.6 m drift distance, can accept lifetimes on the order of 10ms.

Electronegative contaminants can enter the system in many ways. LArTPCs are sealed and leak-checked to ensure atmospheric gases cannot enter the cryostat. Before filling, the cryostat can be vacuum-pumped or purged with gaseous argon to remove the initial contaminants after sealing. However, when filling with liquid argon, either as part of a re-circulation system or to replace boiled-off argon, contaminants from the filling argon can add impurities to the system. Argon is produced through the distillation of air, and research-grade argon can contain the other impurities found in air, such as water vapor, oxygen, and nitrogen. These are initially limited to less 1 part per million from the raw supply. A filtration system within the cryosystem during operation can reduce the water and oxygen to less than 100 parts per trillion. Given how inert nitrogen is, it is difficult to reduce nitrogen impurities from the system once introduced.

Another way for impurities to enter the system is through outgassing of the detector apparatuses inside the cryostat, in particular in the region just above the liquid argon where gaseous argon would exist. Though components submerged in liquid argon would have outgassing attenuated, absorptive material, such as plastic, that is not submerged can add contaminants to the gaseous argon above the liquid surface which would eventually be re-introduced to the liquid phase during re-circulation.

Recombination

Once ionization occurs, not only can the produced electrons be captured by contaminants, as discussed in the previous section, but also by the bulk argon. As ionization occurs on an argon atom, the argon atom is left with an overall positive charge. Moreover, there are other argon ions nearby from other instances of ionization. When charge is liberated from the argon atom, it can be immediately re-collected by a nearby argon ion, reducing the amount of charge that drifts toward the wire planes. Theoretically, this collective charge density due to multiple ionizations can be considered in a cylindrical region surrounding the ionizing particle's trajectory under the columnar model [23].

There are two models used to account for recombination effects: the Birks model [24] and the Box model [25]. The Birks model assumes the ions and electrons in the cylindrical region around the ionizing particle to be described by a gaussian distribution during the recombination phase, and assumes an identical charge mobility for both the electrons and ions. In the Box model, electron diffusion and ion mobility are considered to be negligible. In these models, the electron-ion pairs per unit length, the electric field, the average ion-electron separation and the angle of the particle relative to the direction of the electric field all affect the expected fraction of electrons surviving recombination; the Birks model also includes electron diffusion. Depending on which energy deposition range is probed, these models produce different expected results, and so each model can only be used in a particular regime: the Birks model is used for recombination for low dE/dx deposition, and the Box model is used for higher dE/dx . ArgoNeuT, a predecessor to LArIAT, has measured the recombination factors for that experiment [5]. As LArIAT uses a refurbished version of the ArgoNeuT TPC, LArIAT also uses the same recombination parameters.

Space Charge

As the LArTPC becomes more used, and as more ionizations occur, particularly from cosmic muons, there will be a buildup of positively charged argon ions left in the detector, slowly drifting toward the cathode. Over time, these excess argon ions, or “space charge”, can alter the electric field inside the detector, changing the drift velocity of nearby ionized charge. This can directly affect reconstruction of the event; if the drift velocity changes due to distortion of the electric field from space charge effects, the time of arrival at the anode planes will be affected, and the reconstructed position of the ionizing particle will be incorrect. For larger, surface-level, experiments, this can cause variations of up to 5% in the localized electric field [26]. For a smaller experiment like LArIAT, which has a smaller drift volume, this is a sub-dominant effect.

2.3.2 Scintillation Light

Along with deposited charge in the detector, a charged particle can also deposit energy onto the liquid argon that is emitted through scintillation light. This section discusses light production and detection in a LArTPC.

Scintillation Process

From table 2.1, scintillation light from LAr emits at 128 nm. Figure 2.5 shows the emission spectra for argon, as well as other noble elements [27]. How much light is produced and how much light arrives at a light collection system depends on many factors, including the argon purity, the electric field and $\frac{dE}{dx}$ of the particle. Similarly, from table 2.1, approximately 40k photons/MeV are produced in liquid argon due to scintillation. There are two methods by which argon will scintillate due to interactions with a charged particle, both through the de-excitation of dimers [28]. The first case, “self-trapped exciton luminescence”, occurs when a charged particle is absorbed on the atom, leaving the argon atom in an excited state. This excited argon traps another argon atom in the bulk, creating a dimer state which de-excites and scintillates. The second case, “recombination luminescence” occurs when a charged particle ionizes an argon atom by removing an electron. Similar to the first case, the charged argon ion combines with another argon atom and recombines with the thermalized electron cloud, creating a dimer state which scintillates.

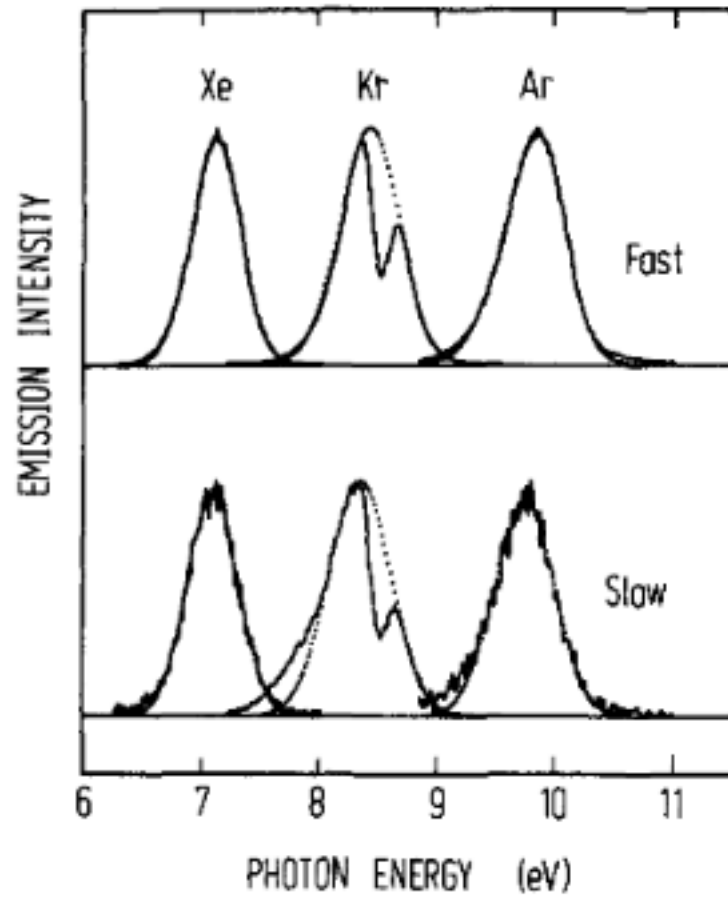


Figure 2.5: Emission spectra of the fast and slow component of xenon, krypton and argon [27].

Dotted lines represent gaussian fits to the data.

Dimers exist in two states: a singlet and triplet state. Depending on state, the dimer has a different radiative decay constant; for the singlet state, this is 6 ns, for a triplet state, it is approximately 1500 ns. Moreover, depending on the method by which the excitation occurs, the probability of being in a given state is different. “Self-trapped exciton luminescence” creates a singlet state around 65% of the time and a triplet state 35% of the time. “Recombination luminescence” creates singlet and triplet states with roughly equal probability.

The light yield is affected by the electric field and the dE/dx of the ionizing particle. With a stronger electric field, there is a greater spatial separation between the argon ions and the free electron cloud, which makes recombination more difficult, decreasing light yield. However, this also makes ionization easier, as electrons require less energy to free, boosting the charge deposition. Therefore, there is an anti-correlation between light yield and charge deposition, as a function of electric field. With more highly ionizing particles, the recombination effect, and hence light yield, increases, as recombination is correlated to the local ionization density. Compared to minimally ionizing particles (MIPs), more heavily ionizing particles will create more light in the LArTPC.

Light Yield Reduction

At 128 nm, scintillation from argon de-excitations are not energetic enough to re-excite the bulk argon, thereby making argon transparent to its scintillation light. This is one of the appealing factors of using liquid argon as a detector medium. However, there are effects which could reduce the light yield reaching the light collection system. In an ideal detector, Rayleigh scattering would be the dominant mode for light reduction, as it would scatter the direction of light propagation through the detector. Experimentally, the scattering length is 66 cm, which is short enough to be a problem even on smaller scale experiments like LArIAT [29]. For detectors that use light information to find a start time for the event, scattering can also cause a problem, as well as make it difficult to combine the charge and light coming from the same particle. Triangulating the source of the light can be done with a light collection system with multiple collection points, which could be compared to 3D position reconstruction using charge deposition. If the light scatters, the position of the light will be affected, making that match difficult.

Though argon is transparent to its scintillation light, the impurities in the argon can absorb

the light directly, reducing the total yield. Moreover, if an excited dimer is close to an impurity, quenching can occur where the dimer transfers energy to the impurity instead of scintillating. This quenching is dependent on how long the dimer exists, so dimers in triplet states, which radiate on a slower time scale, are more likely to come in contact and interact with an impurity, leading to an overall reduction in light yield from triplet states. As water and oxygen can be more easily removed via filtering, quenching and absorption on these impurities is not as problematic. However, nitrogen, being inert, is more difficult and expensive to filter, and therefore is present in the argon at whatever level is provided by the vendor, and is the main impurity leading to light yield reduction.

Wavelength Shifting

Most cryogenic light collection detectors, such as photomultiplier tubes (PMTs) or silicon photomultipliers (SiPMs) cannot detect light at 128 nm. Therefore, in order to collect the light from argon scintillation, a wavelength shifter must be applied to produce light at a wavelength the light collection system can detect. Most experiments use 1,1,4,4-Tetraphenyl-1,3-butadiene (TPB) as a wavelength shifter. TPB absorbs ultraviolet light and re-emits visible light around 430 nm [30], at a ratio of visible:UV=1:2.1 photons [31].

There are multiple ways to implement TPB with a light collection system. TPB can be evaporated directly onto the PMT surface to shift the wavelength as it arrives. Similarly, acrylic plates can be installed in front of the PMTs with TPB evaporated on the plates. These methods are useful because they preserve directionality of the light which can be used to determine position. However, PMTs are best used to probe the volume of the detector in front of it. Therefore, light yield will be diminished from regions near the corners of the TPC, where the light has fewer available trajectories to reach the PMTs. Other experiments, instead of evaporating TPB on or near the PMTs, evaporate TPB on foils mounted to the sides of the TPC. This will reflect light from all directions throughout the TPC, allowing the PMTs to collect it. While directionality is sacrificed, light yield throughout the TPC is increased as well as independent of the source position in the TPC. This also allows light from the corners of the TPC to be collected. For experiments that focus on observation and not positional reconstruction, such as dark matter experiments, TPB coated foils around the TPC are more applicable. Neutrino experiments, which care about position

reconstruction of the interaction, use TPB coated PMTs. Future experiments may find a way to leverage both methods in a hybrid system.

2.4 Event Reconstruction

In this section, the reconstruction of an event is described, where these signals are processed to create 3D track objects. This reconstruction is done in LArSoft, an analysis framework developed to use in the reconstruction of LArTPC events. The stages of reconstruction are: deconvolution, hit reconstruction, clustering, 3D tracking and calorimetry. Figure 2.6 shows a cartoon for each stage of the reconstruction [18].

2.4.1 Deconvolution

Signals left on the anode planes have different shapes, depending on which plane is being readout. For the induction planes, the signal has a bi-polar shape. As electrons approach an induction plane wire, a negative pulse is induced; once the electron passes and moves away from the wire, a positive pulse is induced, in accordance with Faraday’s Law. As the electrons are physically collected on the collection plane, the signal on those wires are unipolar. The first stage of reconstruction, deconvolution, tries to correct for these detector effects by creating similar, unipolar signals on each wire. This allows future stages to treat signals identically, regardless of plane. Some experiments add a noise filtering stage here to remove cross talk. For LArIAT, cross talk was minimal, so no noise filtering was necessary.

2.4.2 Hit Reconstruction

Once signals have been deconvolved, the waveform from each wire is scanned to find possible hits using a peak finder. Once a peak is found, a gaussian is fit to the pulse, and the associated fit parameters are saved, such as peak hit time, height, area under the fit, and the χ^2 for the fit. Each pulse fit is a possible “hit” in the detector.

It is also worth noting that each the shape of each hit is dependent on the trajectory and species of the ionizing particle that liberated the electrons that were collected at the wire planes. If

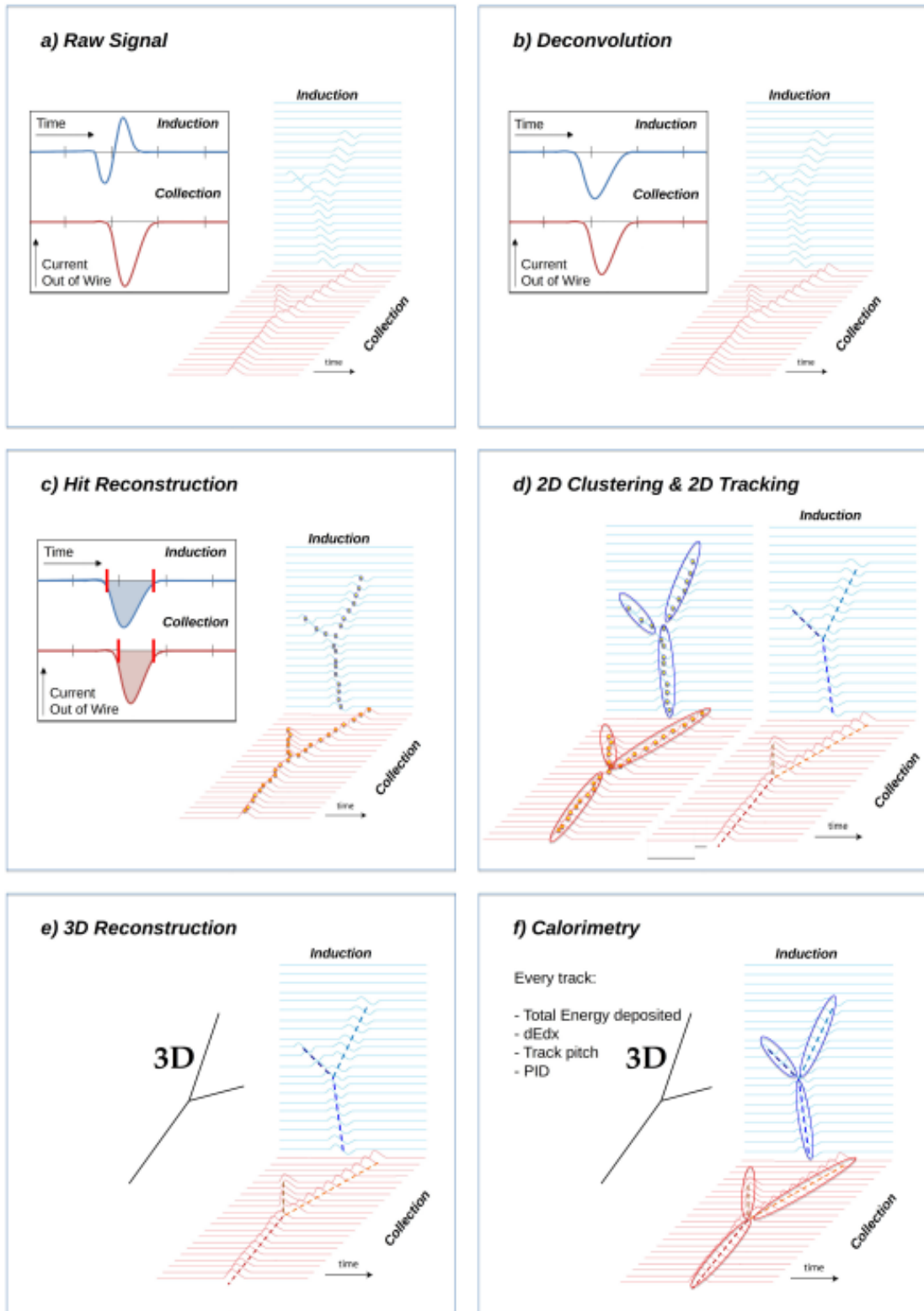


Figure 2.6: The stages of event reconstruction from signals to 3D tracks with calorimetry.

a particle is moving along the drift direction, for example, a cosmic muon which pierces the cathode, travels through the detector and exits at the wire planes, few wires will have a signal left on them, and the pulses on those wires will be wide. The time when charge arrives at a wire corresponds to the position along the drift direction where the charge was deposited. As this example muon travelled through the side of the detector, it deposited charge at most allowable positions in the drift direction, and therefore at many time bins in the wire readout, creating a wide pulse on the a few wires. Conversely, a particle travelling perpendicular to the drift direction will leave narrow pulses on many wires, as the particle travelled in a small range of values in the drift direction, and therefore at a small range of time bins for any given pulse on a wire. Moreover, as the track perhaps travelled the entire length of the detector, many wires will see a signal from this particle. Regardless of particle trajectory, the integral of the pulse left on a wire is proportional to the amount of charge deposited on the wire, which is also related to how much energy was deposited in the detector by the ionizing particle to liberate that drift charge. Therefore, particle species also determines the size of the pulse, as more highly ionizing particles will leave larger pulses on a wire compared with a minimally ionizing particle.

2.4.3 Clustering

With individual hits reconstructed in the TPC, the next step is to group hits over many wires together, provided the hits are in the same plane, to find “clusters”. This stage attempts to create a wire-time “view” of the event, with each plane providing a different “view”. Many algorithms exist to perform clustering, but for this analysis, Trajcluster was the algorithm [32] that was used, and is explained in this section.

Trajcluster begins with a hit in wire-time space, and steps toward the next nearby hit to create an initial trajectory. As the algorithm steps to the next candidate hit to add to the leading edge of the trajectory, some checks are applied to ensure the candidate hit should be added to the previously established trajectory. Some of these checks include:

- the goodness of fit of the candidate hit,
- the charge of the hit compared to the average charge and RMS of the hits already contained in the cluster,

- the goodness of the trajectory fit with and without the new hit,
- the angle between the lines formed by the collection of hits before and after the considered hit in the trajectory.

The last bullet is applied to all hits already in the cluster when a new hit is to be added. It protects against hits that might make sense for the cluster as part of the leading edge of the trajectory, but becomes an outlier when hits before and after the questionable hit are considered. Once all hits have been considered for clustering, some hits may not have been attributed to a cluster, and therefore are ignored for future steps. Clusters, and the hits contained within them, that survive are then matched across planes in 3D tracking.

2.4.4 3D Track Reconstruction

Clustering provides multiple 2D views of the events, one per wire plane. However, information from one plane alone is not enough to know the actual position of the ionizing particle; information from multiple planes need to be combined to create a 3D track. Starting with clusters from different planes that are nearby in time, the reconstruction creates a tentative 3D trajectory of the track using the bounds of the clusters that are time matched. This tentative trajectory is projected back into the wire planes, and adjusts the fit parameters to find the best possible fit using all the hits contained in the clusters that are being considered for the track. Multiple clusters from a plane may be used to create a track, but a cluster can never be broken at the track building stage. When completed, a 3D view of the event is achieved.

2.4.5 Calorimetry

Now that all the tracks for the event has been reconstructed, the individual hits used for the track can be used for calorimetric reconstruction. One of the variables saved for each hit is the total integral of the fit applied to the pulse. This integral is proportional to the total charge deposited by the hit. Correcting for the detector effects discussed in previous sections, such as electron lifetime and recombination, a total charge deposited at the source can be calculated, and via the properties in table 2.1, can be translated into energy. Therefore, the collection of hits in a track can be

896 used to find the total energy loss of the particle in the TPC. For neutrino experiments, the energy
897 of particles produced at a neutrino interaction can be used to infer the energy of the neutrino at
898 interaction. For charged particle experiments, such as LArIAT, if a measure of the particle's energy
899 before entering the TPC can be obtained, using the energy deposition from calorimetry can provide
900 the energy at interaction of the charged particle to be used for a cross section measurement.

Chapter 3

The LArIAT Experiment

LArTPCs are ideally suited for neutrino research, and as described in previous chapters, LArIAT can provide a vital contribution to those experiments through analysis of charged particles that would be a common daughter of a neutrino interaction. For example, figure 3.1 shows the expected momentum spectrum of daughters from a neutrino interaction in DUNE [33] along with the measured momentum spectrum of positively charged particles used in this analysis. As is evident from these plots, the momentum range that LArIAT is analyzing coincides with DUNE’s expected daughter momentum distribution. Therefore, an analysis of particles in LArIAT and development of reconstruction techniques for these particles can be directly translated to neutrino experiments like DUNE that expect to see these same particles in the same energy range.

Using the basics of LArTPC design described in chapter 2, this chapter explains the LArIAT experiment, including the detector hall and beam conditions provided to the experiment, the auxiliary detectors used for particle identification before the TPC, and the specific design and specifications of the LArIAT TPC.

3.1 Fermilab Test Beam Facility

LArIAT was housed in the Fermilab Test Beam Facility (FTBF) (figure 3.2), which exists along the Meson Center beamline. Beam begins in the linear accelerator where protons are accelerated to 400 MeV. From there, beam continues into the Booster, where the energy is increased to 8 GeV, then

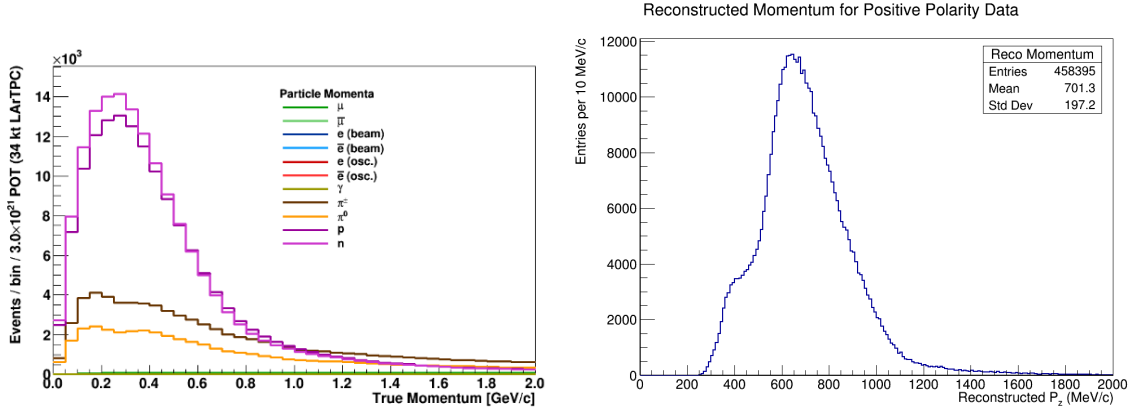


Figure 3.1: Left: Simulated momentum spectra from daughters of neutrino interactions [33]. Right: LArIAT momentum spectrum for Run II, positive polarity, high yield tracks.

into the Main Injector where the protons reach their maximum energy of 120 GeV. This 120 GeV beam is the “primary” beamline. From this, the beam is split into multiple beamlines and sent to various high energy experiments. One of these lines provides beam to the Meson experiments. The Meson line is split in two, the MTest line, and the MCenter line. The MCenter line has a Tungsten target for the 120 GeV protons from the primary beam to collide. Particles created from interactions in the target can be selected based on energy and charge using a series of magnets. For the LArIAT beamline, 64 GeV π^+ were selected. This π^+ beam is what enters the detector hall, and is called the “secondary” beam.

In neutrino experiments, often the pions produced in a neutrino interaction have energies on the order of 1 GeV (fig 3.1). Therefore, this 64 GeV beam is still too energetic for the purposes of LArIAT. To select a lower energy range, a copper target is placed in the secondary beam. This target is in a collimator oriented 13° to the secondary beam, creating a tertiary beamline at this angle. It is along this tertiary beamline where the detectors used for LArIAT are placed. Though high energy beam continues along the secondary beamline through the copper target, none of the LArIAT detectors are in the path of this beam. As described in 3.2.2, dipole magnets in the LArIAT tertiary beamline allows for the selection of particles in the momentum range necessary for study.

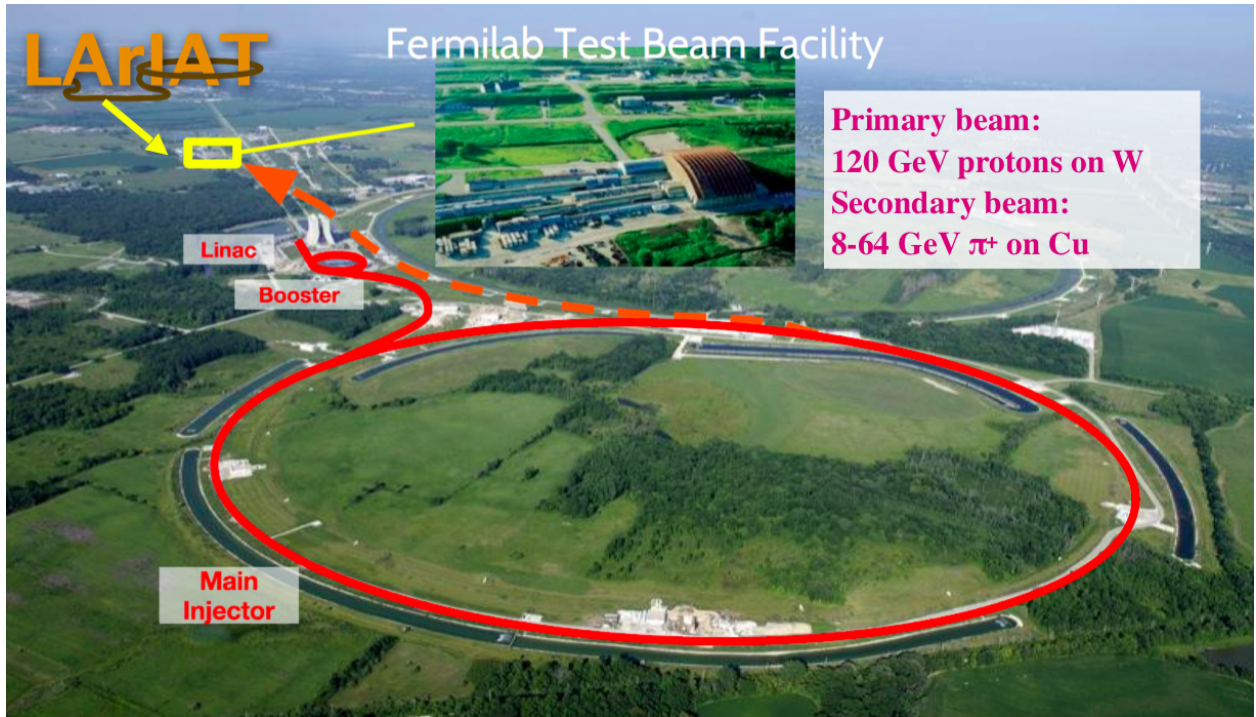


Figure 3.2: Overhead picture of Fermilab with beam path through the various particle accelerators. The Fermilab Test Beam Facility (FTBF) and beam energy conditions in insets.

3.1.1 Accelerator Beam Conditions

The accelerator operates on a 60.5 s supercycle. Though other experiments receive beam throughout the supercycle, LArIAT took beam for only 4.2 s per supercycle. The rest of the supercycle was used for cosmic data taking and file I/O data management. This 4.2 s of beam taken per supercycle is called a “spill”.

Within each 4.2 s of beam, there is additional structure, as pions are sent in pulses, instead of a continuous beam. Each pulse, or “bucket”, of beam is 2.2 ns long, with a 18.8 ns gap between pulses. Therefore, the center-to-center bucket time spacing is 21 ns. This 21 ns time spacing is important, as it affects the Time-of-Flight measurement (section 4.1). Buckets are grouped into “batches”, consisting of 84 buckets. Similarly, batches are combined in groups of seven to create an “orbit”. An “orbit” lasts for:

$$\frac{21 \text{ ns}}{\text{bucket}} * \frac{84 \text{ buckets}}{\text{batch}} * \frac{7 \text{ batches}}{\text{orbit}} = \frac{12.348 \mu\text{s}}{\text{orbit}} \quad (3.1)$$

However, the accelerator does not send beam for one of these batches per orbit. Therefore, beam

is sent for six batches, then there is an empty batch, followed by another six batches of beam, and so on. This process repeats for the full 4.2 s of beam. During running, the intensity of the beam sent to LArIAT was tuned to receive more or less beam, as needed. Often, the intensity of the beam was set to maximize the number of triggers while keeping the TPC from becoming too busy during a readout; if the intensity was too high the TPC would have too many particles during a readout and the reconstruction for the event would be unreliable. Deciding upon an intensity was at the discretion of the shifter, who could see event displays of the TPC in real-time. As such, the intensity varied greatly over the runtime of the experiment. Before the target and at certain positions within the beamline, there were scintillator counters to measure the intensity of the beam entering the experiment hall as well as the occupancy of particles traversing the beamline. In particular, the scintillator counter approximately 1 m upstream of the target was useful, not only for beam intensity monitoring, but also for simulation (see Section 6.3).

3.2 LArIAT Auxiliary Detectors

LArIAT has an array of auxiliary beamline instruments to measure various kinematic quantities of the beam as particles traverse the beamline. Two beamline detector systems exist in LArIAT that were used for this analysis: the Time of Flight paddles and the Wire Chambers. Other detector systems, such as a series of Aerogel detectors, a halo veto paddle in the beamline, a cosmic muon tower to trigger on cosmic muon events, and a muon range stack for particles exiting the TPC were included in the beamline, but information from them were not used for this analysis. Figure 3.3 shows an overhead diagram of the experimental hall. An overview of each auxiliary detector system used in this analysis is given in this section, with an explanation of the cryogenic system and TPC in subsequent sections [34].

3.2.1 Time of Flight

A time of flight (TOF) system exists to provide a measurement how long it takes particles to travel through the beamline. Two scintillator paddles were used during running conditions, bookending the wire chamber system. The upstream TOF (USTOF) paddle had an active area of 10 cm x 6

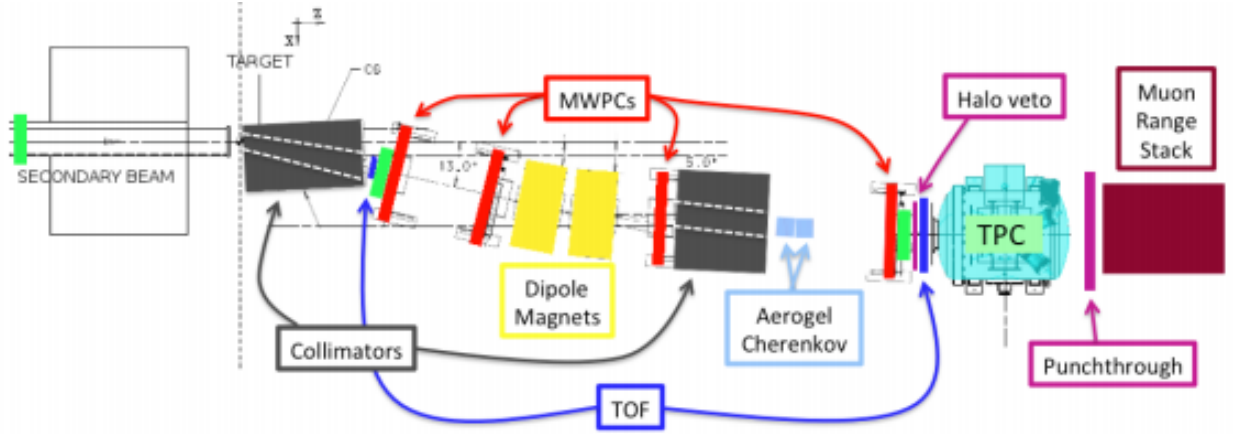


Figure 3.3: Schematic of beamline detectors and TPC. Only information from the MWPCs, TOFs and TPC were used for this analysis.

974 cm x 1 cm, with light guides and a PMT on either side of the paddle, and was rotated 13° in the
 975 XZ plane. The downstream TOF (DSTOF) paddle was 17 cm x 17 cm x 1 cm, with a PMT at
 976 each corner of the paddle, and was rotated 3° degrees in the XZ plane. Each paddle was made
 977 as thin as possible to reduce the energy loss due to ionization in the paddle as well as reduce the
 978 probability of interacting in the paddle. Each paddle had a readout of 3072 samples, with 1 ns
 979 per sample. When a trigger is issued (section 3.5), data from the PMTs are read out and stored,
 980 starting approximately $8.4 \mu\text{s}$ before the trigger time.

981 3.2.2 Wire Chambers and Bending Magnets

982 The wire chambers, in conjunction with the bending magnets, are used as a spectrometer to mea-
 983 sure the momentum of a particle traversing the beamline. The wire chambers are based on Fenker
 984 proportional wire chambers [35]. Each wire chamber has two wire planes, oriented vertically and
 985 horizontally, each with 128 wires spaced 1mm apart. The wire chambers are filled with an 85/15
 986 mixture of gaseous argon and isobutane, which allows ionization of electrons when a charged par-
 987 ticles passes through the active volume. The wire chamber operating voltage varied over runtime,
 988 but was usually between 2400 and 2500 V. The first two wire chambers, similar to the target,
 989 upstream collimator and the USTOF, were rotated 13° in the XZ plane. The second pair of wire
 990 chambers were rotated 3° , similar to the DSTOF.

Wires are readout by a Time-to Digital Converter (TDC) with 64 wires per TDC, for a total of 4 TDCs per wire chamber. Each wire readout lasts for 1024 samples, with each sample representing approximately 1.19 ns. The efficiency of each wire chamber to register a hit was tested in a proton beam, and found to be 98-99% efficient. When a trigger is issued, a digitized readout is stored in a $1.2\mu\text{s}$ window starting approximately 300 ns before the trigger time.

Two dipole magnets are used to bend charged particles as they travel through the beamline. The first magnet was rotated by 10.5° and the second magnet by 5.5° , both rotated in the XZ plane. By choosing the current and polarity passing through the magnets, a selection based on particle charge and momentum can be applied. During operation, a maximum of 100 A was passed through the magnets, equating to an approximate magnetic field of 0.34 T. However, as this would easily cause overheating of the magnets if the current flowed continuously, the magnets were only pulsed when beam was being sent to the detector hall. Chilled water lines through the magnets and fans provided extra heat management. Figure 3.4 plots the maximum field as a function of current for both magnets.

As the current is the parameter that is recorded for an event, the data sets are divided into current ranges. For example, this analysis focuses on data near 60 A and 100 A.

Between the third and fourth wire chamber was a second steel collimator, also rotated at 3° to be in line with the beamline instruments downstream of the magnets. This collimator shielded the fourth WC and DSTOF from any particles that may have been created from an incoming particle impinging upon the steel of the magnets and creating daughter particles downstream. The collimator aperture was larger than the size of an individual wire chamber, so it is unlikely particles with a nominal trajectory would impinge on the collimator steel itself.

3.3 Cryogenic System

3.3.1 Cryostat

As argon must be cooled to 87 K to reach a liquid state, a cryogenic system and cryostat is necessary to contain the TPC and the liquid argon. The LARIAT cryostat, shown in figure 3.5, is a cylindrical vacuum-jacketed vessel with convex end caps. The inner vessel houses the TPC and liquid argon,

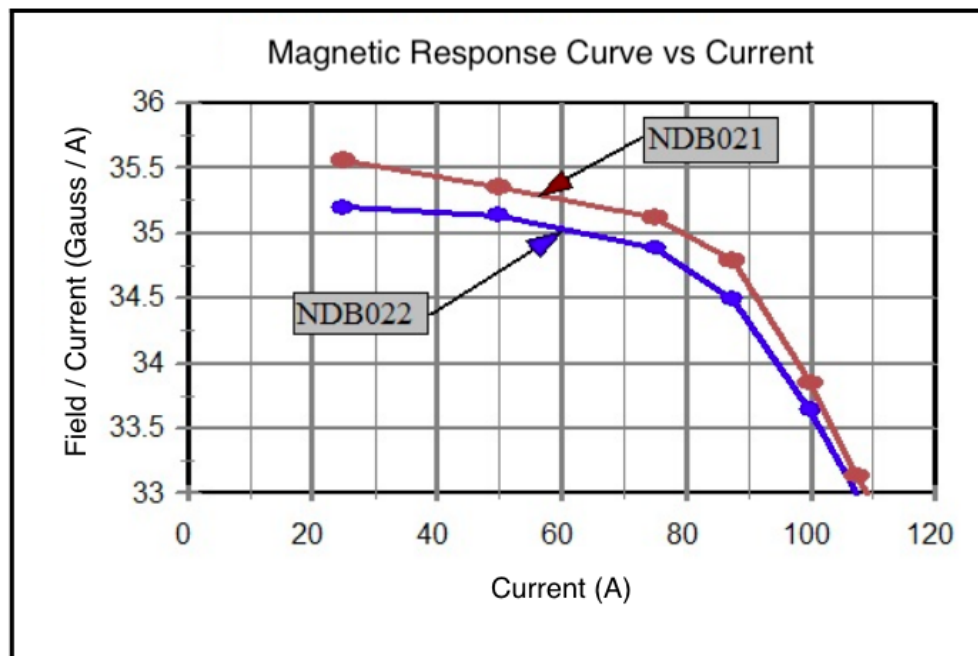


Figure 3.4: Field per unit current vs current for the two magnets used for LArIAT. NDB021 (red) is the response curve for the upstream magnet. NDB022 (blue) corresponds to the downstream magnet.

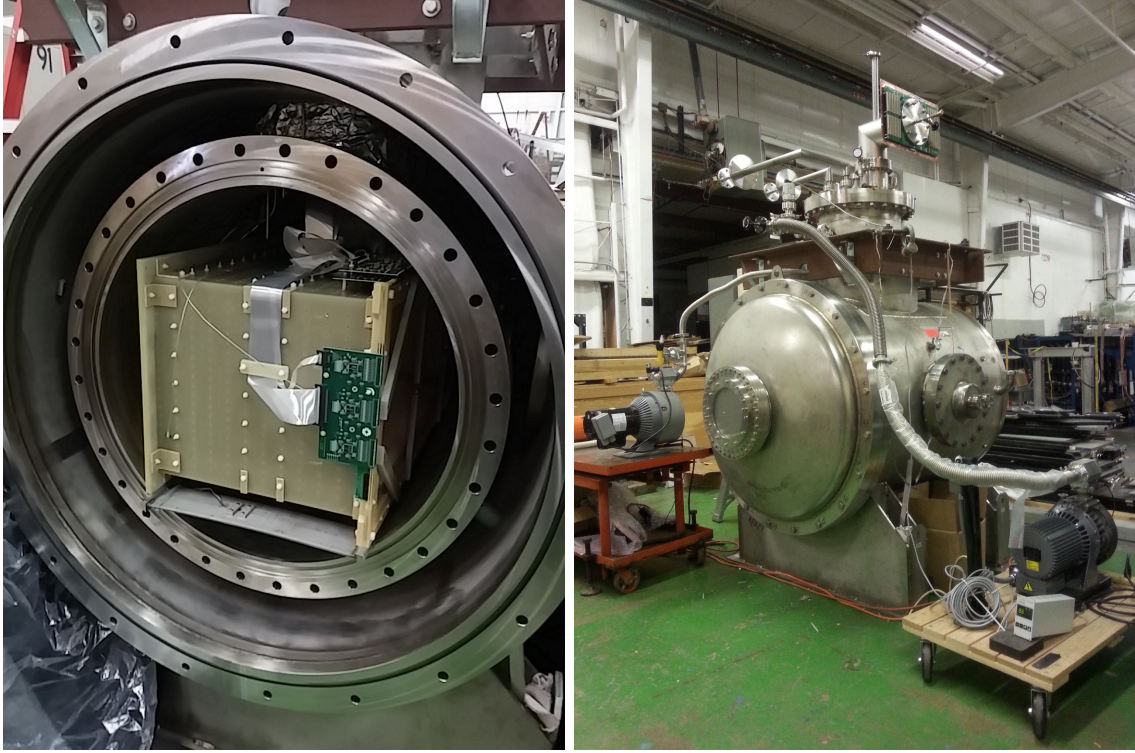


Figure 3.5: Left: Open cryostat with TPC installed. Right: Cryostat sealed before installation at FTBF. The chimney for signal cables and HV feedthrough extends from the top of the cryostat and a port for the light collection system is on the picture right side of the cryostat.

is 76.2 cm in diameter and 130 cm in length, and capable of holding 550 L of liquid argon. The outer vessel is vacuum sealed for thermal insulation. Access to the cryostat is available through either end cap. At the top and mid-length of the cryostat is a chimney that allows a feedthrough for signal cables to the wire planes as well as high voltage to the cathode. Mid-length on the anode side of the cryostat, visible in figure 3.5, is a flange allowing access to the light collection system.

Given the end cap where the beam enters the cryostat is convex, there is a volume of argon that exists in a region in front of the TPC. Interactions and charge deposition cannot be measured in this dead region. To minimize how much dead argon exists in front of the TPC, a concave hollowed-out region was added by installing a concave cap on the inside of the inner end cap, that is also held at vacuum. This “excluder” cap extends to within a couple centimeters of the front face of the TPC. With this, instead of a steel wall and approximately 25 cm of dead argon in front of the TPC, there is a concave vacuumed space, a thin steel wall and <5 cm of dead argon before

the TPC. The change of dead argon to vacuum reduces the ionization and interaction rate in this uninstrumented region of the cryostat.

3.3.2 Liquid Argon Purification System

LArIAT's argon supply came from a commercial dewer outside the detector hall, filled using research-grade liquid argon. The most common impurities were oxygen, water and nitrogen, and were usually filtered to <1 ppm by the vendor. However, the acceptable contamination is only 100 ppt, so additional filtering is necessary.

Argon is pumped from the outside dewer into the purification system, which is based on the Liquid Argon Purity Demonstrator (LAPD) [36]. The purification filter is a 77 L container which is half filled with a 4 Å molecular sieve. This sieve not only removes water, but also small amounts of nitrogen and oxygen. The second stage of the filter consists of copper oxide embedded in alumina, which removes oxygen. In combination, this filter removes most of the oxygen and water impurities from the argon supply, as well as a small amount of nitrogen.

After filtering, the argon is pumped through the bottom of the cryostat into the inner vessel. As there is no re-circulation system, argon naturally boils in the cryostat and is vented into the atmosphere. Once the liquid argon level drops below a threshold, more argon is pumped from the dewer through the filtration system and into cryostat to refill it. This ensures the cold electronics and high voltage feedthrough connection are fully submerged. Refilling of the cryostat occurs multiple times a day. Argon levels, temperature, pressures and filling stages are all monitored in real time. Figure 3.6 shows a screenshot of the monitoring page for all of these variables.

3.4 LArIAT Time Projection Chamber

3.4.1 Cathode Voltage and Field Cage

The TPC active volume (47 cm x 40 cm x 90 cm) is enclosed by the cathode and field cage. Given the drift distance of 47 cm and a desired electric field of approximately 500 V/cm, a voltage difference from cathode to anode of 23.5 kV is required. Voltage is provided to the cathode through the high

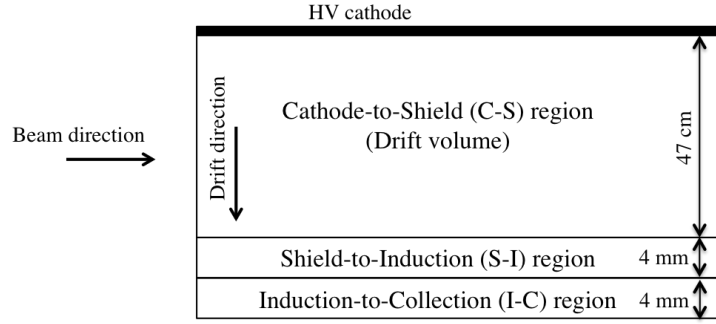


Figure 3.7: Diagram (not to scale) showing the regions of the TPC created by the placement of the cathode and three wire planes.

voltage feedthrough in the cryostat chimney. For the run period for which data was used for this analysis, the cathode was a sheet of copper mounted on G10 plastic such that the copper sheet completely covered the inner surface of the cathode side of the TPC; subsequent runs replaced the copper sheet with a mesh cathode. The field cage which comprises the four sides of the TPC other than the cathode and wire planes consists of G10 with a series of 1 cm wide copper rings connected on the inner surface of the plastic, with each ring separated by 1 cm. On the outside of the TPC were $1\text{G}\Omega$ resistors to connect one series of rings to the next. Each ring was connected through 4 resistors in parallel, providing a ring-to-ring resistance of $250\text{ M}\Omega$. This gradually stepped down the voltage across the TPC, ring by ring, such that a constant 500 V/cm electric field was maintained in the active volume.

3.4.2 Anode Wire Planes

After 47 cm of drift volume are the anode wire planes where signal from the detector is collected. There are three wire planes: the shield plane, the induction plane, and the collection plane. The wires were made of $152\text{ }\mu\text{m}$ diameter copper-beryllium wires, with a 4 mm wire-to-wire spacing. Each plane had a different orientation of wires. The shield plane consisted of 225 wires, which were oriented at 0° with respect to the vertical, while the induction and collection planes consisted of 240 wires oriented at $\pm 60^\circ$ with respect to the vertical. Using G10 spacers between the wire planes, the distance from plane to plane was set to 4 mm. Figure 3.7 shows a diagram of how the cathode and wire planes were oriented in the TPC.

Run Period	Pitch (mm)	Cathode (V)	Shield (V)	Induction (V)	Collection (V)
Run I	4	-23164	-298	-18.5	338
Run II	4	-23164	-298	-18.5	338
Run IIIA	5	-23164	-325	0	423
Run IIIB	3	-23164	-298	-18.5	338

Table 3.1: Voltages for the cathode and wire planes for each run period. This analysis focuses on data taken during run II.

Each wire was held at a tension of 10N before being soldered onto the wire plane frame. This kept the wires taut while on the frame and prevented loose wires from touching or floating in the liquid argon. Loose or touching wires would create cross talk from wires and cause poor reconstruction of information from those wires as they would not be where the reconstruction expected them to be. Every wire on the induction and collection planes was its own RC circuit, with a 2200 pF capacitor and 22 M Ω resistor in series with the wire, producing an RC time constant of 48 μ s. The shield plane was not readout during running, and so was not instrumented with resistors and capacitors. After construction, a series of wires on each plane were tested at random with a function generator to ensure they were acting appropriately as a RC filter and that there were no unintentional shorts in the plane.

The wire planes were set at particular voltage to satisfy transparency conditions, which are a function of the voltage of the cathode and wire planes, as well as the geometry of the wire planes themselves. These conditions ensure that drifting charge is only collected on wires at the collection plane, and creates induced signals on the induction plane and the shield plane, if the shield plane were instrumented. Table 3.1 shows the voltages for all the run periods during the experiment. Note the difference between the cathode and the collection planes is 23.5 kV, which maintains the 500 V/cm electric field.

3.4.3 TPC Readout

Each of the 480 instrumented wires is individually read out. As the signal on each wire due to drifting electrons is small, some amplification of signal is needed. Mounted on the TPC frame

are a series of cold amplifier motherboards hosting ASICs. These were designed to operate while submerged in liquid argon, and are the same design as the ASICs used for MicroBooNE [37]. Using cold electronics improves the signal-to-noise ratio, compared to the warm ASICs that were used in ArgoNeuT, the predecessor experiment to LArIAT which used this TPC. With an amplification setting of 25 mV/fC, the charge deposition on a wire, which is around 3.5 fC, produces an amplified signal of 90 mV.

Signal is carried from the cold motherboards to warm receiver/driver cards (WRDs) mounted outside and above the cryostat through ribbon cables that exit the cryostat through the chimney. These cards convert the single-ended TPC signals into differential signals. The signal is then transferred away from the cryostat to the electronics racks a few meters away where they are processed by a set of D2S-64 cards. These cards reconvert into a single-ended signal to cancel common mode noise, and provide enough current for the digitizers. The digitizers used for LArIAT were a series CAEN V1740 boards, with 128 ns sampling time, and a total of 3072 samples per event, for a total readout time per wire of 393 μ s. A 90 mV signal from the ASICs corresponds to a peak amplitude in the digitizers of 180 ADC. The digitized signal from the V1740s are what are saved and used for reconstruction. Figure 3.8 shows a diagram of the electronics readout apparatus.

3.4.4 Light Collection Systems

As described in chapter 2, a light collection system can also be used to collect light produced from interactions in the argon. Multiple light detection modules were used during LArIAT's operation. Two PMTs were used during data taking: a 3 inch Hamamatsu R11065 PMT and a 2 inch ETL D757KFL PMT. A series of SiPMs were also used during data taking runs, including two Hamamatsu S11828-334M 4x4 SiPM arrays and one single channel SensL MicroFB-60035 SiPM. Each of the three SiPMs had a 6 mm x 6 mm active surface area. LArIAT used TPB (2.3.2) coated foils for Run II as well as TPB coated PMTs. Coating the PMTs allowed for collection of light that came directly from the source without reflecting off of the foils wrapping the TPC. Figure 3.9 shows a picture of the various PMTs and SiPMs used during operation. The system is mounted through the beam right side port visible in figure 3.5. Signals from the light collection system were recorded

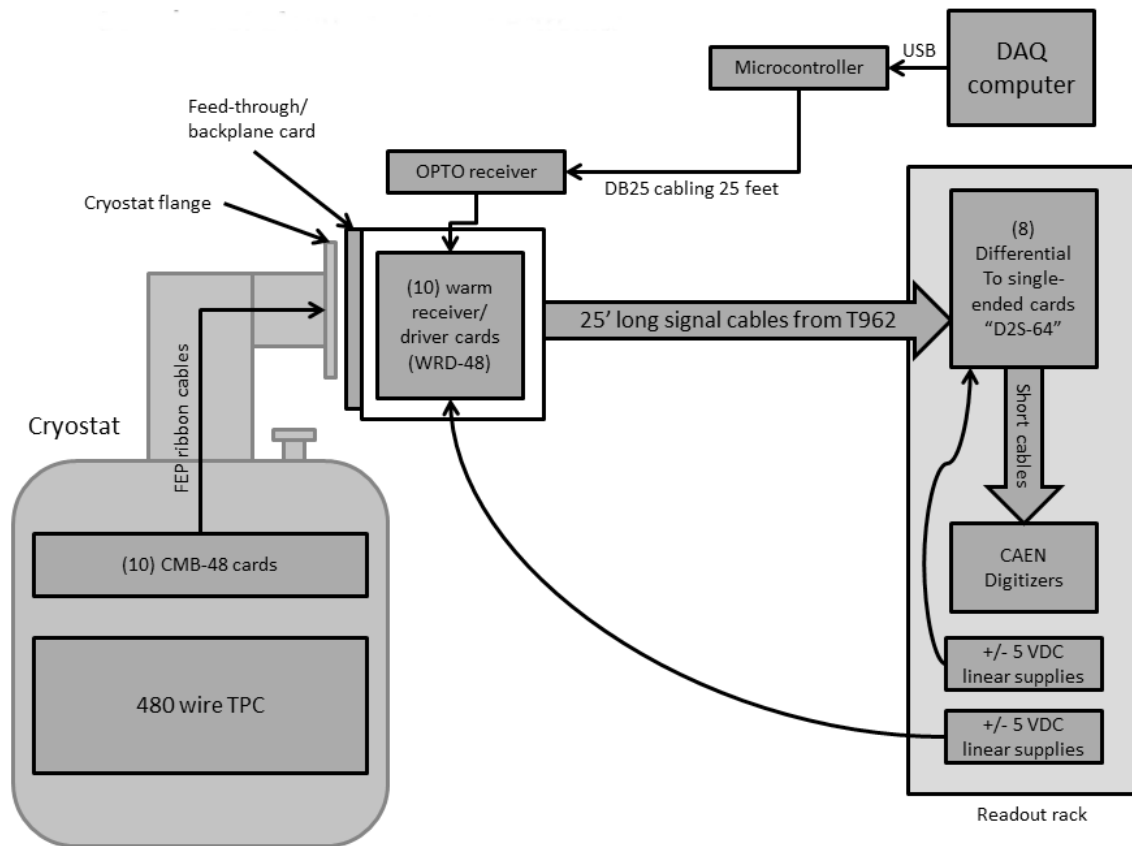


Figure 3.8: Diagram of electronics used to deliver signal from wires to the digitizers.

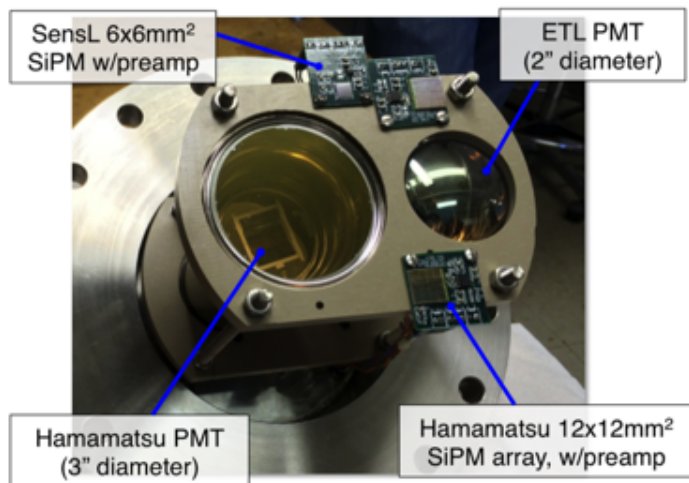


Figure 3.9: Photodetection systems used in LArIAT.

by CAEN V1751 digitizers with a 1ns sampling rate. Discriminated copies of the signal were also sent to NIM crates to be used for various light-based triggers during running conditions.

3.5 Trigger Conditions

Using signals from all the detectors, trigger conditions can be created to cause data to be saved. Data buffers from the various systems were fed into a CAEN V1495 to be used for triggering. During running conditions, many trigger conditions were programmed into the FPGA that accompanied the V1495. Every 10 ns, the trigger card would check for coincidence between the various inputs from the detector systems, and if one of the user-defined patterns were met, a trigger would fire. Some trigger conditions were implemented, such as cosmic muon based triggers, that did not require information to be recorded in the auxiliary detectors. However, for brevity, only the beam-like trigger conditions, which are relevant for this analysis, are described.

As explained in 3.1.1, every 60.5 s supercycle, LArIAT receives 4.2 s of beam. When beam is about to be sent to the experiment, and when beam ends, a signal is sent from the accelerator. Between these two accelerator signals, a BEAMON gate is opened. This open gate is one of the inputs necessary for triggers used in this analysis, as this analysis focuses on pions entering the TPC from the beam.

The TOF paddles and wire chambers are also needed to create a trigger, as coincidence among those detectors suggests a charged particle has travelled through the beamline towards the TPC. Each TOF paddle has multiple PMTs. Within a TOF paddle, there must be a coincidence, within 20 ns, of all PMTs in the paddle to register a hit in that given paddle. Assuming both TOF paddles meet this internal coincidence, a coincidence between the pair is checked. As it is expected for there to be a delay between signals from the upstream TOF (USTOF) paddle and the downstream TOF paddle (DSTOF), as a charged particle takes time to get from the USTOF to the DSTOF, a 20 ns offset is applied to the USTOF time that is used for the coincidence with the DSTOF. This 20 ns offset is the expected time of flight for a particle moving at the speed of light, so if a particle was travelling near the speed of light, the 20 ns offset to the USTOF time would create coincidence with the DSTOF to meet the TOF trigger requirement. Obviously, massive particles will move more

slowly, so there is a 100 ns window allowed where this coincidence between the delayed USTOF time and the DSTOF can occur. If mutual coincidence is found, a 100 ns gate is opened.

For a given wire chamber, there are 4 TDCs, with each TDC reading out one half of one axis of the wire chamber. The readout from each TDC is fed to a NIM module which creates a logical OR of the two TDCs in an axis, and then a logical OR of the two axes. When this OR is true, there is coincidence of signals from at least one wire on both axes within a WC, and a 100ns gate is opened. The trigger condition requires 3 of 4 WCs be in coincidence with the rest of the detectors.

The trigger card takes in six logic inputs for a beam-like trigger: the BEAMON signal, the 100 ns gate due to coincidence of the delayed USTOF and the DSTOF, and four 100 ns gates, one for each WC, with 3 of 4 WCs required. If these are in coincidence, a trigger is issued, and the readout buffer for each detector, including the TPC is stored. To review, a trigger is issued under the following conditions:

- The BEAMON signal is being sent from the accelerator complex.
- All PMTs within a TOF register a pulse, within 20 ns.
- With a 20 ns delayed USTOF, find coincidence with the DSTOF, within 100 ns. If so, open a 100 ns gate.
- Both axes of a given WC register a hit, as defined from the NIM module. If so, open a 100 ns gate.
- The BEAMON signal, the TOF system, and 3 of 4 WCs are in coincidence.

Beam-like triggers should have information stored regarding hits in the wire chambers, the TOF paddles, and hopefully, the TPC. By using this information, the kinematics of particles in the beamline can be reconstructed and compared to information in the TPC. The next chapter describes how information from each detector is reconstructed.

Chapter 4

Reconstruction Methods

In this section, the reconstruction of the auxiliary beamline instruments, the time of flight and wire chamber system is given, with a more in-depth analysis of the wire chamber reconstruction. The TPC reconstruction was generally described in section 2.4, so it is not re-explained here.

4.1 TOF Reconstruction

There are two TOF paddles in the beamline, with multiple PMTs per paddle. For the data taking campaign which this analysis used, the upstream TOF paddle had two PMTs, while the downstream TOF paddle had four. Due to timing issues with matching across four PMTs, only two PMTs from the downstream TOF paddle were used. The process for reconstructing a candidate hit time is similar for both paddles, and is described below.

4.1.1 Hit Matching Within a TOF Paddle

Each PMT within a paddle reads out a waveform, at a rate of 1 sample per 1 ns. An example PMT pulse is given in figure 4.1. For a given pulse, the discrete five-point derivative for time sample, i , is calculated using the four nearby samples:

$$f'_i \approx \frac{-f_{i+2} + 8f_{i+1} - 8f_{i-1} + f_{i-2}}{12} \quad (4.1)$$

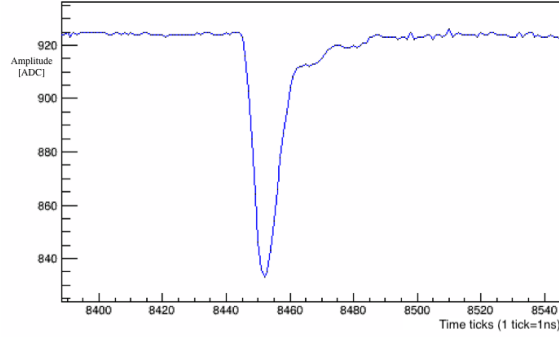


Figure 4.1: Example PMT pulse in a TOF paddle.

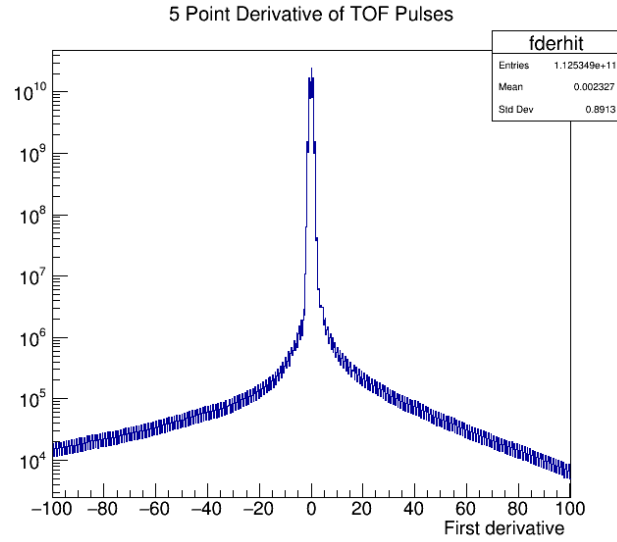


Figure 4.2: First derivative of TOF pulses, in log scale. Hits are registered if the derivative is less than -3.

1187 A hit in a paddle is declared when $f'_i < -3$, which coincides with the falling edge of the waveform.
 1188 Figure 4.2 shows the derivative for all waveforms used in this analysis. This derivative assumes each
 1189 pulse is separated, as the derivative calculation was tuned on single pulse waveforms. However,
 1190 if multiple pulses overlap, the derivative would vary, and would be dependent on the separation
 1191 between the two overlapping pulses. To prevent this, once a hit is found, a 20 sampling dead time is
 1192 added, where another hit cannot be registered. When this pulse overlapping occurs, the hit finding
 1193 method will only consider the first instance where the derivative crosses this threshold.

1194 Once all hits are found in the PMTs within one paddle, the hits between the PMTs are

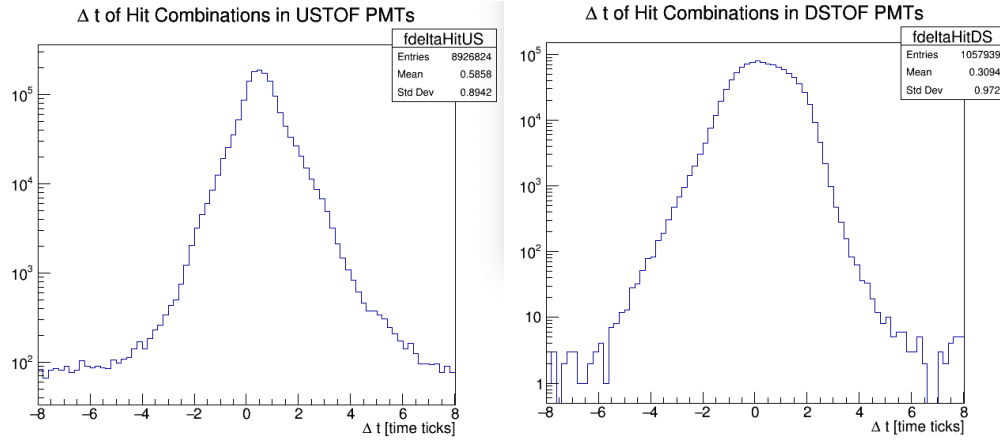


Figure 4.3: Δt between each combination of hits for USTOF (left) and DSTOF (right). Both are in log scale.

compared to find a match. This process ensures that both PMTs confirm the timing of the hit. Each hit in one PMT is compared to each hit in the other PMT, and the Δt between the two is calculated. If the particle went through the center of the TOF paddle, each PMT should register a hit at the same time. However, if a particle passes closer to one PMT, that closer PMT will record a hit earlier than the other PMT. Therefore, a window of acceptable Δt is allowed. For the upstream TOF, the acceptable range for hit matching was $[-1, 2]$ samples. The downstream TOF had a larger range, from $[-2.6, 3.4]$ samples. Figure 4.3 shows this distribution for all combinations of hits in both TOF paddles. If a pair of hits are sufficiently close in time, the hit is confirmed for the paddle.

4.1.2 Calculating The Time of Flight

With the collection of hits in each TOF paddle, possible TOF combinations, $t_{DSTOF} - t_{USTOF}$, are reconstructed using a hit from the USTOF and the DSTOF. Figure 4.4 shows the number of possible TOFs reconstructed per event, and all the possible TOF combinations. A cut is applied where a $TOF < 10$ ns is not considered.

From the TOF plot, the beam timing structure can be seen. As mentioned in subsection 3.1.1, beam arrives in the detector hall every 21 ns. This explains distinct peaks at approximately 60, 80 and 100 ns. These peaks occur when a TOF is reconstructed from different beam pulses. If hits

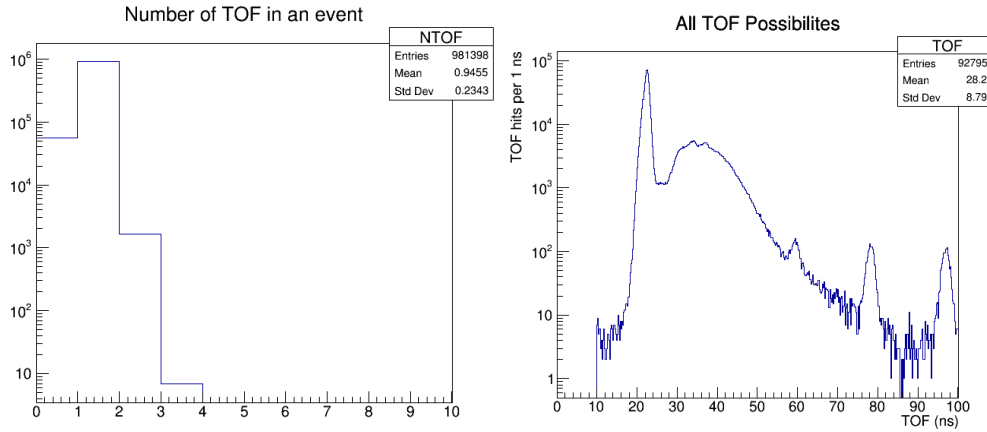


Figure 4.4: Number of TOFs reconstructed per event (left) and all TOF combinations (right), both in log scale. Analyses focus on events with only one TOF.

created from two adjacent beam pulses are used, and assuming the two particles that made the two hits would have the same TOF if this effect were not present, the TOF measured would differ by this 21 ns timing offset. Peaks near 60, 80, and 100 ns are multiples of this 21 ns offset. Moreover, the difference between the TOF of lighter particles, such as pions and muons, and heavier particles, such as protons, is also on the order of 20 ns. Therefore, it is realistic that some of the TOFs returned that seem proton-like (TOF ~ 40 ns) are actually lighter particles (TOF ~ 20 ns) at the DSTOF that were affected by this 21 ns offset.

4.2 Wire Chamber Reconstruction

In order to do a cross section measurement, the energy of the particles in the data set must be known. Though the TPC measures energy loss of a particle within it, it has no knowledge of the energy of the particle as it enters. However, information from the auxiliary beamline detectors can be used to calculate the energy of the particle before it enters the TPC. Using the wire chamber system, the momentum of the particle can be found. This can be translated into kinetic energy, once the mass of the particle is known. On a personal note, as the development of this reconstruction was one of my main contributions to the experiment, I provide a more in-depth explanation of the wire chamber reconstruction.

4.2.1 Wire Chamber Hit Finding

As discussed in subsection 3.2.2, a charged particle passing through a wire chamber (WC) will ionize the gas in the WC and leave a signal, or "hit", on nearby wires in both the X and Y planes. As the WCs are rotated around the Y axis, a signal on an X wire corresponds to both an X position and a Z position, while a signal on a Y wire corresponds the Y position of the hit. With four WCs in the system, this gives four instances where the position of a passing particle can be found.

However in operation, noise effects occur. When a particle passes through a WC, it can leave a signal not only on the nearest wires, but also on the neighboring wires. Moreover, though all 16 TDCs, 4 TDCs per WC, are time synchronized at the beginning of the spill, each TDC seems to have slightly different sampling rates. Over the course of the spill, this causes drift between the measured times of each hit across planes, and creates ambiguity when attempting to time-match hits. Therefore, for each particle and plane, there is not just one wire hit at one time, but a group of wires hit over a span of a couple time bins, with the range of time bins changing depending on which TDC was associated to those wires. Complicating matters more, noisy wires in the WCs can cause a hit to be registered even when no particle passed through the chamber near that position and time.

Given this, the first stage of WC reconstruction is a clustering algorithm that groups hits close in time and space within a wire plane. Once a cluster has been identified, the earliest hit in time within the cluster is saved in a list of candidate hits, and the rest discarded as noise. Finally, if candidate hits associated with different clusters are within one wire and one time bin of each other, the average wire and time of the two is used. This operates as a last catch in case the clustering algorithm created multiple clusters out of a single group of hits. Once the clustering algorithm is complete, each plane in each WC has a list of filtered candidate hits to be passed to next stage of WC reconstruction. Often, multiple particles pass through a WC in a readout window, with each creating a cluster of hits. Therefore, the list of candidate hits for a WC can include multiple X and Y wires, and the number of X wire hits and Y wire hits within a WC need not be equal.

4.2.2 Wire Chamber Track Building

The second stage of WC reconstruction, Wire Chamber Track Building, attempts to match hits across both the X and Y planes within a WC, along with hits in the other WCs, to find the best possible WC Track for the event. Because the X and Y planes are readout independently and suffer from drifting clocks, it is difficult to associate a hit on an X wire to a hit on a Y wire, using timing information. Therefore, all combinations of X hits must be used with all combinations of Y hits to attempt to create a track based on position.

There are two methods by which a WC Track can be reconstructed for an event: A four point track, reconstructed from a combination of four X and four Y hits, one per WC, and a three point track, reconstructed from a combination of three X and three Y hits. A restriction is placed on three point tracks, where only WC2 or WC3 can be the missing WC. If information exists for all WCs in an event, only a four point track can be reconstructed. Moreover, an additional condition may be placed on the event that requires that all WCs have exactly one X hit and one Y hit.

With these possible combinations of track reconstruction methods and restraints, two configurations have been chosen for analyses. First, a "Picky Tracks" sample which only allows four point tracks and requires only one XY hit per WC. This provides the purest sample of events at the cost of statistics. Second, a "High Yield" sample which allows four point tracks and three point tracks, as well as allowing for any WC to have more than 1 XY combination of hits within it. This sample provides the highest statistics out of a given set of events, at the cost of purity.

4.2.3 Four Point Track Reconstruction

For every combination of X and Y hits across all WCs, the 3-D position of each hit is calculated using the following transformation:

$$x = x_{center} + x_{wire} * \cos(\theta) \quad (4.2)$$

$$y = y_{center} + y_{wire} \quad (4.3)$$

$$z = z_{center} + x_{wire} * \sin(\theta) \quad (4.4)$$

where θ is -13° for WC1 and WC2 or -3° for WC3 and WC4, to account for the rotation of the WCs around the Y axis. The "center" variable corresponds to the 3-D position of the body center

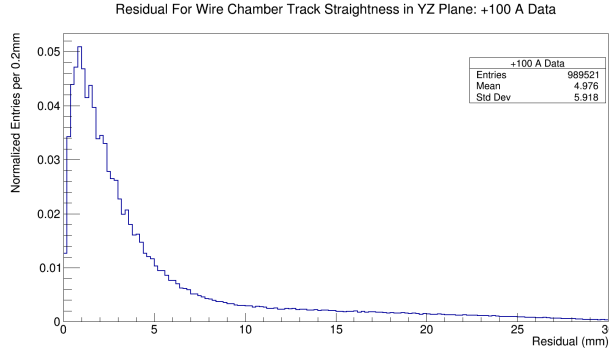


Figure 4.5: Using equation 4.5, the average distance of hits from the relative line of best fit. The plot is area normalized. Tracks with an average distance greater than 12 mm are rejected.

of a given WC, as measured by survey, given in mm. As the wires are spaced at 1 mm intervals, and wire number 0 is at the center of the WC, the wire number provides the distance from the center of the hit.

Although a particle is expected to bend in the X direction as it passes through the magnetic field, there should be no force acting in the Y direction. Therefore, if the particle is traced in the YZ plane, it should maintain a straight trajectory, excluding any interactions. Because of this, for each permutation of hits across the WCs, the combination that is used to create a WC Track is the group of hits, one XY combination per WC, that form the straightest track in the YZ plane. This is done by linear regression using the position of the hits in the YZ plane and selecting the combination that lie closest to the line of their respective linear fit. In other words, the combination of points that minimizes the average distance of each hit, or "residual", from the line of best fit, given by slope m_f and intercept y_f :

$$R = \frac{\sum_{i=1}^{NHits} |m_f z_i + y_f - y_i|}{NHits} \quad (4.5)$$

A cut of 12 mm is applied to remove events where there is no reasonable set of points that form a line. Figure 4.5 shows the residual for the +100 A data set for the straightest track in the event. Figure 6.9 overlays this plot with the respective plot from simulation. Though the underlying distributions have some disagreement, a cut at 12 mm is in the tail of both distributions, where the differences are negligible.

With a combination of hits selected to create the WC Track, the momentum for the track is calculated. Using the X and Z position of the hits in WC1 and WC2, a line is drawn in the XZ

plane, and the angle of that line with respect to the Z axis is calculated, θ_{US} . The same is done for the X and Z hits in WC3 and WC4, with angle θ_{DS} .

The beamline has two magnets, rotated at -10.5° and -5.5° around the Y axis, with different responses curves, $B(I)$, as well as fringe fields. Each magnet is expected to bend a particle by 5° . Once the particle is at the center of the magnetic field, it should have bent 2.5° from the entering trajectory. Therefore, at the center of the magnet, the bending trajectory should be normal with the aperture of the magnet.

For the WC track reconstruction, some approximations are made. A square field approximation is implemented for each magnet, where instead of fringe fields, a tophat function is used:

$$B_y(z) = B_{eff}(I), |z| < \frac{L_{eff}}{2} \quad (4.6)$$

$$B_y(z) = 0, otherwise \quad (4.7)$$

$$(4.8)$$

$B_{eff}(I)$ was calculated by using two hall probes to measure $B_{max}(I)$ of a magnet at various current settings, calculating $\frac{B}{I}$ with each probe, averaging the values, then making a polynomial fit through those points; this curve is plotted in figure 4.6. The value L_{eff} is informed from simulation such that $\int B_y(l)dl = B_{eff}L_{eff}$. According to simulation, the effective length of one of the magnets is 57.185 cm. To simplify two magnets into one, L_{eff} is chosen to be twice the effective length of a single magnet, 114.37 cm.

With these approximations, the nominal trajectory of a particle in the magnetic field is an arc of a circle, and simplifies the momentum calculation. Using B_{eff} , L_{eff} , θ_{US} and θ_{DS} , the z-component of the momentum of a WC Track is calculated to be:

$$P_z = \frac{B_{eff}L_{eff}}{3.3(\sin(\theta_{DS}) - \sin(\theta_{US}))} \quad (4.9)$$

where 3.3 C^{-1} converts from T*m to $\frac{MeV}{c}$. Using this formula, P_z for the positive polarity four point "High Yield" sample is shown in figure 4.7. The other components of the momentum, P_x and

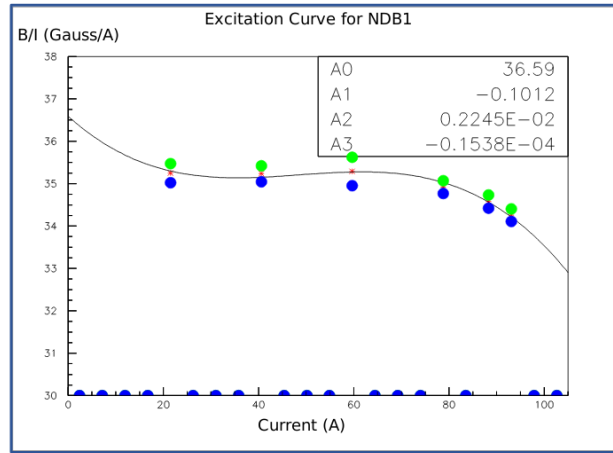


Figure 4.6: Excitation curve of NDB1 using two hall probes (green and blue), with the average in red, fitted with a third degree polynomial (black curve) with fit parameters in legend.

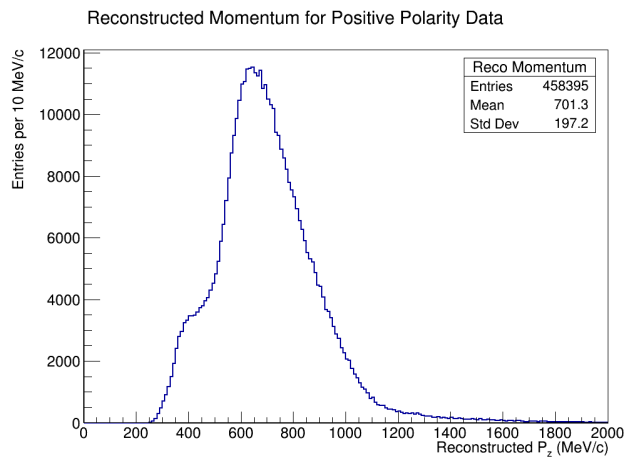


Figure 4.7: Reconstructed momentum for four point high yield tracks. The double peak structure is from the combination of 60 A and 100 A data.

1317 P_y , are found using the trajectory through WC3 and WC4:

$$(dx, dz) = (x^{WC4} - x^{WC3}, z^{WC4} - z^{WC3}) \quad (4.10)$$

$$\frac{dx}{dz} = \frac{P_x}{P_z} \quad (4.11)$$

$$P_x = \frac{P_z dx}{dz} \quad (4.12)$$

$$(4.13)$$

1318 with a similar expression for P_y .

1319 4.2.4 Quality Cuts on 4 Point Tracks: Aperture Cuts and Track Extrapolations

1320 Once a track has been reconstructed, other quality cuts are applied. Particles that scatter off of
 1321 material in the beamline will create unreasonable trajectories in the wire chambers. An example
 1322 for a particle scattering off of the downstream collimator is shown in figure 4.8. Similar cases can
 1323 occur in either of the bending magnets. To remove these cases, tracks are discarded if:

- 1324 • Projection of line of track through WC1 and WC2 forward to the magnets does not intersect the
 1325 area of the apertures of the upstream magnet.
- 1326 • Projection of line of track through WC3 and WC4 back to the magnets does not intersect the
 1327 area of the apertures of the downstream magnet.
- 1328 • Line of the track through WC3 and WC4 does not pass through both apertures of the downstream
 1329 collimator, which exists between WC3 and WC4.

1330 The next check involves extrapolating tracks through the region between the magnets. If the
 1331 approximation is made that both magnets have an identical magnetic field, then a mirror-symmetry
 1332 exists in the XZ plane, with the line of symmetry centered between the two magnets. Therefore, the
 1333 trajectory from WC1 and WC2 projected downstream should intersect the trajectory from WC3
 1334 and WC4 projected upstream, and that intersection will be at this line of reflection. As this line
 1335 extends infinitely in the Y direction, it is actually a plane, and because it is between the magnets,
 1336 the term "midplane" is used, depicted in figure 4.9.

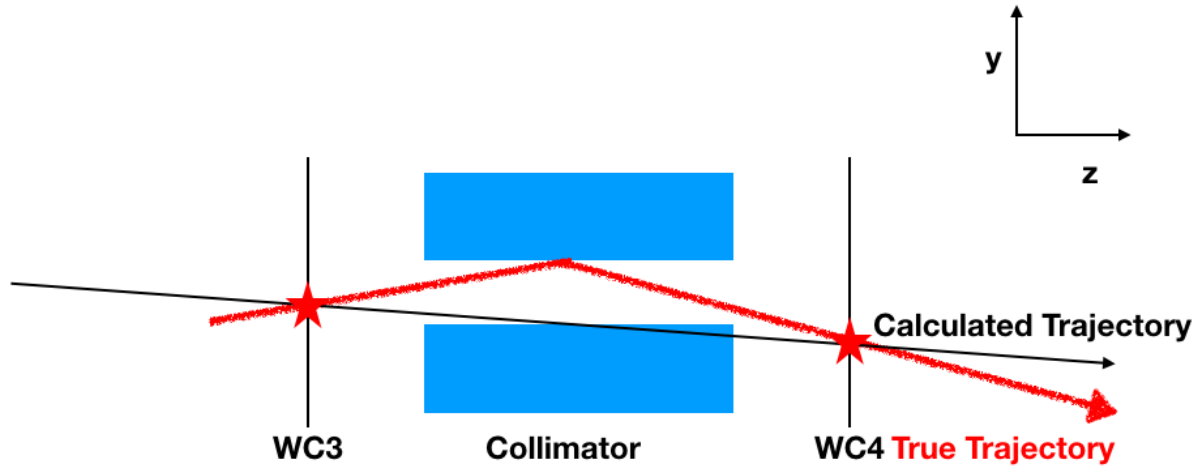


Figure 4.8: Scattering of particle off of collimator (red) and reconstructed part of track passing through collimator steel (black).

Figure 4.10 shows the ΔX , ΔY and distance plots for the +100 A four point high yield WC tracks. There is a systematic offset in data plot of ΔX of approximately 3 mm, which also occurs in the +60 A data set. This could be due to misalignment of one or more wire chambers in the beamline, and need only be a few mm to cause this offset at the midplane. A cut is place in both ΔX and ΔY requiring tracks to be within 15 mm of the mean of the respective distribution, removing the tails of the distribution which would suggest a poorly reconstructed track.

4.2.5 Three Point Track Reconstruction

In the case that a wire chamber did not register a hit from a through-going particle, either because of detector inefficiency or because the particle trajectory through the beamline did not include passing through a wire chamber, information will not be available for all four wire chambers. However a track can still be reconstructed if data exists for three WCs.

The method for a three point track begins similarly to the four point version, finding the best combination of three points that lie closest to their line of best fit (Eq. 4.5) However, to calculate the momentum, a fourth point is required. For a three point track, either the upstream (WC1 and

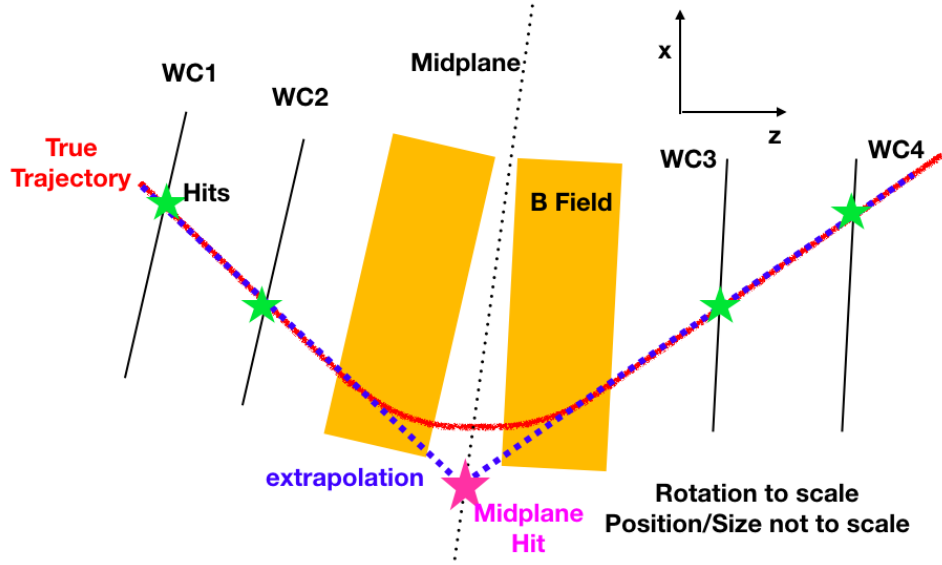


Figure 4.9: Ideal depiction of midplane, assuming identical magnetic fields. In reality, there will be some small offset due to magnet irregularities.

WC2) or downstream (WC3 and WC4) portion of the track will be complete. For the complete portion, the trajectory is extrapolated to the midplane. The point of intersection with the midplane becomes the fourth point in the track, and is used with the lone WC in the incomplete portion to complete the track. Figure 4.11 illustrates this for the case of WC3-missed events. This allows the momentum to be calculated in the same way as the four point case. Because this extrapolation would introduce larger errors the further away the line is projected, events are rejected if WC1 or WC4 is the missing wire chamber; the only allowable three point tracks are ones that miss WC2 or WC3. With the momentum, the expected position in the missed WC can be found by rearranging the momentum equation to solve for the position of the missing hit.

4.2.6 Three Point Calibration

Inherent in the three point track reconstruction was the assumption that the magnetic fields in both magnets are identical in shape and magnitude, which is not the case (figure 3.4). Therefore, a correction to the momentum calculated with the three point method is necessary. This calibration

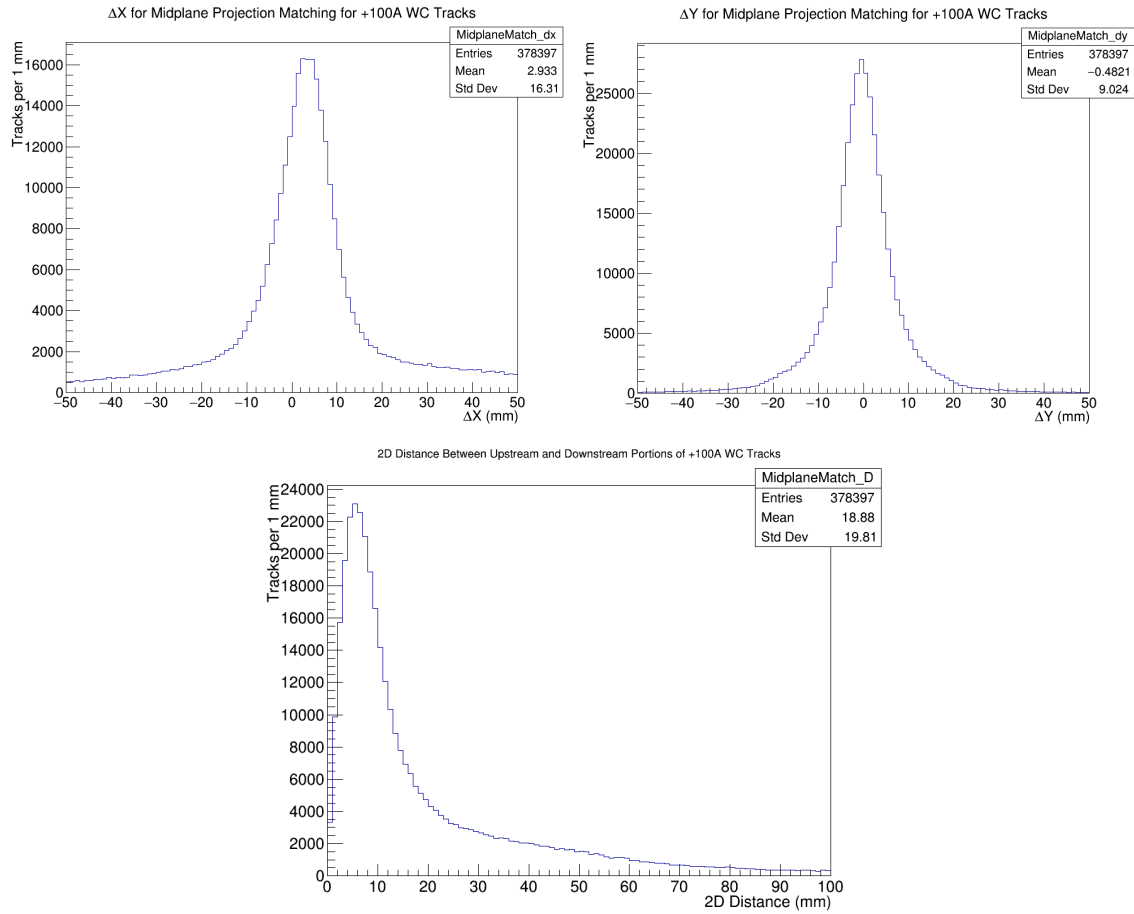


Figure 4.10: ΔX (top left) and ΔY (top right) for +100 A four point high yield tracks from projections of upstream and downstream portions of the WC track. Using those distributions, the total distance between the two projections (below). Suitable tracks must be within 15 mm of the respective mean of the ΔX and ΔY plot.

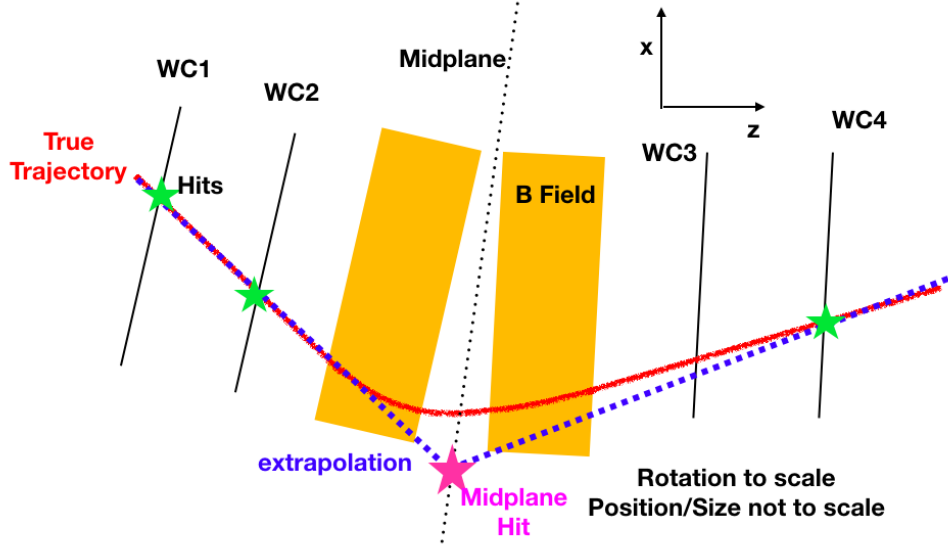


Figure 4.11: Depiction of midplane method for track missing WC3. True trajectory (red) disagrees with extrapolation at WC3 from midplane and WC4 (blue) due to magnet asymmetries.

was done by taking the Picky Tracks reconstruction for the positive polarity data sample, separated into the two magnet current settings used for this analysis, 60 A and 100 A. For each track, the information is blinded off in either WC2 or WC3, the momentum calculated using the three point method, then compared to the momentum with all four points.

From these plots, it is evident that the three-point method introduces a shift depending on the WC that is missed. Missing WC2 leads to a momentum that is higher than expected, whereas missing WC3 returns a momentum that is lower than expected. Tracks that miss WC3 assume the bending angle in the downstream magnet is the same as the bending angle in the upstream magnet. However, because the upstream magnet, NDB1, has a stronger magnetic field than the downstream magnet, NDB2, the three point method will assume an over-bending of trajectory in NDB2 (figure 3.4). A particle bending more in the magnets is associated with a lower momentum, explaining the shift seen for tracks that miss WC3. Tracks that miss WC2 have a similar explanation, with an assumption of an under-bending in NDB1, leading to an over-estimation of the momentum. The fractional error, $\frac{P_z^{3Pt} - P_z^{4Pt}}{P_z^{4Pt}}$, as a function of P_z^{3pt} is shown in figure 4.14 for the WC2-blinded 60A sample.

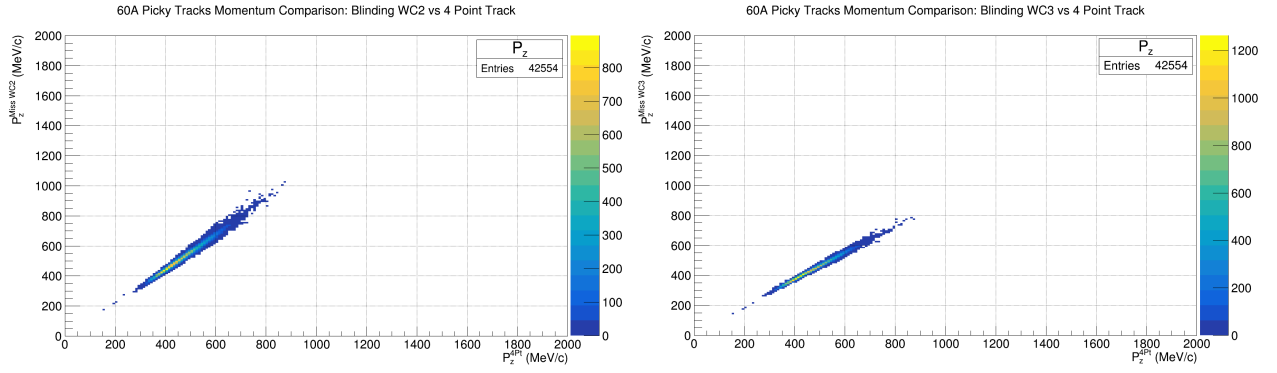


Figure 4.12: 60A Positive polarity sample: Comparison of momentum for WC2-missed tracks vs 4-point momentum (left), and WC3-missed tracks vs 4-point momentum (right).

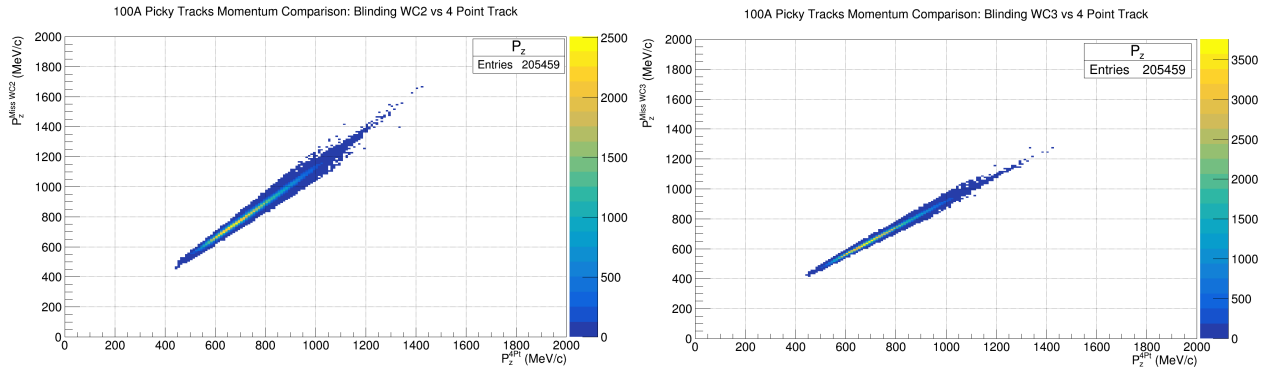


Figure 4.13: 100A Positive polarity sample: Comparison of momentum for WC2-missed tracks vs 4-point momentum (left), and WC3-missed tracks vs 4-point momentum (right).

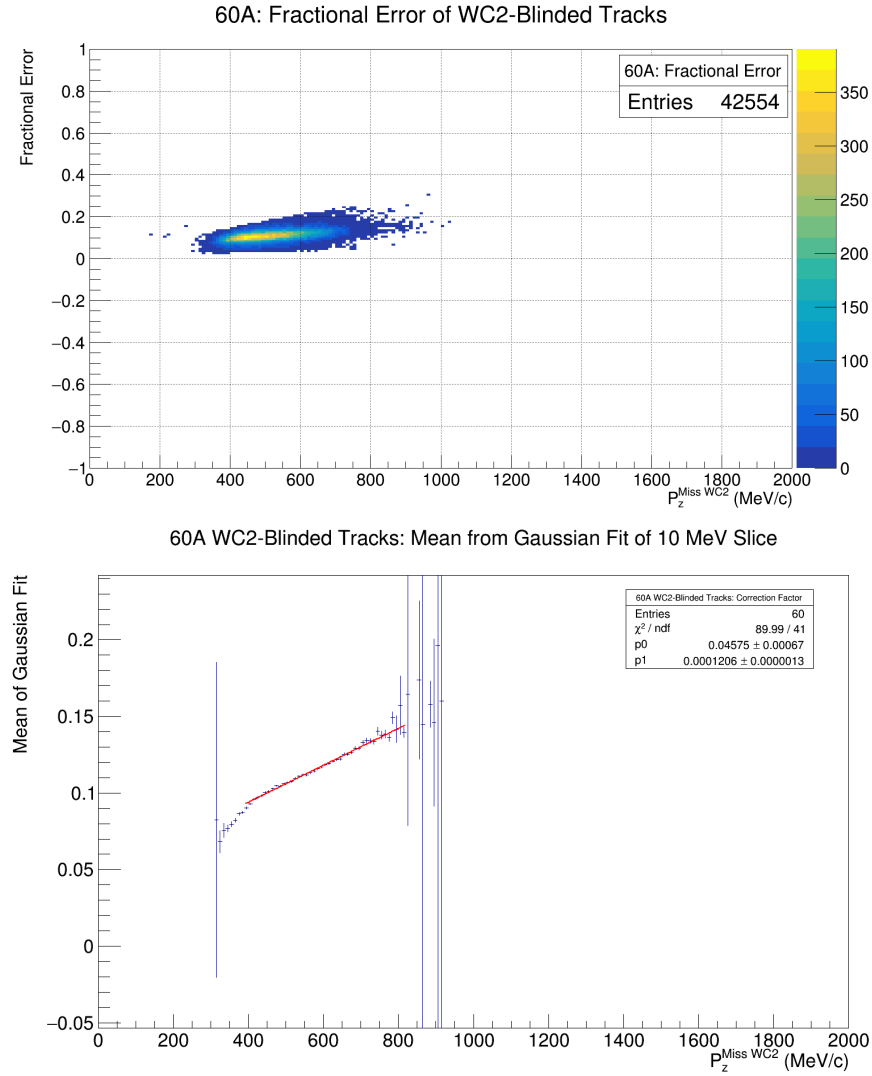


Figure 4.14: Fractional Error of WC2-Blinded 60 A tracks (Left). Mean from fits of fractional error for 60 A WC2-blinded sample (Right). Only bins between 400-700 MeV/c are used for the correction factor equation.

Current/WCMissed	3 Point Momentum Range Used for Fit (MeV/c)	Scaling Factor Equation
60 Miss WC2	400-700	$1.21\text{E-}4 * P^{3pt} + 0.0458$
60 Miss WC3	320-560	$-5.71\text{E-}5 * P^{3pt} - 0.0483$
100 Miss WC2	620-1130	$7.39\text{E-}5 * P^{3pt} + 0.0479$
100 Miss WC3	480-930	$-4.20\text{E-}5 * P^{3pt} - 0.0444$

Table 4.1: Parameters for Three Point Track Calibration

As this error is not uniform across the momentum range, a momentum-dependent calibration is needed. Each fractional error plot is sliced into 10 $\frac{\text{MeV}}{c}$ bins of P_z^{3Pt} . For each bin, a gaussian fit is applied to the fractional error for tracks within that bin. From the plot of mean from fit vs P_z^{3Pt} , a linear fit is applied in the high stats bins. Therefore, the following set of equations define the scaling from three to four point tracks, for a WC2-missed track for 60A.

$$\text{ScalingFactor} = 0.000121P_z^{3pt} + 0.0458 \quad (4.14)$$

$$P_z^{4pt} = \frac{P_z^{3pt}}{1 + \text{ScalingFactor}} \quad (4.15)$$

The parameters used for each current setting and WC-missed is given in table 4.1. Using these functions, the uncertainty associated with scaling a three point track to a four point track can be found by plotting the scaled momentum versus the original momentum. From the distribution in figure 4.15, this uncertainty is 2%.

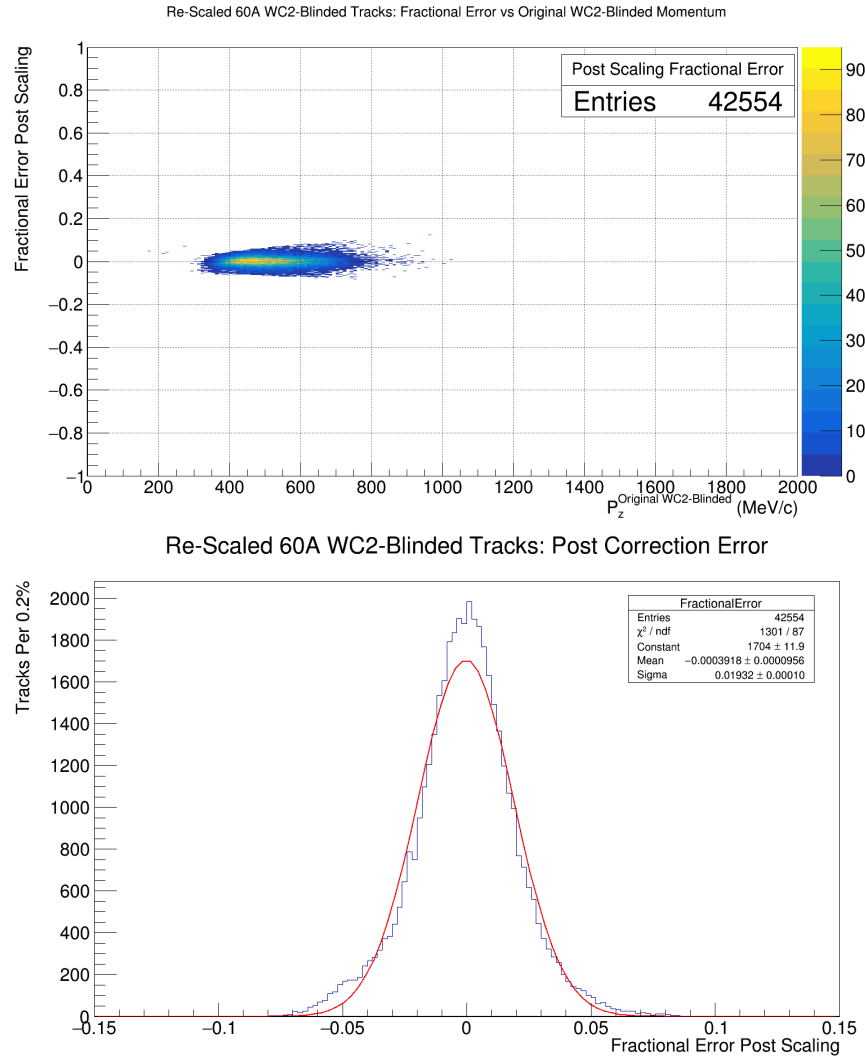


Figure 4.15: Fractional error of corrected WC2-blinded 60A tracks vs original three point momentum (Left) with Y axis projection fitted with gaussian (right).

Chapter 5

Pion Event Selection

During Run II, LArIAT recorded approximately 3.2 million events. However, any analysis-worthy event must have certain reconstructable objects associated to it: a Time of Flight (TOF), a Wire Chamber Track (WC Track), and a TPC track. Moreover, quality cuts are applied to reject events that are non-physical or are too messy to be cleanly reconstructed. In this section, the cut flow to determine the π^+ cross section sample, using these objects, is discussed.

5.1 Charge Selection, and TOF/WCTrack Existence

LArIAT operated in both a negative and positive polarity mode, selected by the flow of current in the bending magnets. The first cut on data for this analysis is to select positively charged particles, by requiring the magnets to be in positive polarity mode for that event.

The existence of exactly one TOF and WC Track for the event is required for any event to be used for analysis. As discussed in section 4.2, a Picky Track or High Yield Track requirement can be used. To have a high statistics sample, the Four Point High Yield track condition is used for this analysis. Of the initial 3.2 million events, 460,000 are in positive polarity mode, with a magnet current of 60 A or 100 A, and have a reconstructed TOF and four point HY WCTrack. Though three point tracks are reconstructable, due to difficulties in understanding the beamline simulation, three point tracks are not used for this analysis. More explanation of this is given in section 6.4.2.

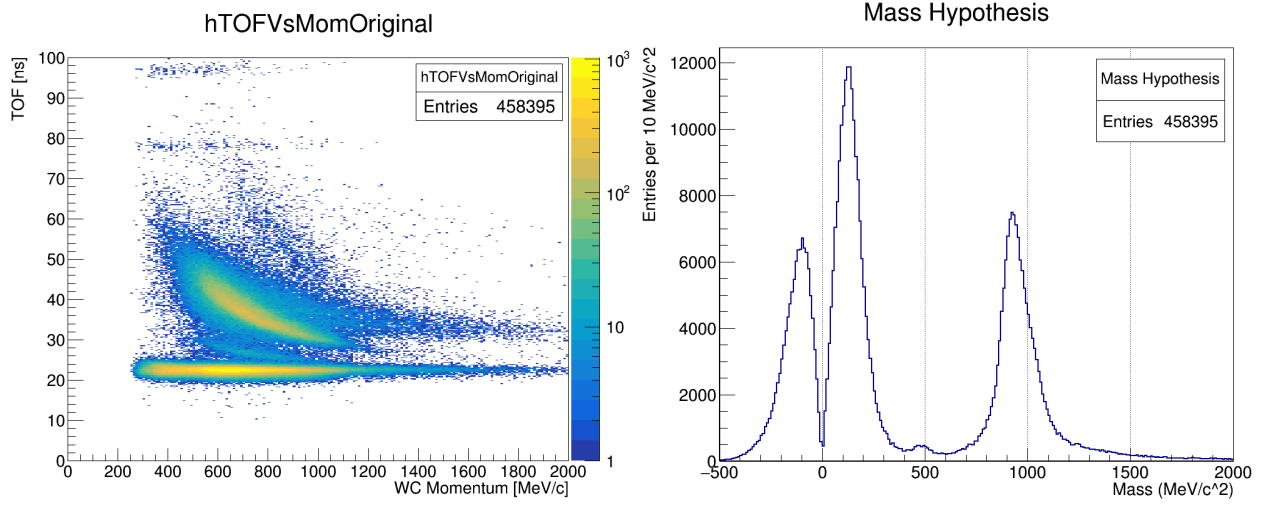


Figure 5.1: Left: Time of Flight vs WC Momentum. Right: Associated mass hypothesis using TOF and WC Momentum.

5.2 Mass Hypothesis

Using the TOF and WC Track momentum, a mass hypothesis for the event can be made. For a given momentum, p , time of flight, t , and distance of travel, $l=6.652$ m, the mass of a particle is given by the following equation:

$$m = \frac{p}{c} \sqrt{\left(\frac{ct}{l}\right)^2 - 1} \quad (5.1)$$

For the four point HY WCTrack sample, the TOF vs momentum distribution and subsequent mass hypothesis is shown in figure 5.1.

In the mass plot there are 3 peaks: a proton peak, a kaon peak, and a combined peak for pions, muons and positrons. The lighter particles are not distinguishable at this stage due to the 1 ns timing resolution of the TOF system. Moreover, because the lighter particles are moving close to the speed of light, the timing resolution of the TOF system can cause an event to reconstruct a TOF that suggests a superluminal particle, which would correspond to an imaginary mass in eq. 5.1; these events are given a negative mass in figure 5.1. A cut is placed to keep all events with $|m| < 350 \frac{\text{MeV}}{c^2}$ to filter this sample to select lower mass particles. About 289,500 events remain.

5.3 Wire Chamber Quality Cuts

With a WCTrack reconstructed for the event, quality cuts are applied to remove tracks that suggest a scattering in the beamline. These cuts are described in 4.2.4, and summarized below.

- Projection of line of track through WC1 and WC2 downstream to the magnets intersects the area of the upstream aperture of the upstream magnet.
- Projection of line of track through WC3 and WC4 upstream to the magnets intersects the area of the downstream aperture of the downstream magnet.
- Line of the track through WC3 and WC4 intersects both apertures of the downstream collimator, which exists between WC3 and WC4.
- Comparing the projection of WC1 and WC2 at the midplane with the projection from WC3 and WC4, the ΔX between the two must be within $[-12, 18]$ mm, and ΔY must be within $[-15, 15]$ mm (figure 4.10).

Figure 5.2 shows the ΔY vs ΔX for events passing the WC Quality cuts. Applying these cuts reduces the number of events to 169,700. The WC information for the events that survive this cut are also used as input for the simulation in chapter 6.

5.4 TPC Quality Cuts

At this stage, reconstructed TPC information is used to find quality events for analysis. To eliminate any events that only have tracks from cosmic muons, events are required to have at least one TPC track starting within 4 cm of the upstream face of the TPC. Figure 5.3 shows, per event, the number of tracks found in the upstream 4 cm of the TPC.

As it is possible for many particles to traverse the beamline within a TPC readout window, some TPC events can have too much activity for reconstruction to be trustworthy. To remove these “pileup” events, a cut is applied to remove events with more than 4 tracks reconstructed within 14 cm of the upstream face of the TPC. Figure 5.4 plots, per event, the number of tracks found in the upstream 14 cm of the TPC. In combination, these cuts reduce the number of events to 121,700.

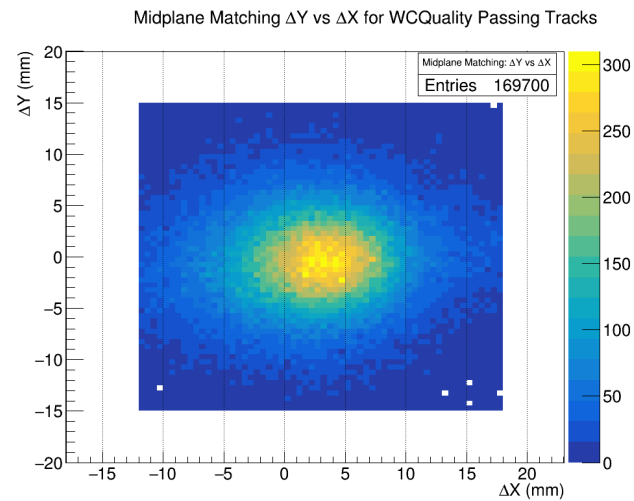


Figure 5.2: Using the cuts described in the bullet points, the ΔY vs ΔX for tracks that pass the WC Quality filter.

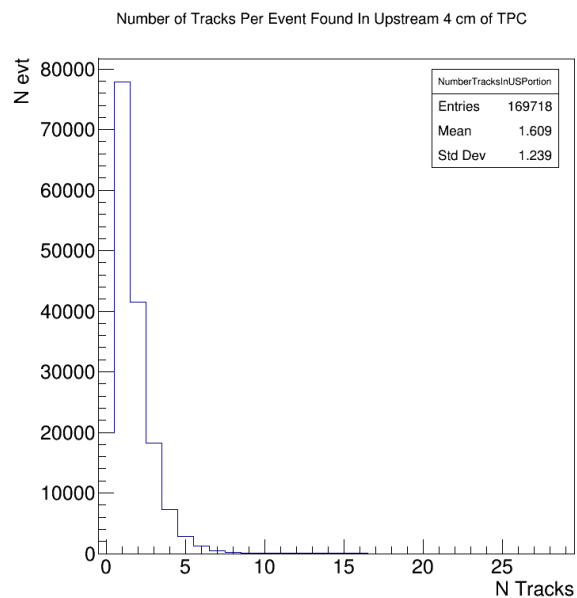


Figure 5.3: Per event, the number of tracks with a reconstructed point within the upstream 4 cm of the TPC.

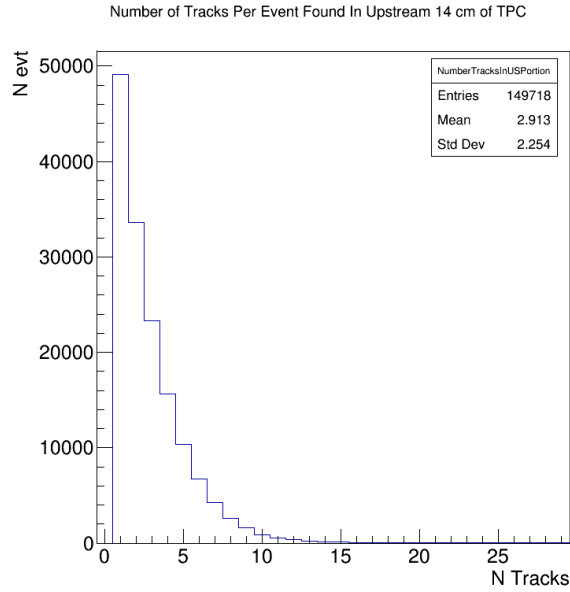


Figure 5.4: Per event, the number of tracks with a reconstructed point within the upstream 14 cm of the TPC. Tracks with more than 4 tracks are removed from the sample.

5.5 WC To TPC Match

In the previous cuts, beamline and TPC information were disconnected; neither relied on the other to decide whether the event passed that stage of cuts. The next cut makes this connection by matching the WCTrack in the event to, at most, one of the reconstructed TPC tracks for the event. The TPC tracks that are considered for a possible match to the WCTrack meet the following conditions:

- The TPC track must have an initial start position within $Z=2$ cm to $Z=6$ cm into the TPC.
- The Z-projection of the TPC track must be at least 4 cm long. Namely: $Z_{end} - Z_{begin} > 4$ cm.

For tracks that meet these conditions, a line through the hits of the track from WC3 and WC4 is projected into the TPC to the Z position of the start of the TPC track. Comparing the XY coordinates of this projection to the position of the TPC track, the differences, ΔX and ΔY are calculated. A circular cut is applied, where TPC tracks are rejected if they are outside of a circle with radius of 3.5 cm and a center of $[X_{center}, Y_{center}] = [0.35 \text{ cm}, -0.57 \text{ cm}]$. This offset is most likely

1459 due to misalignment of the beamline. In equation form:

$$(\Delta X - 0.35 \text{ cm})^2 + (\Delta Y + 0.57 \text{ cm})^2 < (3.5 \text{ cm})^2 \quad (5.2)$$

1460 If a track passes this position based cut, a second, angle-based cut is applied, where the angle
 1461 between the WCTrack projection and the TPC track is less than 0.2 radians, or approximately
 1462 11.5° . In equation form: $\alpha = \cos^{-1}(\hat{WC} \bullet \hat{TPC}) < 0.2 \text{ rad}$. If there are multiple tracks that pass
 1463 both the position and angle based cut, the event is rejected. Requiring uniqueness of the WC-TPC
 1464 match limits the possibility of matching the wrong TPC track to the WCTrack. Figure 5.6 plots
 1465 the ΔY vs ΔX and α for tracks that pass the WC to TPC Track Match. 78,500 events remain
 1466 after this cut.

1467 5.6 Shower Filter

1468 Though the beamline mass cut serves to remove most of the kaons and protons from the data set,
 1469 muons and positrons still exist as a background. To remove positrons, a shower filter is implemented.
 1470 When interacting, muons, pions, and the small contamination from kaons and protons would be
 1471 expected to leave a few long tracks in the TPC, whereas positrons entering the TPC should start
 1472 to shower, leaving many short tracks. To filter out these positron events, a cone-shaped region of
 1473 interest (ROI) is created around the WC-TPC matched track, and within that region, the number
 1474 of short tracks are counted. If too many short tracks are found in the ROI, the event is rejected.

1475 5.6.1 Cone Dimensions and Orientation

1476 The cone is oriented such that the initial trajectory of the WC-TPC matched track forms the
 1477 axis of the cone. The dimensions of the cone should be large enough such that, in the case of an
 1478 positron event, most of the shower activity is contained. However, if the cone is too large, other
 1479 reconstructed tracks not associated to the candidate WC-TPC matched track could be included;
 1480 though a pileup filter has been implemented (section 5.4), there may still be other tracks in the
 1481 TPC that the shower filter should ignore. Given most tracks begin a few cm into the TPC, an
 1482 positron could start showering within this dead region of argon. Therefore, the cone should not
 1483 start at a vertex, but begin with some opening radius. This collects any electromagnetic activity

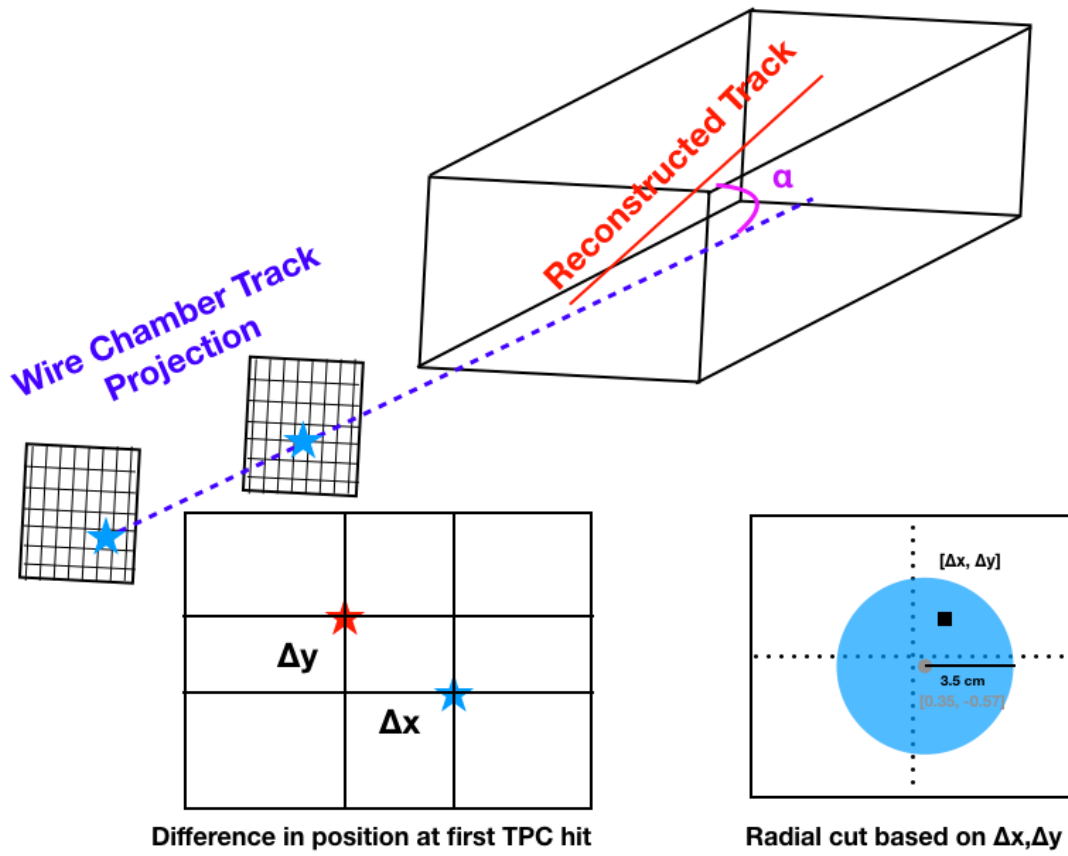


Figure 5.5: Wire Chamber to TPC Track Matching. A match requires projections to be sufficiently close at the position of the start of the TPC track and to be parallel to each other, within 0.2 rad, or 11.5° .

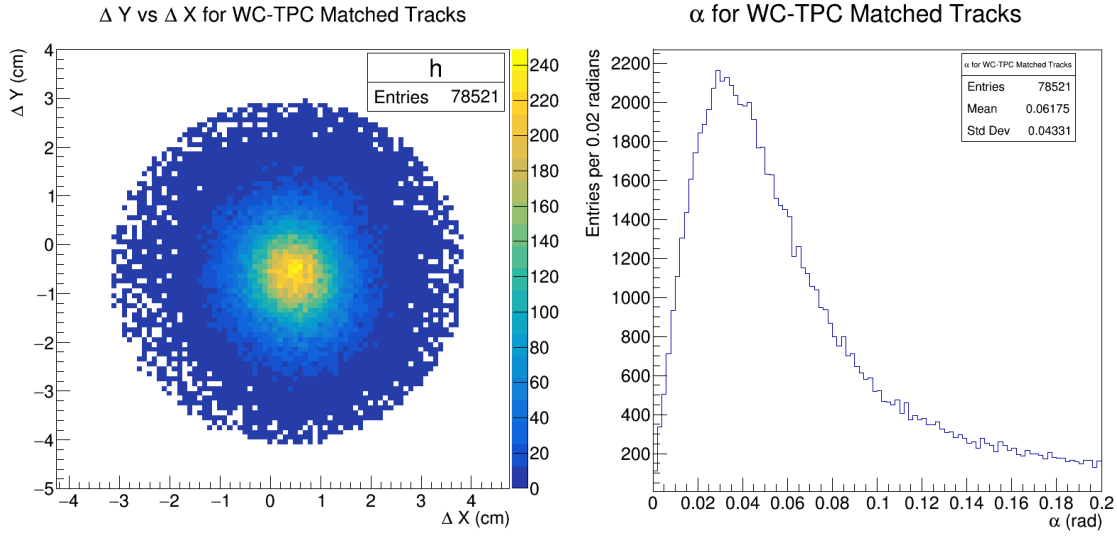


Figure 5.6: For events that have a unique match within the cut value set for the match, the ΔY vs ΔX for those matched tracks (left) and α (right).

around the WC-TPC matched positron track inside the cone. With this, the cone is defined by three parameters: the beginning radius of the cone, the length of the cone, and the ending radius of the cone.

For the WC-TPC matched track, provided no other TPC tracks are nearby, there is up to a 4 cm tolerance where the start of the matched track could shift and still have a match occur. This 4 cm tolerance is used as the beginning radius of the cone. The end radius of the cone should be defined how far, transverse to the positron trajectory, one must look to capture most shower activity. By definition, this is the Molière radius of an electron, and for liquid argon, this is approximately 10 cm. To ensure more than 95% of the shower would be contained, two Molière radii are used, for an end radius of 20 cm. The length of the cone is determined by how far an positron should travel before it starts to shower. This is the radiation length of an electron, and is about 14 cm in liquid argon. However, if the cone were only 14 cm long, the expected start of the shower would be at the boundary of the cone. Therefore, to ensure the entire cascade of the shower is captured, the length of the cone is extended to five times the radiation length, 70 cm. Other combinations of radii and length were tested in simulation, but failed to yield better disambiguation of positron and pion events. 5.7 shows a diagram of the conical region around a WC-TPC matched track that is considered for the shower filter.

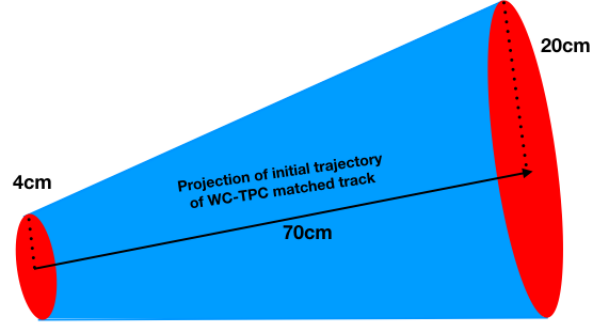


Figure 5.7: Orientation and dimensions of cone region of interest around WC-TPC matched track where short tracks are considered.

5.6.2 Tuning Shower Filter in Simulation

Using simulation of pions and positrons, the shower filter can be tuned to maximize the number of pions passing the filter while also minimizing the nubmer of positrons passing. As the filter is to reject events with too many short tracks reconstructed within the conical ROI, tuning this filter requires two parameters to be optimized: the definition of “short” and the definition of “too many”. For this study, the allowed parameter space spans $L_{short} = [0, 10] \text{ cm}$ and $N_{tracks} = [0, 20]$.

The method for generating the simulation is given in 6.1. To tune the filter, the DDMC pion and positron samples were reconstructed and filtered through the TPC quality cuts (section 5.4) and for a unique WC-TPC track match (section 5.5). Of the events that survived, 10,000 pion and positron events were used to tune the shower filter.

For a given event, the tracks within the cone are collected. For each combination of L_{short} and N_{tracks} , a boolean is returned to indicate whether the collection of tracks would pass the filter if that combination of L_{short} and N_{tracks} were used. Combining over all the events in the sample gives an expected passing rate for any combination of parameters. The passing rates for pion and positron simulation are given in figure 5.8. Excluding the most extreme cut values, pions pass the shower filter with more than 97% efficiency. Therefore, the cut focuses on admitting as few positrons as possible while maintaining this 97% efficiency for the pions. A cut is placed at $[L_{short}, N_{tracks}]$ of $[10 \text{ cm}, 3]$. Any event with more than 3 tracks shorter than 10 cm within the cone ROI is classified

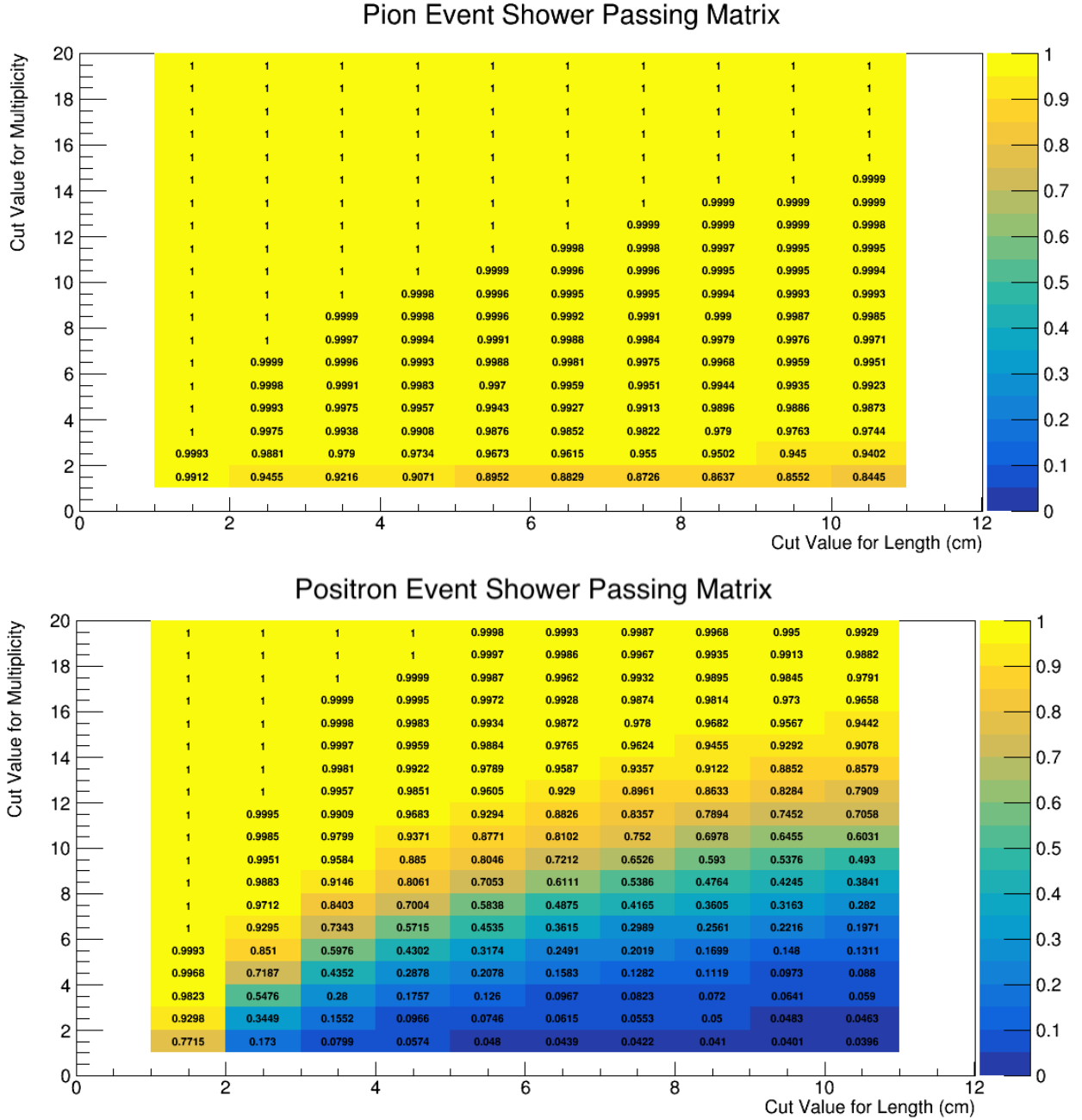


Figure 5.8: MC passing rates over parameter space of L_{short} and N_{tracks} for pions (top) and positrons (bottom). Each cell represents the passing rate at that given L_{short} and N_{tracks} . A cut placed at [3 cm, 10 tracks] admits 97.4% of pions and 5.9% of positrons.

as a positron and removed from the sample. From the plot, this admits 97.4% of pions and 5.9% of positrons. Figure 5.9 shows the shower passing rates for data as a function of L_{short} and N_{tracks} . Placing the cut at $[L_{short}, N_{tracks}]$ of [10 cm, 3] reduces the number of events to 68,600.

5.7 Proton Filter

Though there is a mass cut to remove protons from the analysis, it is still possible for some protons to contaminate the data set due to poor reconstruction of the time of flight. However, there is a way to filter out some of these protons. The last filter in the analysis uses calorimetric information to remove stopping proton events from the sample. This method can also remove pions and muons that have poor energy reconstruction. Protons are more heavily ionizing than pions and muons, and should leave a larger $\frac{dE}{dX}$ profile. Also, as particles slow down in a medium as they start to reach zero kinetic energy, the ionization increases, and this rate of increase as a particle stops is also different for protons. This increase at the end of the track is called the “Bragg peak”. Therefore, by plotting $\frac{dE}{dX}$ at a point along the track versus the distance that point is from the end of the track, called “residual range”, and doing so over all the points along the track, protons will populate differently than pions and muons. Figure 5.10 plots $\frac{dE}{dX}$ vs residual range for a sample of +100 A single particle pion and proton DDMC events, subject to the TPC based cuts described previously.

The relationship between $\frac{dE}{dX}$ and residual range can be described by an exponential function [5]. Based on measurements from ArgoNeuT, the relationship between $\frac{dE}{dX}$ and residual range (R), is described by the following function:

$$\frac{dE}{dX} = A * R^{-0.42} \quad (5.3)$$

This allows a way to disambiguate protons from pions. For a given track, take the points $(R, \frac{dE}{dX})$ for that track and apply this exponential fit, and return the best value for A. Protons will return a larger value of the constant, A, than pions and muons. Figure 5.11 shows the value of A for relevant particle species, using truth information from GEANT4, as well as the returned value of A from the events used to populate figure 5.10.

Some events in figure 5.11 return a PIDA value away from the expected value. There are two

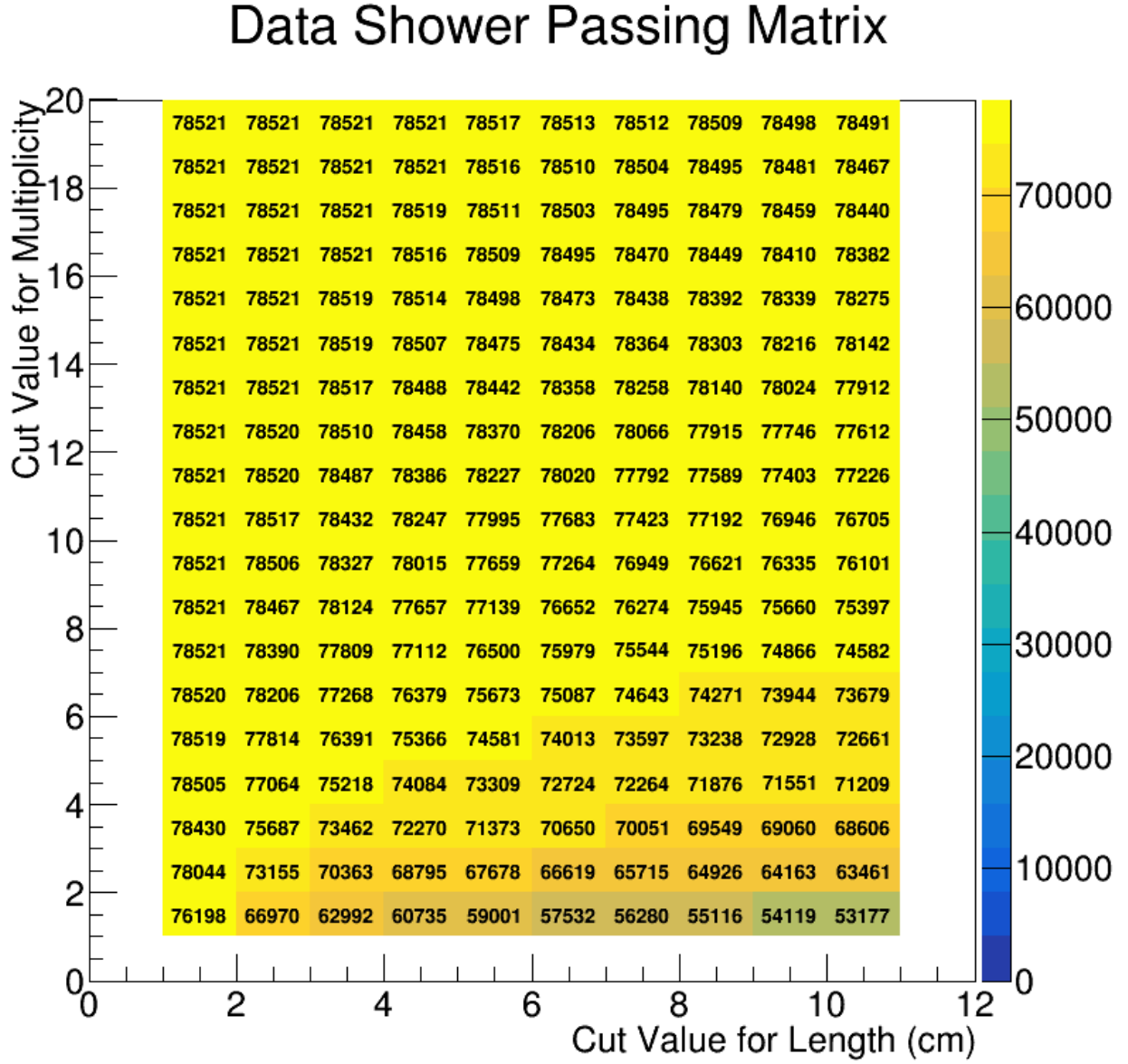


Figure 5.9: Shower filter pass rates for data over parameter space of L_{short} and N_{tracks} . Each cell represents the passing rate at that given L_{short} and N_{tracks} . A cut placed at [3 cm, 10 tracks] which admits 68,600 events.

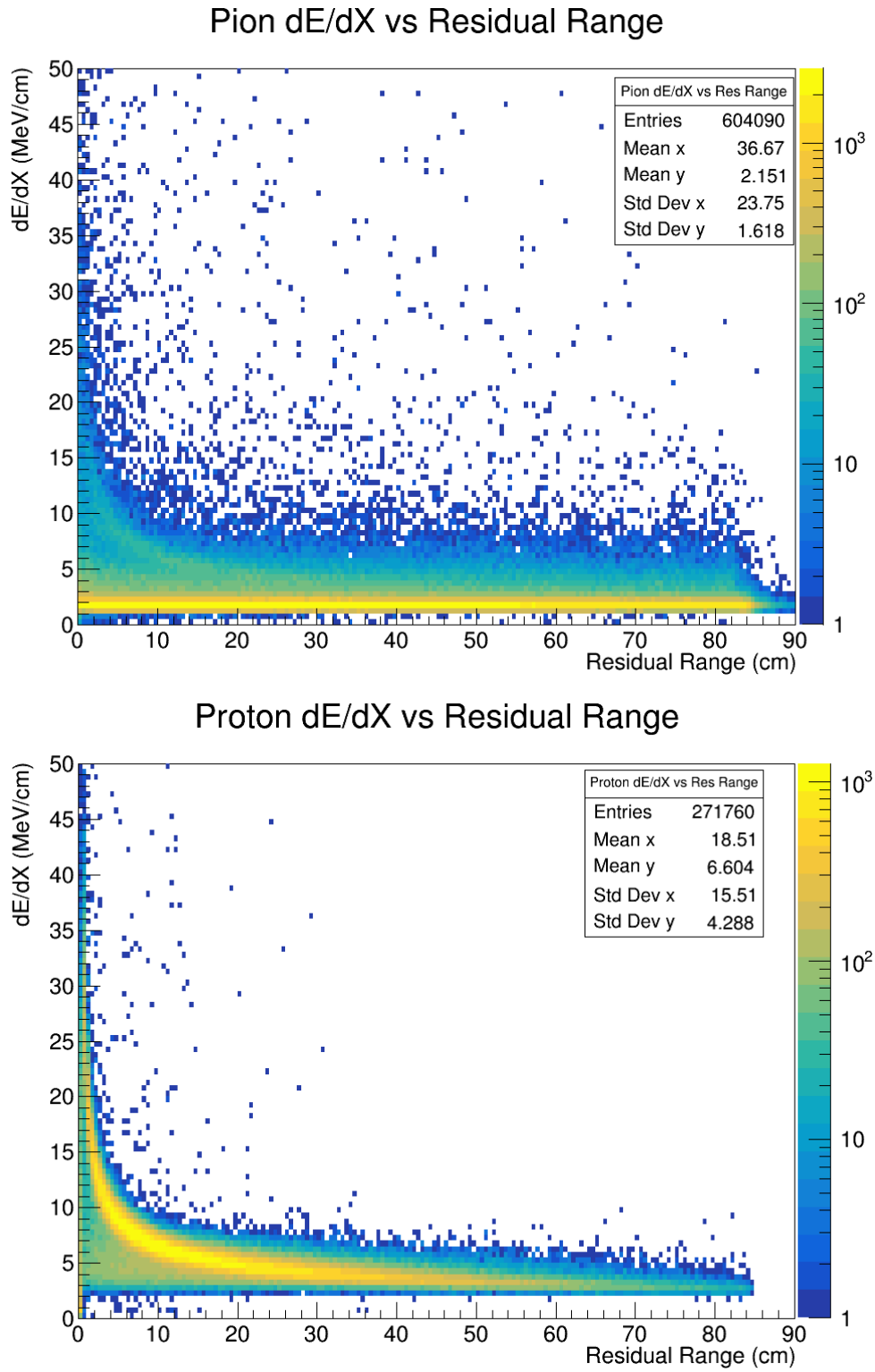


Figure 5.10: $\frac{dE}{dX}$ vs Residual Range for 5000 DDMC pion (top) and proton (bottom) events.

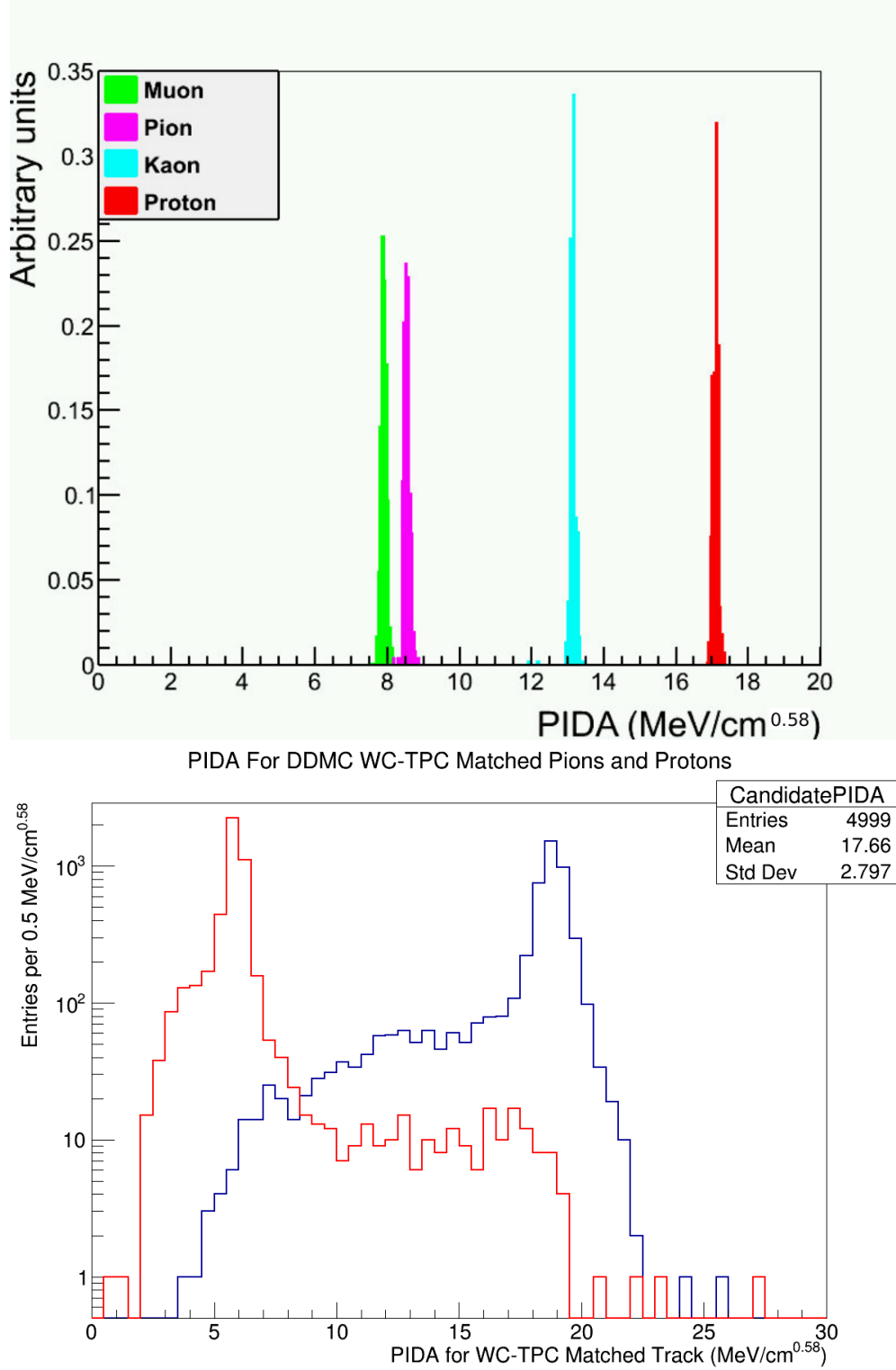


Figure 5.11: Using truth information from GEANT4, the PIDA returned from a fit of $\frac{dE}{dX} = A * R^{-0.42}$ (top). PIDA (log scale) returned for pion (red) and proton (blue) DDMC test samples (bottom).

Current Setting or Cut (Survival % Per Cut)	+60 A	+100 A	Total
WCTrack and TOF Exist	80,069	378,397	458,466
$ m < 350 \frac{MeV}{c^2}$	71,066 (88.8%)	218,444 (57.5%)	289,510 (63.1%)
WCQuality	35,877 (50.5%)	133,841 (61.3%)	169,718 (58.6%)
TPC Upstream Track Exists	30,447 (84.9%)	119,273 (89.1%)	149,720 (88.2%)
TPC Pileup Filter	25,200 (82.8%)	96,538 (80.9%)	121,738 (81.3%)
Unique WC-TPC Match	14,643 (58.1%)	63,878 (66.2%)	78,521 (64.5%)
Shower Filter	11,971 (81.8%)	56,635 (94.6%)	68,606 (87.4%)
Proton PIDA Filter	11,229 (93.8%)	53,555 (88.8%)	64,784 (94.4%)

Table 5.1: The event reduction table for +60 A and +100 A Data. 64,784 events pass all filters and are used for the cross section.

reasons for this. First, this method is to be used for stopping particles, which will show an increase
 in ionization as the particle stops. Many of these particles do not stop, and instead interact before
 the particle reaches its Bragg peak. If a particle interacts before this peak, the $\frac{dE}{dX}$ vs residual
 range plot for that track will appear flat, even at zero residual range, making a fit less useful.
 Second, if the track and energy reconstruction fails in some way, and there are points along a pion's
 track where the $\frac{dE}{dX}$ is extremely large, those poorly reconstructed points can also skew the fit.
 However, from the test proton and pion sample, even with these reconstruction inefficiencies, using
 a PIDA cut can remove protons from the sample. A cut is placed at $10 \frac{MeV}{cm^{0.58}}$, which retains 96%
 of pions and rejects 96% of protons for the +100 A samples. For the +60 A sample, 96% of pions
 survive while 99% of protons are rejected. Figure 5.12 shows the PIDA distributions for data events
 reaching this stage of the analysis. With a cut at $10 \frac{MeV}{cm^{0.58}}$, 64,784 events pass this filter and are
 the events used for the cross section analysis. Table 5.1 reviews the event reduction for both +60
 A and +100 A data sets.

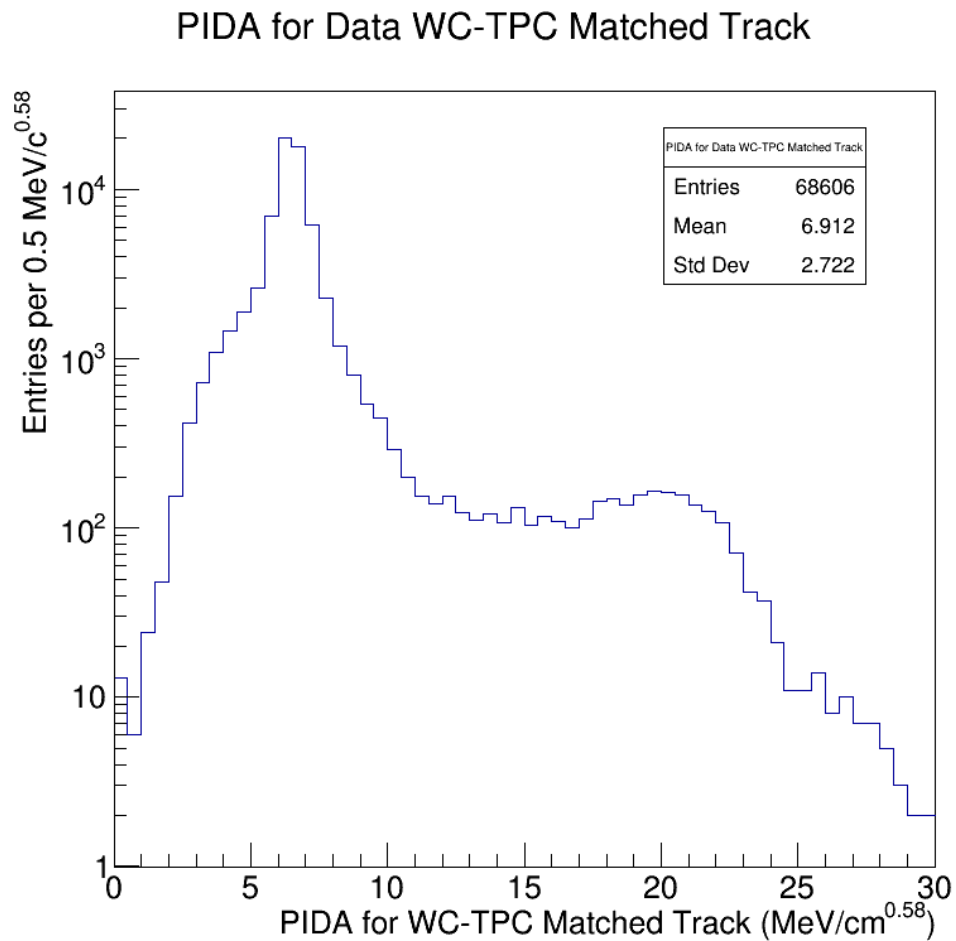


Figure 5.12: PIDA (log scale) for tracks to be considered for cross section analysis. Events are excluded with a PIDA greater than $10 \frac{\text{MeV}}{\text{cm}^{0.58}}$.

Chapter 6

Simulation

Part of any cross-section analysis is a comparison to Monte Carlo simulation. This section discusses the methods used to create a simulated beam, as well as known similarities and differences to data-taking conditions.

6.1 Data-Driven Monte Carlo

The Monte Carlo (MC) events created for this analysis uses single particle gun events, enhanced by beamline reconstruction to determine the initial kinematics of all particles in each event. The full data sample is filtered by magnet polarity, current, and WCTrack conditions. With the WCTrack and TOF information, a mass hypothesis can be made to choose protons, kaons, or a mixture of pions, muons and positrons. As explained in chapter 5, both the +60 A and +100 A, 4 point WCTrack, WC-Quality filtered $\pi/\mu/e$ samples were used for the cross section analysis.

For the +100 A $\pi/\mu/e$ data events, the distributions of the WCTrack information, including the three-momentum and XY position of the hit in WC4 are saved, and are shown in figures 6.1 and 6.2, with similar plots for the +60 A in figures 6.3 and 6.4. These distributions combine to create a five-dimensional probability distribution from which the initial kinematics of a simulated particle is chosen. The particle species is chosen by using the momentum-dependent beamline composition distributions, and is discussed in section 6.3. Information about this particle, including PDG and initial kinematics, is saved in the HEP event text file format. Though the initial XY position is

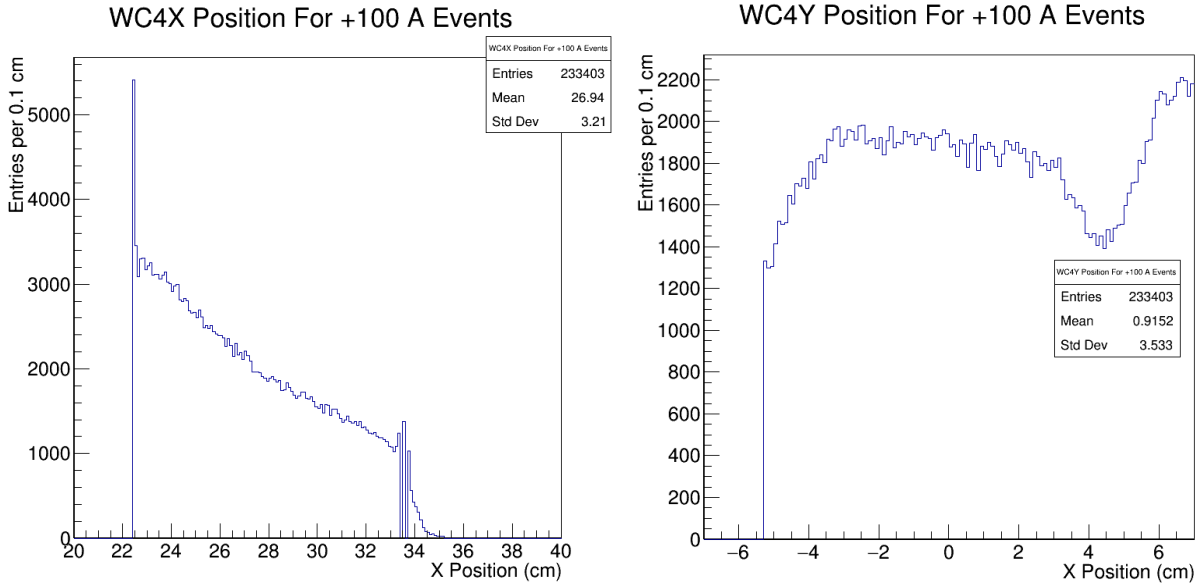


Figure 6.1: Data XY start position for +100 A events. DDMC is generated by using these plots as probability distributions.

chosen through the probability distributions, the Z coordinate is set to 100 cm upstream of the front of the TPC. Particles are then simulated through the final 100 cm of beamline into the TPC. Standard LArSoft packages, tuned for LArIAT, create data-like objects from the simulation that can then be reconstructed in the same way as data. Creating MC events in this manner ensures the MC will be similar to the data from which it pulls. This is why the term “Data-Driven Monte Carlo” (DDMC) is used to describe the simulation.

Approximately 1.1 million DDMC events were simulated for both the +60 A and +100 A samples, in two sets. Around 550,000 events create a pure proton sample and the other 550,000 constitute a mixture of pions, muons and positrons. The proton sample momentum spectrum matches the overall data set, while the pion, muon and positron sample is weighted by the beamline composition. For example, about 80% of the +100 A sample is pions, 10% are muons and 10% are positrons. The +60 A sample has a higher positron content, as suggested by the beamline composition. Moreover, as the composition is momentum dependent, the momentum spectrum of each individual particle species will match the shape of the distribution from the beamline simulation. The downside of using this method is that particles with a smaller percentage of the composition will have fewer events simulated. Unfortunately, given the limitations of memory

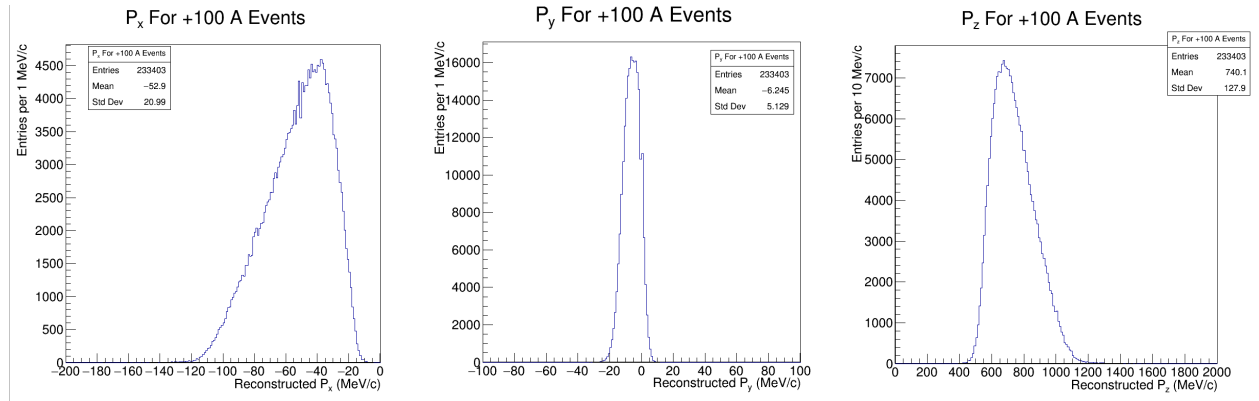


Figure 6.2: P_x , P_y , P_z used for + 100 A DDMC production. All particle species use the P_x and P_y distributions. Low mass particles use P_z distribution, but choose particle species by using momentum-dependent composition functions.

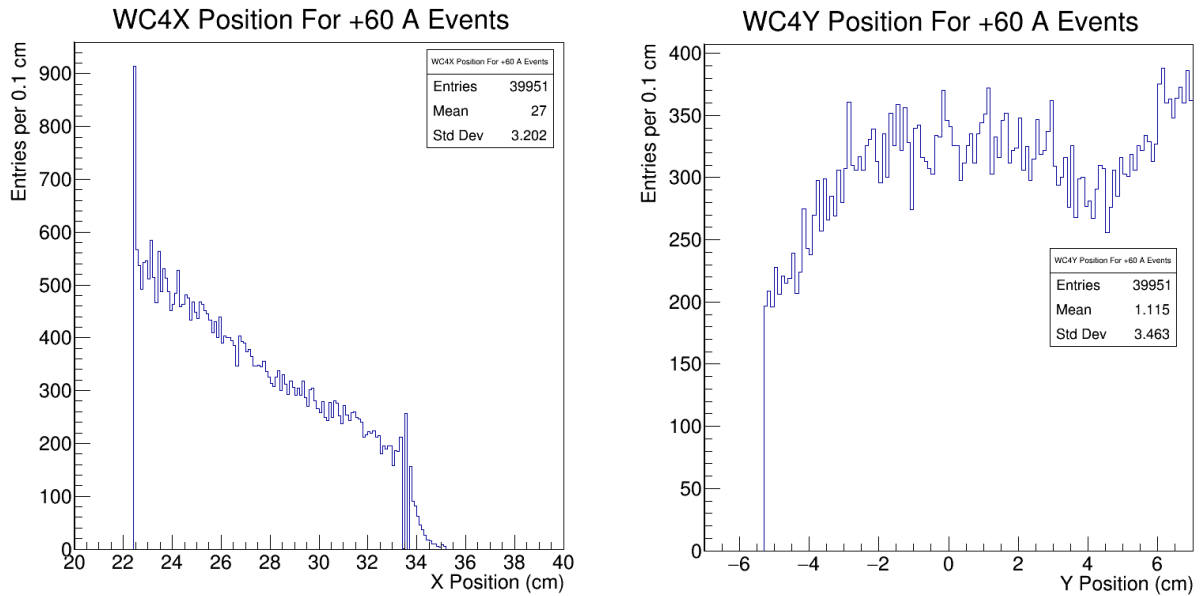


Figure 6.3: Data XY start position for +60 A events. DDMC is generated by using these plots as probability distributions.

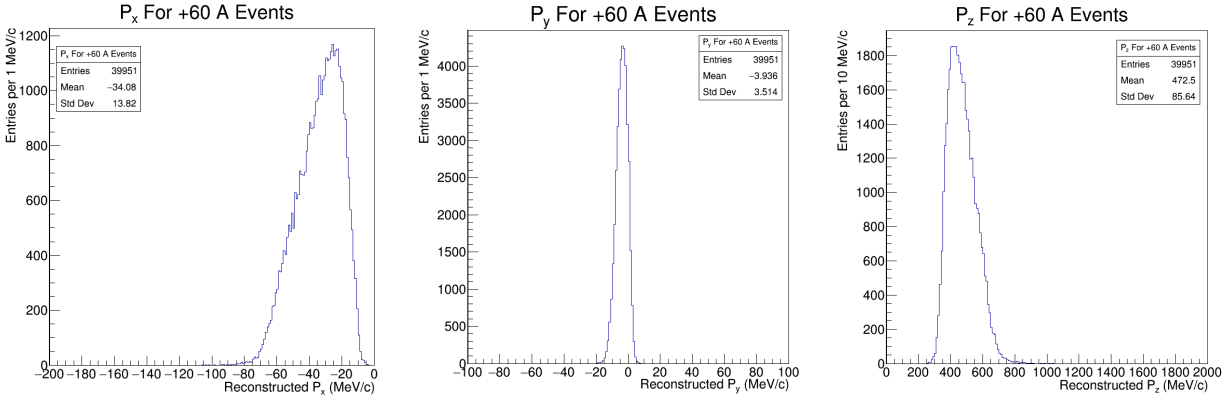


Figure 6.4: P_x , P_y , P_z used for +60 A DDMC production. All particle species use the P_x and P_y distributions. Low mass particles use P_z distribution, but choose particle species by using momentum-dependent composition functions.

storage available, a larger sample with higher statistics for the rarer particles species could not be created.

6.1.1 Simulation of Pileup

The method described previously only creates single particle events that look like particles that caused a trigger in the beamline. Secondary to these particles are other pileup tracks that enter through the front of the TPC. These particles should be filtered by any analysis, but for a more realistic MC sample, should be simulated.

By definition, a pileup track is any track that enters the front of the TPC, but is not the WC-TPC matched track for the event. Often these tracks are from highly energetic muons, created from interactions of the 120 GeV proton beam on the secondary target just upstream of the detector hall, which then penetrate through the detector hall and enter the TPC. An upgrade to the TPC simulation to include these pileup tracks is currently in development, but is not completed in time for this analysis. An explanation of how the pileup simulation will work is summarized here.

The muons created from interactions in the secondary target are assumed to have a total momentum between 32-64 GeV, with a flat probability. Using the initial trajectory of the muon track in the TPC, the angles of the track, θ_{xz} and θ_{yz} , are used to calculate the 3 components of the momentum, and the initial hit of the track provides the XYZ position. Using these variables,

the position of the muon is projected to 1 cm before the front of the TPC. It is the XYZ position here, along with the momentum of the muon, that provides the probability distributions that are drawn from to choose the initial kinematics of the pileup muon. Contrary to the primary particle simulation, the five distributions are drawn from independently, instead of as part of a 5-D probability distribution. The number of pileup muons to be simulated per event is chosen by drawing from the distribution of pileup multiplicity in the matching data sample.

6.2 Beamline Material Energy Loss

The wire chamber system can be used to calculate the kinetic energy of a particle in the beamline up to WC4. The TPC acts as a calorimeter, measuring the energy loss of a particle as it traverses the active volume. However, there is no data-based measurement of the energy loss due to ionization for the particle between WC4 and the beginning of the TPC active volume. This region includes many materials, including the DS time-of-flight paddle, a “Halo” veto paddle that was not usable, the steel of the cryostat, and the few centimeters of argon within the cryostat but is not part of the active volume of the TPC (figure 3.3). Due to this material, some amount of energy must be subtracted from the beamline measurement of the kinetic energy to be used as the initial kinetic energy in the TPC. The relationship between these energies is given by:

$$E_{TPCStart} = E_{WC4} - E_{Loss} \quad (6.1)$$

The materials present between WC4 and the active volume of the TPC are given in table 6.1.

The energy loss can be derived from simulation, and was done using the π^- DDMC simulation [18]. As pion ionization is not charge dependent, it is assumed the π^- energy loss distributions and the analysis of the distributions will be applicable to the π^+ analysis. For each DDMC π^- , the true energy loss between WC4 and the TPC active volume is calculated, and is shown in figure 6.5 for both the -60 A and -100 A simulated samples. From these plots, it is evident that a double peak structure exists. The cause for this is the halo paddle between WC4 and the downstream TOF paddle, visualized in figure 6.6. Pions that pass through the air in the hole in the paddle lose less energy than pions that pass through the scintillator of the paddle.

Whether a pion hits the paddle or not is a function of the initial position and momentum of

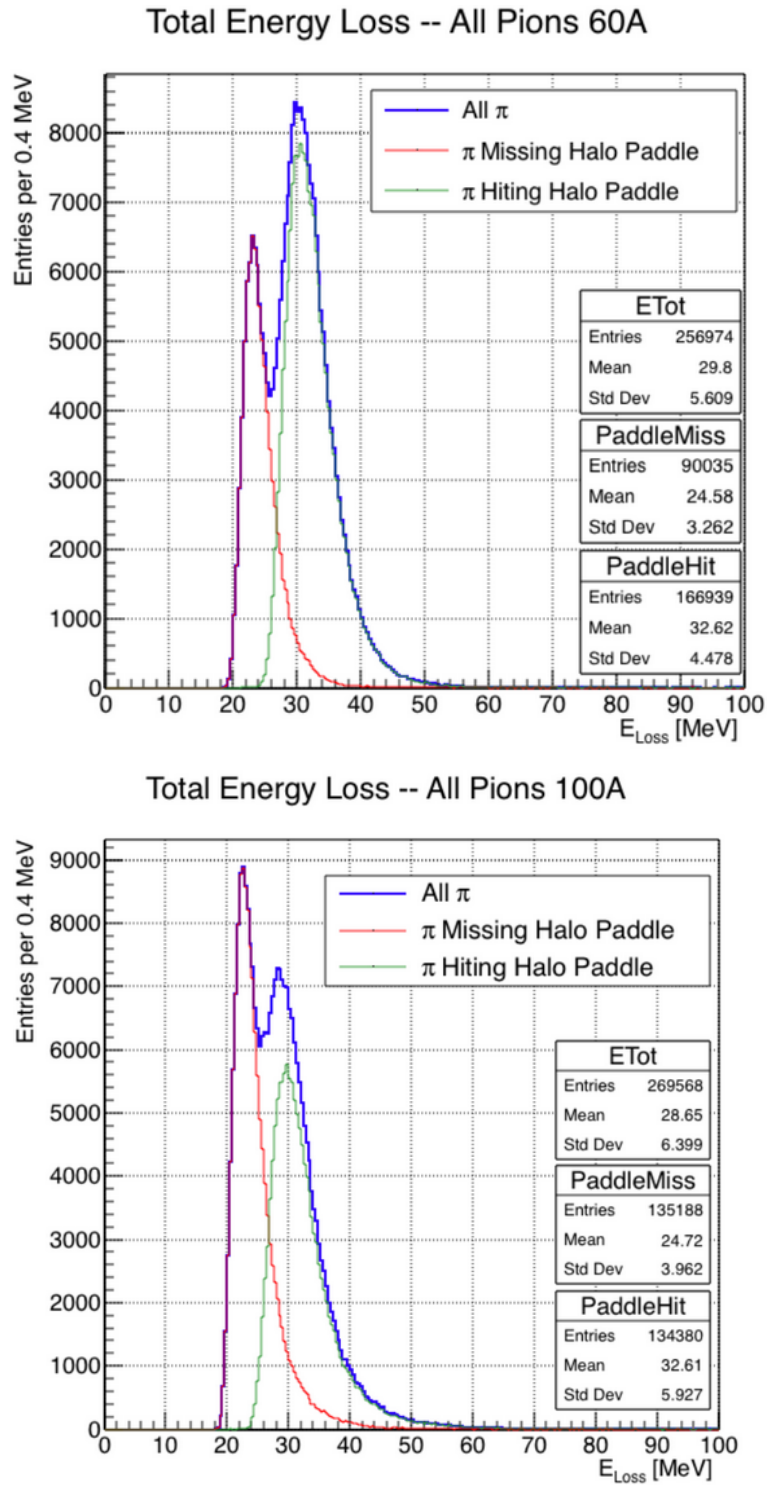


Figure 6.5: For 60 A pions (top) and 100 A pions (bottom), the total energy loss between WC4 and the active volume of the TPC. The double peaked structure is due to particles hitting the plastic of the Halo paddle or going through the hole in the center of it. Plastic hitting particles have a higher energy loss.

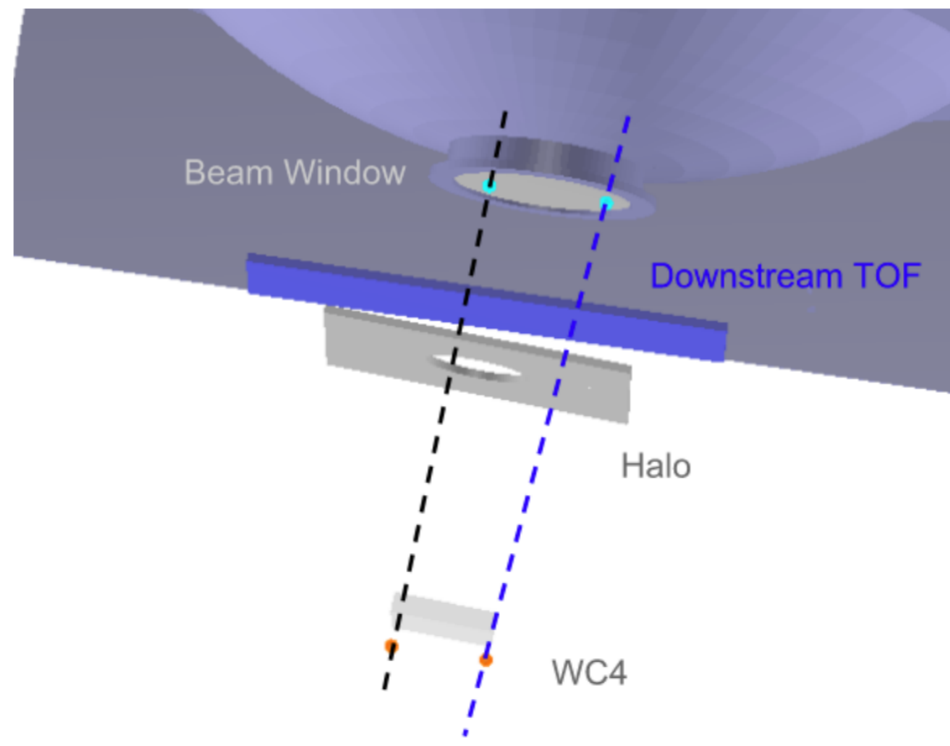


Figure 6.6: Rendering of the portion of the beamline between WC4 and the front flange of the TPC. A halo veto scintillator paddle exists with a hole in the center. Two trajectories are drawn: one through the plastic of the paddle, and other through the hole. Particles that pierce the plastic will have a higher energy loss.

Material	density (g/cm ³)	width (cm)
Fiberglass laminate (G10)	1.7	1.28
Liquid Argon	1.4	3.20
Stainless Steel	7.7	0.23
Titanium	4.5	0.04
Air	0.0012	89.43
Plastic Scintillator	1.03	1.20 (+1.30)

Table 6.1: Material Budget between WC4 and TPC active volume. Energy loss in any given material is proportional to density*width.

the pion when it was fired from WC4. Therefore, separating the simulation by whether the pion hit the paddle or not and plotting P_x vs x at WC4 will give the allowed phase space. This phase space is shown in figure 6.7. Using logistic regression, a line in position-momentum space can be found that separates the two samples. Pions that are expected to hit the paddle, and therefore require a higher energy loss, are ones with a P_x and X that satisfy the following equation

$$P_x + 0.02 * X - 0.4 < 0 \quad (6.2)$$

Similarly, pions that are expected to pass through the hole of the paddle, and therefore require a lower energy loss, satisfy the following equation

$$P_x + 0.02 * X - 0.4 > 0 \quad (6.3)$$

This method correctly classified 86% of the pion DDMC events. The energy loss associated to a MC pion that projects through the halo scintillator is $E_{Loss} = 32 \pm 4$ MeV and $E_{Loss} = 24 \pm 3$ MeV for MC pions that project through the hole of the paddle.

After this analysis was complete, an error was found in the geometry that added an extra 3 cm of argon before the active volume of the TPC, artificially increasing the amount of argon the simulated pions traveled and increasing the energy loss of those pions. As this argon is not present in data, the expected energy for data is slightly less, $E_{Loss} = 24 \pm 6$ MeV for tracks that hit the halo paddle, and $E_{Loss} = 17 \pm 6$ MeV for tracks that project through the hole in the paddle. The

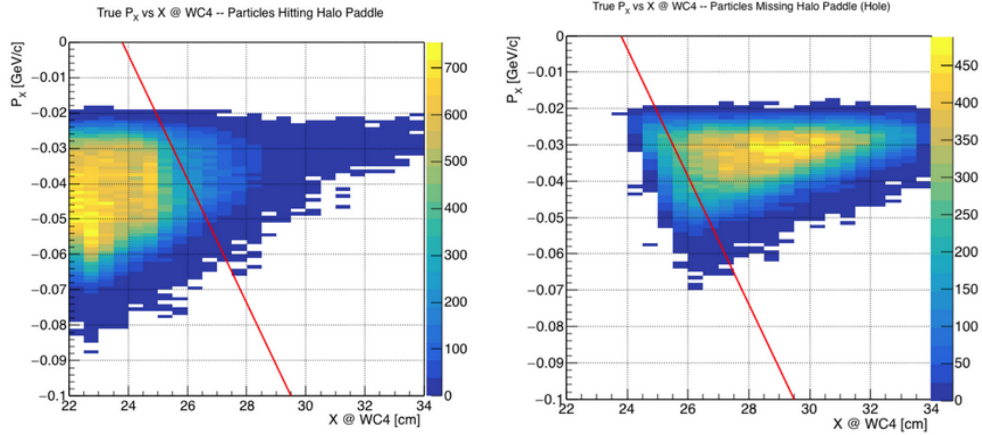


Figure 6.7: The P_x vs X_{WC4} for particles that hit the halo paddle (left) and that miss the halo paddle (right). Using the linear regression fit (red) correctly disambiguates 86% of pions in the sample.

uncertainty associated to the energy loss in data, 6 MeV, is determined from the standard deviation of the full double peaked distribution in figure 6.5.

6.3 Beamline Composition

Data Driven Monte Carlo creates a pure sample of a particular particle species for MC analyses and background contamination studies. However, without knowledge of the composition of particles in the beamline, MC and data analyses cannot properly weight MC samples. This section discusses the creation of the beamline simulation and composition studies. As this was another section of the analysis to which I greatly contributed, I provide a more indepth explanation.

6.3.1 Simulation Geometry, Spill Creation and Trigger Finding

The geometry used for beamline simulation is a simplified version of the experimental hall geometry, in order to increase computing speed. Detector support apparatuses are removed; all detector volumes exist as floating sensitive volumes, made of the appropriate material for the detector, with plastic frames for the WCs. The copper target and both steel collimators are present and in the proper position. To track particles exiting the upstream collimator, a pseudo detector, called

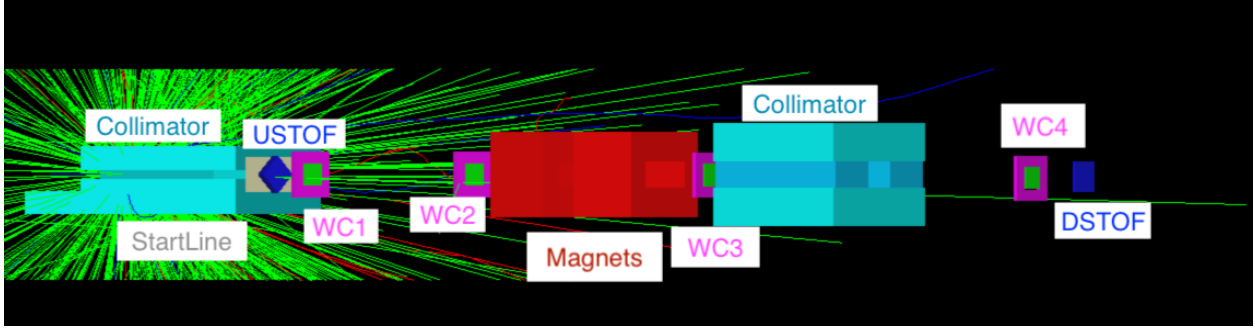


Figure 6.8: The simplified geometry used for beamline simulation. Collimators are in cyan, Start-Line in grey, TOFs in blue, WCs in green with pink G10 frames, and steel of the magnets in red. Target is inside the upstream collimator (not pictured). Green lines are particles produced for the test event, bounded by the defined world volume.

“StartLine”, is added, and is only used for debugging purposes. Though the steel of the magnets are placed in the beamline, the fringe fields of the magnets in the experiment hall are not known; the G4Beamline default configuration for fringe fields is used for simulation. The only parameters set for simulation are the square field approximation parameters, B_{Eff} and L_{eff} , explained in section 4.2. Though the experimental magnets have slightly different response curves, the simulated magnetic fields are identical. A schematic of the beamline is shown in figure 6.8.

Events are simulated individually. For an event, a 64 GeV π^+ is fired at the copper target from 50 cm away. The daughter particles from the interactions inside the target are tracked, and information, such as position, momentum, time, and mother pion ID, is recorded for daughters that enter any Wire Chamber, Time of Flight paddle or Startline. Each pion on target exists in its own universe, without knowledge of other simulated pions. The goal becomes to create beam similar to data taking conditions, with the correct intensity and accelerator beam timing structure. During data taking, a scintillator paddle was installed in the secondary beam pipe before the target to monitor the intensity of the beam (subsection 3.1.1). Though the intensity varied between 100,000-500,000 counts, on average, 350,000 counts were registered in the scintillator paddle per spill. To reflect this in simulation, pions on target, and all daughters from them, are grouped into spills of 350,000 each.

For each pion on target simulated, a random time between 0-4.2 seconds is drawn, using the beam structure from the accelerator as a probability distribution (subsection 3.1.1); all daughters

from that pion have their time of arrival in all detectors offset by that RNG-drawn time. With this offset, the spill has the proper intensity and timing distribution as occurred during data taking conditions. An additional delay is added to all hits within a certain detector to simulate the cable delays. These delays were: [18, 15, 10, 5, 0, 0] ns, for the USTOF, the four wire chambers, and the DSTOF, respectively. Hits in the upstream detectors will be delayed such that when the particle hits the downstream detectors, the delayed upstream hit and the downstream hit will be synchronous, making trigger finding easier. The actual time of a hit, in a given detector, used for event triggering is:

$$t^{hit} = t^0 + t^{RNG} + t^{delay} \quad (6.4)$$

With the creation of a spill, the next stage is to sort through the charged daughters in the spill to find time coincidences among the beamline detectors. When a particle enters a given detector, a 100 ns gate is used to find coincidence with other detectors, with a 10 ns mutual coincidence requirement. During a spill, for each charged-particle hit in the DSTOF, a 100 ns window is opened. Then, for each charged particle hit in WC4, a 100 ns window is opened. If these windows overlap by at least 10 ns, then the two hits are in coincidence. These hits are checked against all charged particle hits in WC3, each with a 100 ns window. If the 10+ ns overlap is maintained across DSTOF-WC3-WC4, the process continues, until a combination of hits across all six detectors are in coincidence, with at least a 10 ns overlap. Trigger conditions are also possible if WC3 is not in coincidence or WC2 is not in coincidence, though not both at once. This allows three-point WC tracks to be reconstructed (section 4.2). The time associated to the trigger, $t_{trigger}$, is set as the start of the coincidence overlap.

During data-taking, once a trigger is issued, the readout buffers for each detector are saved. If two triggers are sufficiently close in time, the readout buffers for those triggers would overlap, and multiple events would be created from the same set of particles. To prevent this, once a trigger is issued, a dead-time equal to the buffer readout window is implemented for each detector where it cannot issue another trigger. As such, readout buffers cannot overlap. In simulation, once all triggers for a spill are found, if two triggers are within a readout window of each other, the later one is removed. For each trigger in this filtered down list, particles within the readout window for each detector are saved to be used for reconstruction.

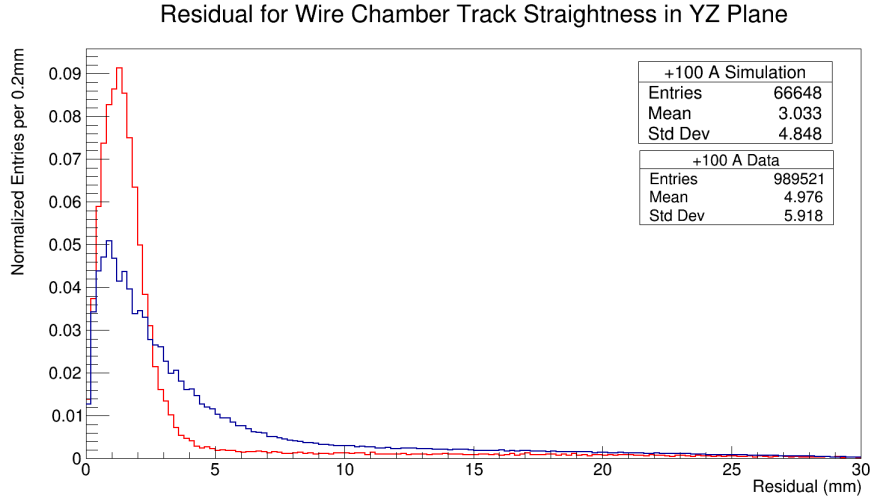


Figure 6.9: Using eq 4.5 and applying to both the data and the simulation, the area normalized plot of data 4 point HY WC tracks (blue) and simulated 4 point WC tracks is plotted (red). The cut is placed at 12 mm.

6.3.2 WC Tracking and TOF Reconstruction

For each trigger, there are a collection of hits in each detector. As described in 4.2, noise effects occur in data, which are not simulated directly. To account for this, for each hit used as part of the simulation WC reconstruction, a 2 mm gaussian smearing is applied to the X, Y, and Z coordinates. This smearing simulates the effect of noise in a WC causing hits on not only the nearest wires to a passing particle, but also the nearest neighbor wires.

This smeared collection of hits can be processed similarly to data using a ROOT macro. As described in 4.2, the combination of hits used, one from each detector, is the set that is the most co-linear, subject to a threshold cut (Eq 4.5). There is a disagreement between simulation and data when plotting the residual over the samples, shown in figure 6.9. This most likely due to mis-reconstruction in data due to matching X and Y hits from different particles inside a wire chamber; In simulation this mis-match does not occur. Though the position of the simulated hit is smeared, the 3-D position of a simulated hit is known, unlike in data. A cut is placed at 12 mm in both simulation and data, which admits 87% of data events and 93% of simulated events. This cut is conservative and could be further tuned, but at 12 mm, this cut avoids the differences in the shape of the data and simulation distributions.

Once the combination of hits is chosen for the trigger, the momentum is calculated using equation 4.9. At this point, a comparison can be made between the reconstructed momentum for the event, and the true momentum of the particles used to make the track. In particular, the reconstructed momentum to the true momentum of the particle used to make the hit in WC4 can be compared. Figure 6.10 plots the fractional difference:

$$\frac{P_z^{TrueHitWC4} - P_z^{Reco}}{P_z^{TrueHitWC4}} \quad (6.5)$$

for the tracks in the +100 A simulation. From this plot, there is a systematic offset, where the reconstructed momentum is 2.6% higher than the true momentum of the particle in WC4. To correct for this in data, the reconstructed momentum is reduced by 2.6%. The +60 A plot is not shown, however, that sample suggested the same shift and resolution. To note, this correction factor has already been applied to data plots of the reconstructed momentum.

The event also undergoes the aperture cuts discussed in 4.2.4. The underlying distribution of midplane matching ΔX and ΔY are shown in figure 6.11. In data, a 3 mm offset appears in the ΔX plot, though this offset does not occur in simulation. Moreover, data has broader tails, suggesting data has more poorly reconstructed tracks than simulation. These effects are not present in the ΔY distribution. It is assumed this is a currently unknown difference in the geometry between simulation and data. Simulation is shifted 3 mm to create overlap of the peaks, and the same cut is applied as in data, as specified in 4.2.4. Truth studies performed with and without this 3 mm shift affected the overall beamline particle composition by <0.2%, which is considered negligible for this analysis.

A time-of-flight (TOF) is also reconstructed for the simulated event. Similar to the WCs, the TOF paddles can have multiple hits during an event, so every permutation of USTOF and DSTOF hits must be checked. A TOF is reconstructed for the event if there exists only one pair of hits in the USTOF and DSTOF that reconstruct a TOF between 10-100 ns. Blindly applied to simulation, the efficiency of the TOF reconstruction was significantly lower than in data, and eliminated many simulated events tagged as an positron. There are two reasons for this. In simulation, the exact time of a hit is known. However, the real TOFs have a sampling rate of 1 ns. Moreover, the PMTs in each TOF paddle have pulses that can last multiple time samples. If multiple particles pass through a TOF at the same time, such as when an positron is part of a shower, a simulated

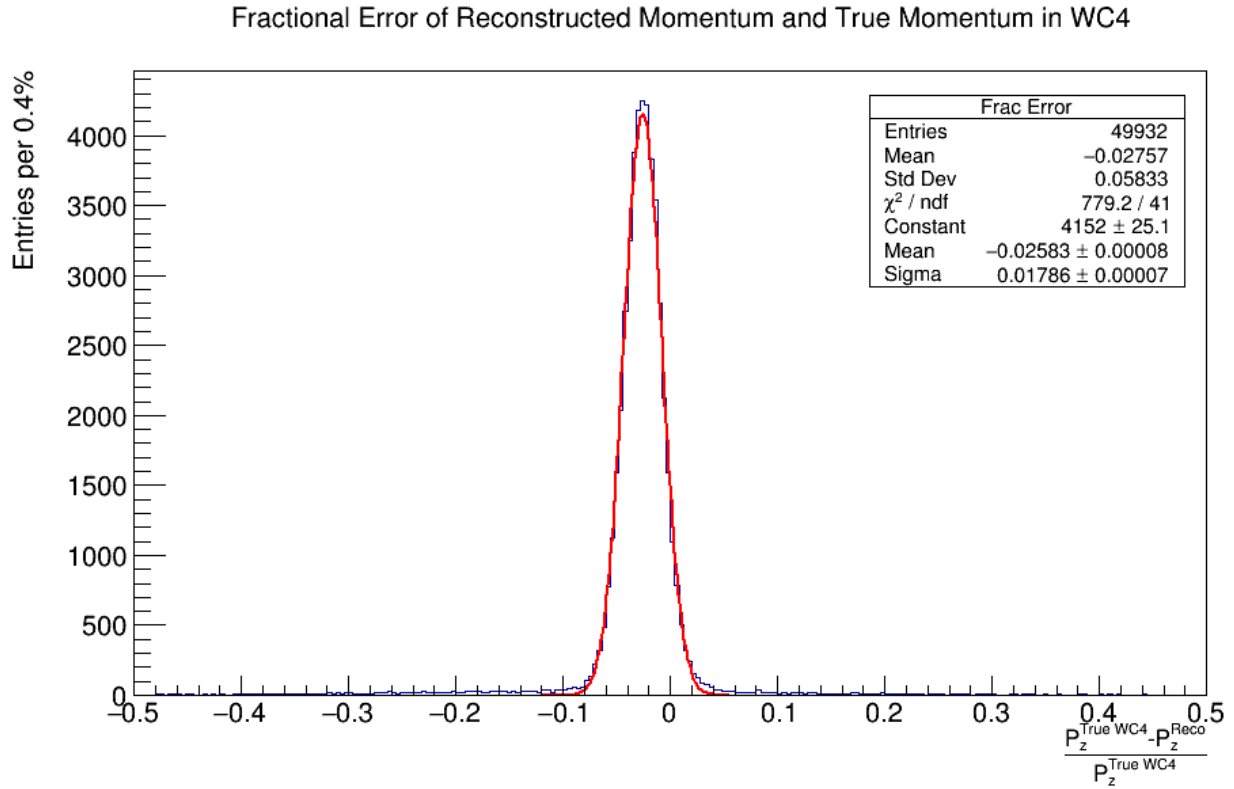


Figure 6.10: For +100 A four point tracks, the fractional between the true momentum of the particle in WC4 and the reconstructed momentum for the track. From this plot, a -2.6% offset is applied to data.

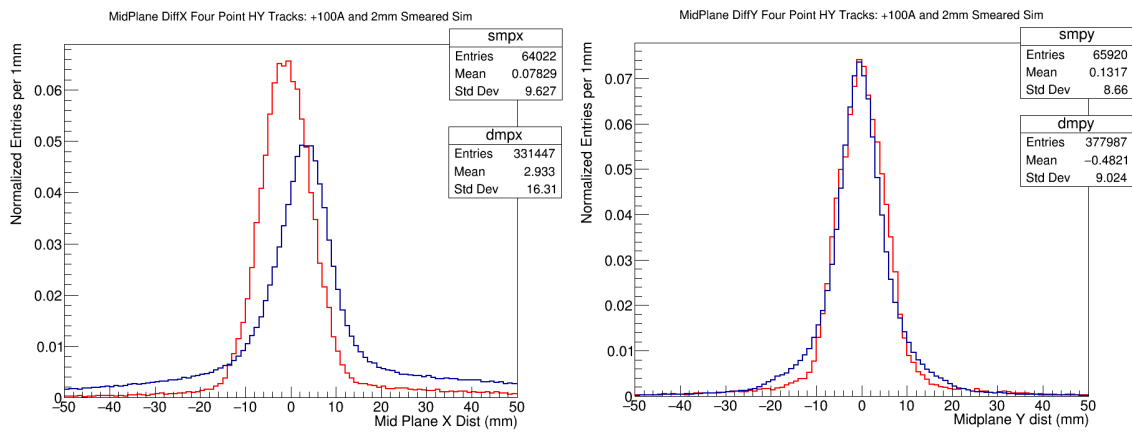


Figure 6.11: Comparison of midplane matching ΔX (left) and ΔY (right) between data (blue) and +100 A simulation (red). While ΔY agrees, there is a shift and higher population of the tail in the ΔX data plot. Plots are area normalized.

event would distinguish every positron, creating multiple nearly identical TOFs for the event in the necessary range, and reject the event. A data event would see pulses stack in the TOF paddle, and the waveform analysis used for finding hits in a paddle would create only one hit out of the many positrons passing through the paddle (section 4.1). Only one TOF would be reconstructed for the event in the necessary range, and the event would be accepted. To apply this data-based effect in simulation, a 20 ns dead time was applied to the TOF simulation, where any hit found within 20 ns after another hit would be ignored for the TOF reconstruction.

6.4 Beamline Composition Analysis

With the beamline reconstruction of momentum and TOF, comparisons can be made between the data and simulation distributions, separated by current setting, +60 A and +100 A, and WCTrack conditions: four point high yield, WC2-missed three point track, and WC3-missed three point track. A four point picky track analysis is also possible, but is statistics limited in data. Moreover, all four point picky tracks are also contained in the four point high yield set. Therefore, the only four point analysis performed is the high yield analysis.

6.4.1 Four Point Analysis

Using the distribution of simulation in figure 6.9 to apply a 12 mm cut, the midplane matching described and plotted in figure 6.11, as well the aperture cuts described in subsection 4.2.4, the underlying distributions for the +100 A simulation analysis are the momentum and TOF plots which are shown in figure 6.12. Using Eq 5.1, the TOF and momentum reconstructed for an event can be used to calculate a mass hypothesis for the event, shown in figure 6.13. From these plots, it is evident there are data effects that are not captured in the simulation. Though the momentum spectrum roughly agrees, two effects are noticeable in the TOF plot. First, the simulated TOF is too sharply peaked, an expected effect given the timing resolution in the actual TOF paddles, which is not simulated. This can be corrected through smearing of the TOF distribution. This effect is amplified in the reconstructed mass plot, where differences in the TOF become more pronounced.

Second, the simulated TOF distribution suggests there are too many slow particles found in

data, which may be due to beam structure instead of a disagreement in composition. When the beam structure is simulated, it is assumed the probability of beam arriving in any given pulse is uniform, which is generally not true in data. Figure 6.14 below plots of the integrated flux in data, over a few spills. If the probability of beam is uniform, the trace of MC7SC1 (yellow) would be linear, which is obviously not the case. These plots were available in real time for monitoring, but not saved in the data flow. Anecdotally from shift taking, these plots could vary from shift to shift, making an estimation of data-based intensity impossible, leading to the zeroth order approximation in simulation of a constant flux.

During instances when beam is more intense during a spill, it is possible to get accidental TOF matching of particles from one pulse with particles from the next pulse. As explained in section 4.1, because the time spacing between pulses is approximately 21 ns, when this mis-matching occurs, events that would reconstruct a TOF in the low TOF peak would instead reconstruct a TOF 21 ns higher, overlapping with the TOF peak of the protons. It is also possible that protons could be matched with faster particles from the previous pulse, creating a lower TOF for a proton. The first case introduces an inefficiency in finding pions, as the reconstructed mass would be higher than expected. The second case introduces an extra background in the pion events from protons. The second case could also explain the existence of more superluminal particles being reconstructed as negative mass in the data; a relatively fast proton being reconstructed with a TOF 21 ns lower than expected could become superluminal.

If the only effect was the timing resolution, a smearing of the simulated TOF could be performed. By choosing various smearing factors for the simulated TOF, a χ^2 test with the data TOF could guide an appropriate smearing factor for the TOF. However, given the effects of the non-constant beam intensity and timing structure in data which is not replicated in the simulation, both of which cannot be described by a simple gaussian smearing, any attempt to apply this method will return a poor χ^2 . Therefore, no smearing can be done on the TOF distribution. Moreover, using the mass plot to make any comparisons also fails, given the TOF needs some form of correction to make the simulated mass reconstruction agree with data. It is left to a future analysis to tag these TOF accidentals in data to remove them so the simulated and data distributions are more comparable.

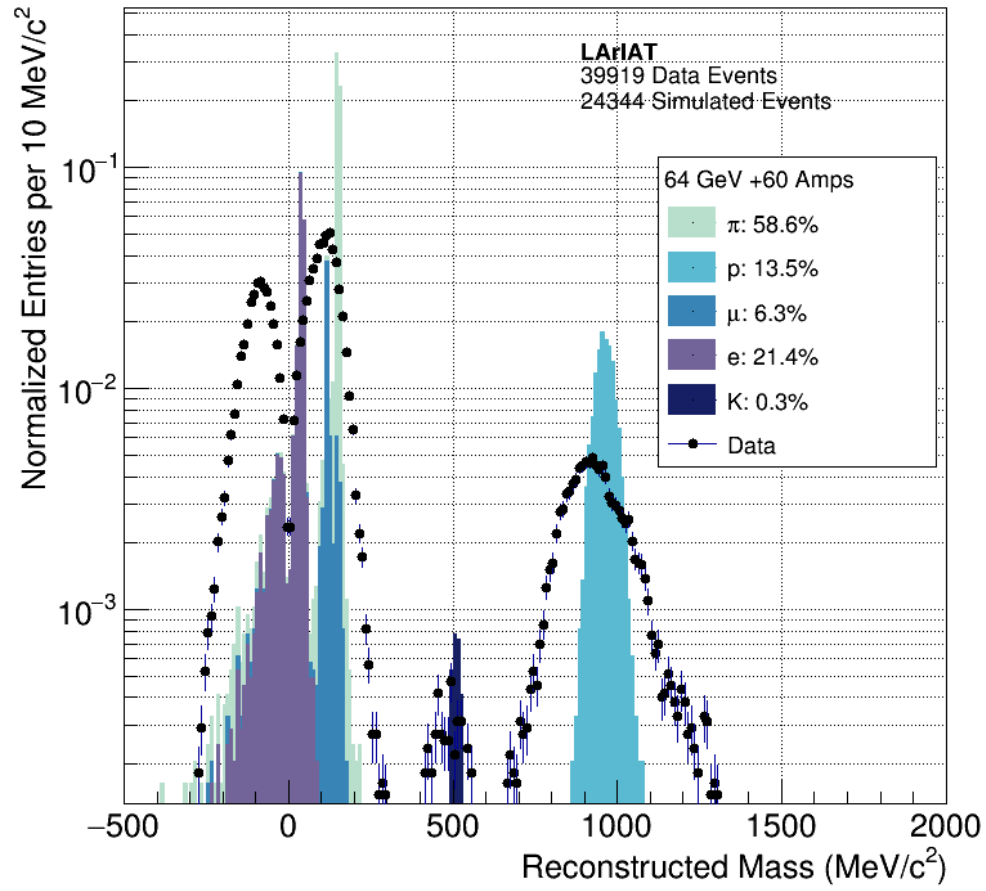


Figure 6.17: Reconstructed mass comparison using TOF and momentum for simulation and data. Superluminal events are given negative mass.

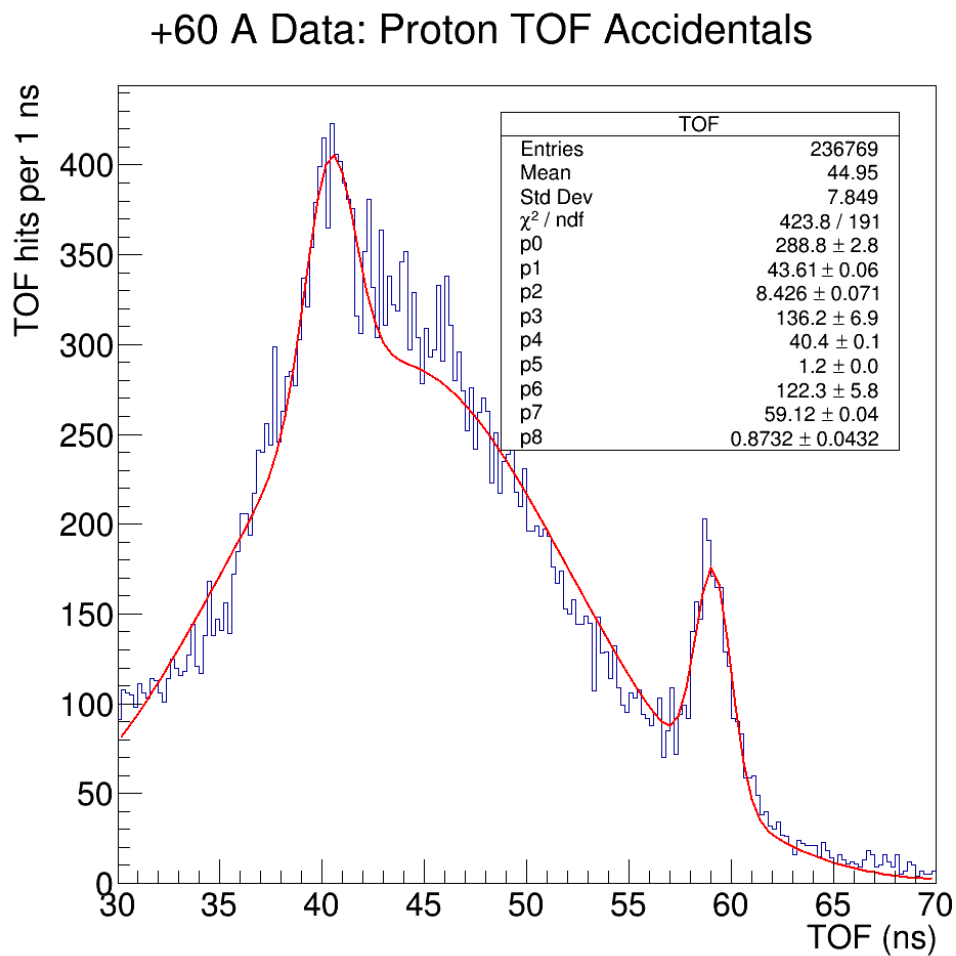


Figure 6.18: Fitting TOF accidentals over data proton TOF peak. For the proton peak, 40 ns accidental, and 59 ns accidental, the fit parameters of normalization, mean and sigma are given in table 6.2.

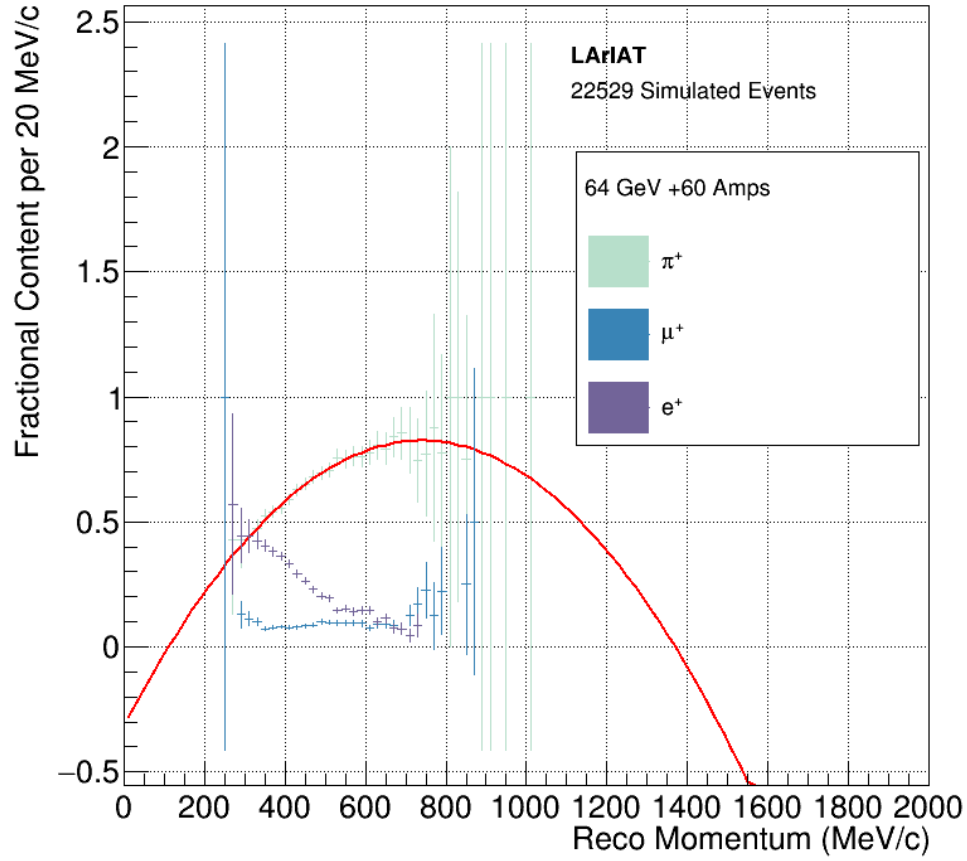


Figure 6.19: Fractional content of +60 A low mass particles with second order polynomial fit for pion content shown (red). Note fit parameters suggest a negative composition when extrapolated away from the possible range of momentum.

1853 as a function of momentum. The content from $\pi/\mu/e$ per bin of momentum is given in figure 6.19.

1854 The fit parameters which define the composition are given by the following:

$$C(p_\pi) = -2.06 * 10^{-6} * p^2 + 3.07 * 10^{-3} * p - 0.312 \quad (6.10)$$

$$C(p_\mu) = -1.01 * 10^{-7} * p^2 + 1.55 * 10^{-4} * p + 0.037 \quad (6.11)$$

$$C(p_e) = 2.16 * 10^{-6} * p^2 - 3.22 * 10^{-3} * p + 1.27 \quad (6.12)$$

$$(6.13)$$

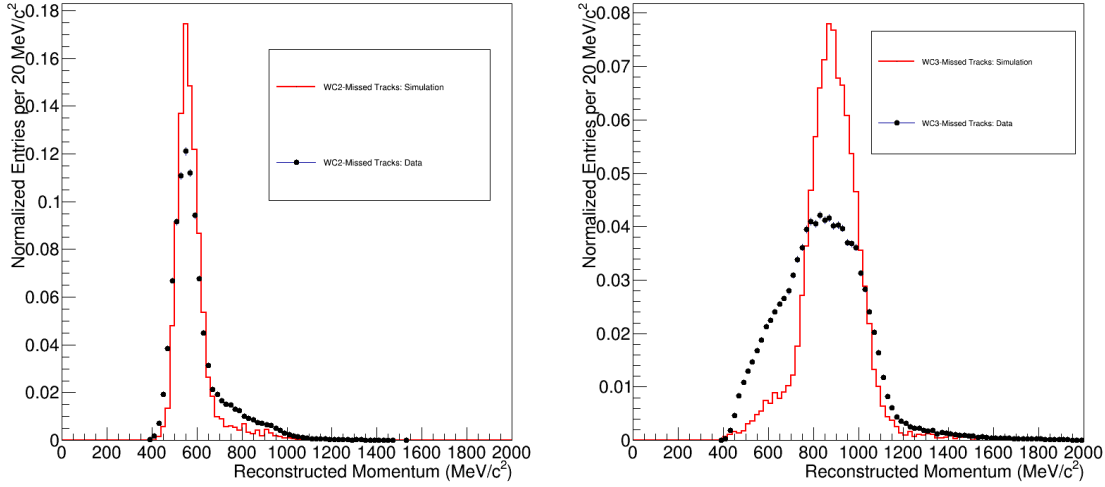


Figure 6.20: WC2-Missed tracks (left) and WC3-Missed tracks (right). Each plot shows the area normalized simulated momentum distribution (red) to normalized data (black).

6.4.2 Three Point Analysis

As noted in chapter 5, though three point wire chamber tracks are reconstructable in data, only four point tracks were used for the analysis. This section discusses the differences between the three and four point reconstruction of simulation and describes why three point tracks are not used, using the +100 A simulation and data sets.

As was shown for the four point analysis, the momentum distributions of simulation and data for the WC2 and WC3 missed tracks are given in figure 6.20, without separating by particle species. Compared to figure 6.12, there is a much larger disagreement between data and simulation. Simulation would suggest there a significant number of tracks in data that are being misreconstructed at a higher momentum for WC2-missed tracks or at a lower momentum for WC3-missed tracks. Similar to the four point analysis, the reconstructed momentum can be compared to the true momentum of the particle used to make the hit in WC4, using equation 6.5.

The error for all four point tracks and all three point tracks are shown in figure 6.21. Also shown is the percentage error vs reconstructed momentum for three point tracks. Though both distributions peak at 0%, the three point distribution is broader, suggesting a larger uncertainty on the momentum. Moreover, three point tracks have a large shoulder past 20%. From the second

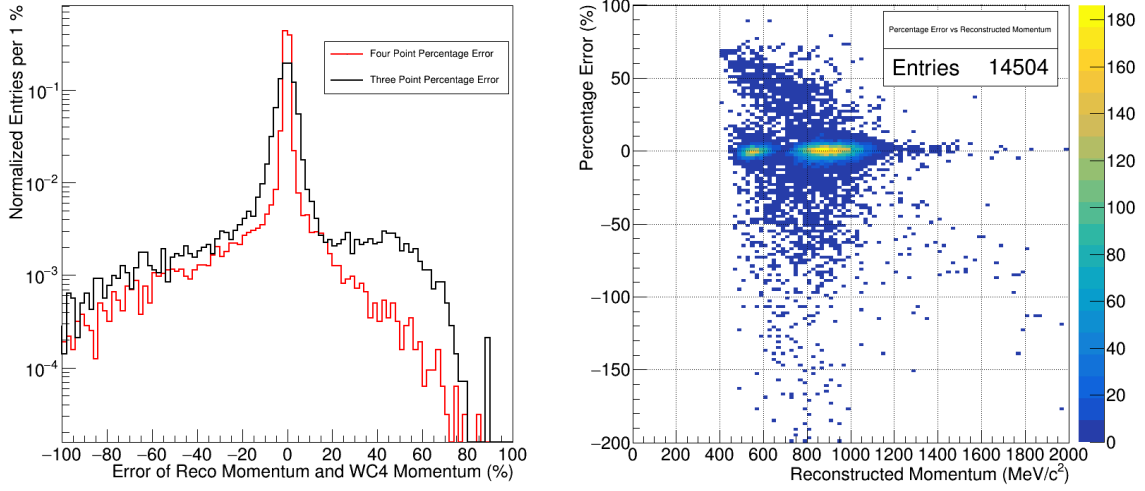


Figure 6.21: Left: Percentage error comparison of three point tracks (black) and four point tracks (red). Right: Percentage error vs reconstructed momentum for three point tracks.

plot in figure 6.21, this error is not restricted to a particular range of momenta. This makes it impossible to remove a band of three point tracks in data and be confident the removed tracks were poorly reconstructed. Given the higher uncertainties associated with using three point tracks in the analysis, and given four point tracks have enough statistics for an analysis and the uncertainty associated with those tracks can be well calculated, only four point tracks are considered for the cross section in this analysis. It is left to future analyses to understand three point tracks in simulation to incorporate them back into the data set.

6.5 Selection of DDMC Events

This section describes the DDMC event selection for the DDMC portion of the cross section analysis. As the generation of the DDMC events uses events that have passed some data cuts, the event reduction for DDMC begins with TPC reconstruction. As explained previously, approximately 550,000 events were created for protons, and 550,000 events which were a mixture of pions, muons and positrons were created. As the explanation for how these cuts were applied were given in chapter 5, this section is brief, showing noteworthy plots and the overall event reduction for each particle species.

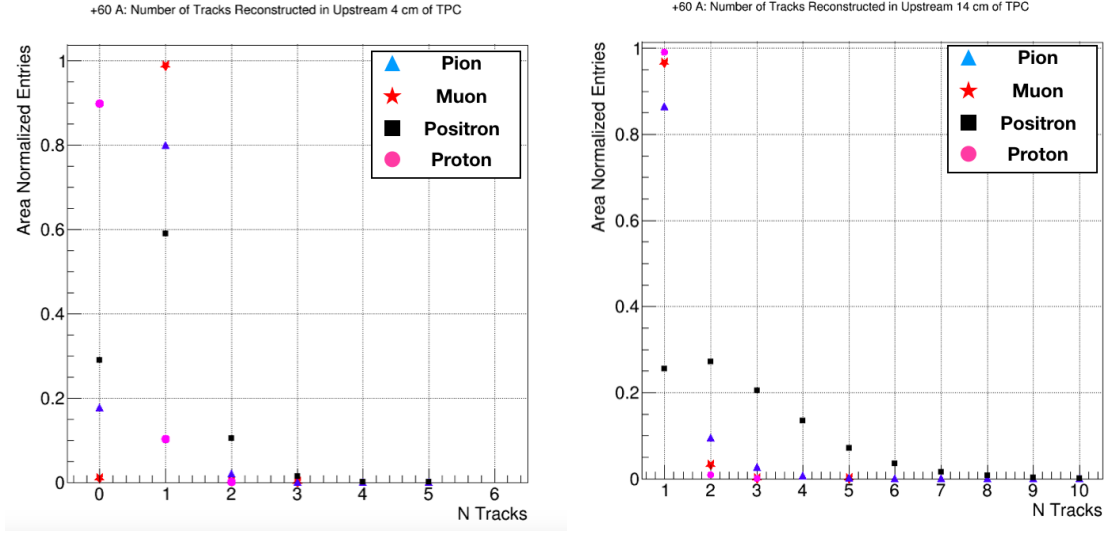


Figure 6.22: The upstream track existence cut and pileup filter cut for the +60 A DDMC samples (log scale). Pions are in blue, muons in red, positrons in black and protons in pink.

For the +60 A sample, 352,000 pions, 45,000 muons, 131,000 positrons and 531,000 protons are simulated and reconstructed. The +100 A sample consists of 453,000 pions, 46,000 muons, 44,000 positrons and 544,000 protons. Figures 6.22 and 6.23 shows the normalized number of tracks reconstructed in the upstream 4 cm and 14 cm of the TPC for the four species simulated.

It is interesting to note that while there is general agreement in the shapes of each species when comparing both current settings, the +60 A protons have a high rate of failure when the upstream track existence cut is applied. While the +100 A protons have about a 15% failure rate, the +60 A protons have a 90% failure rate.

From figure 6.4, the mean momentum for the +60 A DDMC sample is $472 \frac{\text{MeV}}{c}$. A proton at this momentum has a kinetic energy of 110 MeV. According to NIST tables [38], the stopping range for a proton at 100 MeV is 15 cm in argon. From section 6.2, there is a total of 6 cm of dead argon before the TPC. Moreover, as reconstruction does not reconstruct tracks within the first 3 cm of the active volume of the TPC, there is a total of 9 cm of argon the proton must travel before information can be reconstructed. Including the plastic of the scintillator in the DSTOF and halo paddle, as well as the steel of the cryostat and plastic of the TPC frame, it is highly likely a 110 MeV proton will stop before a track can be reconstructed. In this case, there will no track reconstructed in the TPC and the event will fail. For data, it is expected the true pass rate for the

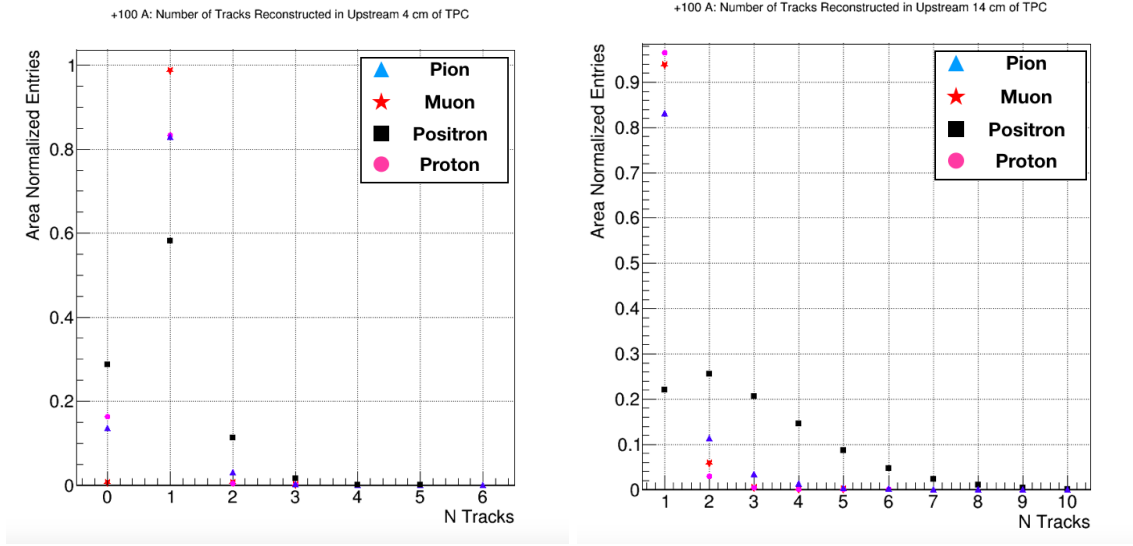


Figure 6.23: The upstream track existence cut and pileup filter cut for the +100 A DDMC samples (log scale). Pions are in blue, muons in red, positrons in black and protons in pink.

+60 A protons will be slightly higher, given there is only 3 cm of dead argon. However, given the overall rejection rate for +60 A protons from all TPC based cuts, the difference between the data and MC pass rate due to this cut will still leave the proton content negligible.

The WC-TPC match also shows greater disagreement between +60 A protons and +100 A than when comparing other particle species across current settings. Figure 6.24 plots α for the +60 A and +100 A proton DDMC samples. The +60 A sample suggests the WCTrack and TPC track to be matched has a larger difference in angle. This would support the hypothesis that +60 A protons are interacting more often between WC4 and front of the TPC, leading a larger elastic scattering or interaction angle. The other particle species have similar pass rates when comparing across current, and the underlying ΔX , ΔY and α when comparing those species are similar, and are not shown.

The shower filter has different pass rates for +60 A and +100 A positrons. While for the +100 A DDMC sample, the pass rate at $[L_{short}, N_{tracks}] = [10 \text{ cm}, 3]$ was 5.9%, for the +60 A DDMC sample, the pass rate is slightly higher, 10.9%. Similar to the positron pass rate for +100 A DDMC in figure 5.8, figure 6.25 shows the total event passing rate for the +60 A DDMC positrons. As +60 A positrons have less momentum, and therefore less energy, once they begin to shower, due to kinematics, fewer electrons and positrons will be created. Therefore, fewer tracks will be

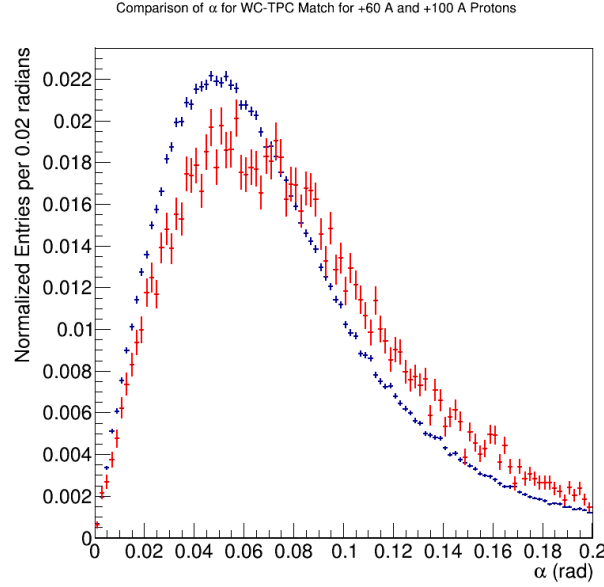


Figure 6.24: For WC-TPC matched DDMC protons, the distribution of α for the +100 A (blue) and +60 A (red) is shown. +60 A protons have a broader distribution at a larger α , suggesting +60 A protons scatter more between WC4 and the start point of the TPC track.

1920 reconstructed in the cone ROI, and the positron event will have a higher chance of passing the
1921 filter.

1922 The are two differences in the effect of the PIDA cut when comparing across current samples.
1923 First, as stated in section 5.7, more than 99% of +60 A protons are rejected, but only 96% of the
1924 +100 A protons are rejected. This difference is most likely due to some +100 A protons not fully
1925 stopping before interacting, creating a more flat $\frac{dE}{dX}$ vs residual range curve, and a lower returned
1926 value for the PIDA.

1927 Second, the proton filter accepts 93% of the +60 A positrons, but accepts only 75% of the
1928 +100 A positrons. Given the proton filter is after the shower filter, the positron events passed to
1929 the proton filter will have fewer tracks reconstructed, on average, than if the shower filter were not
1930 used. However, the positron events will still have a similar total energy deposition, regardless of
1931 how many tracks were reconstructed. If the energy deposition is contained in fewer tracks, due
1932 to reconstruction joining multiple shower electrons and positrons together, then the total energy
1933 deposition per track will be greater. This will increase the $\frac{dE}{dX}$ profile for those tracks, and cause
1934 the proton filter to reject the event. In the +60 A sample, this effect is smaller, as fewer electrons

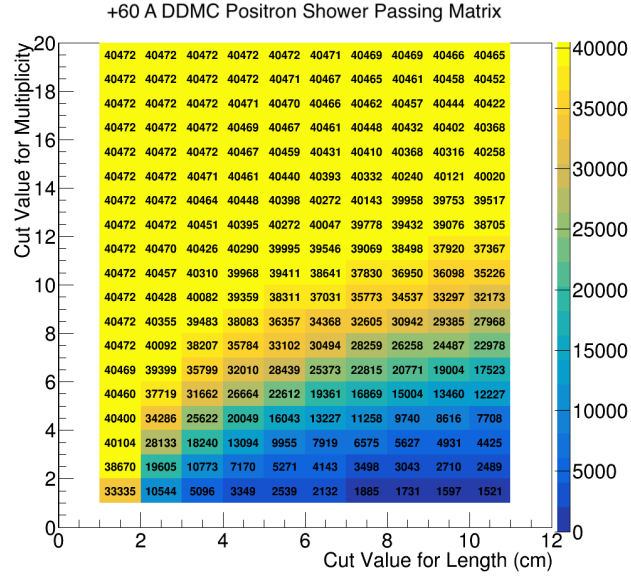


Figure 6.25: Of the +60 A DDMC positron sample reaching the shower filter, the total number of events passing for any given cut value. For $[L_{short}, N_{tracks}] = [10 \text{ cm}, 3]$, 4,425 of 40,472 events pass, for a pass rate of 10.9%. +100 A DDMC positrons have a 5.9% pass rate.

and positrons are created, making track reconstruction more reliable. However, the +100 A sample will have more electrons and positrons created during the shower, and track reconstruction will be more likely to merge electrons and positrons into one track, and cause the proton filter to reject the event. Refining reconstruction techniques to improve the calorimetry of tracks reconstructed from positrons should cause more agreement between the two positron samples, as viewed from the proton filter. However, as positrons are a background to this analysis, the knock-on effect of the proton filter also acting as a positron filter is a benefit, so the proton filter is kept for the analysis.

Finally, a scaling of the proton events is done. As the initial sample was approximately an equal amount of protons and low mass particles, given the beamline composition, protons should be scaled down to match the global composition suggested by figures 6.12 and 6.16.

For the +100 A DDMC sample, a total of 543,000 pions, muons, and positrons are simulated, as well as 544,000 protons. From figure 6.12, the ratio of protons to pions, muons and positrons is 25.6:73.7, or 34.7%. Therefore, the number of protons simulated should be approximately 188,613 events to match the 543,000 low mass particles simulated, scaling down the number of proton events to 34.7% of the original sample. The +60 A DDMC begins with 528,000 pions, muons,

Species/Cut (Cut Survival %)	Pion	Muon	Positron	Proton
Initial Events	352,000	45,000	131,000	531,000
TPC Upstream Track Exists	289,515 (82%)	44,581 (99%)	93,072 (71.0%)	54,116 (10%)
TPC Pileup Filter	288,534 (100%)	44,580 (100%)	80,745 (87%)	54,116 (100%)
Unique WC-TPC Match	223,039 (77%)	44,013 (99%)	40,472 (50.1%)	24,607 (46%)
Shower Filter	220,890 (99%)	44,009 (100%)	4,425 (11%)	24,607 (100%)
Proton PIDA Filter	212,787 (96%)	44,006 (100%)	4,132 (93%)	102 (0.4%)
Scaling of Protons	212,787 (100%)	44,006 (100%)	4,132 (100%)	16 (16%)

Table 6.3: Event reduction table for +60 A DDMC pions, muons, positrons and protons. The final row scales the proton events to match the beamline composition.

and positrons, and 531,000 protons. Figure 6.16 suggests this ratio should be 13.5:86.3, or 15.6%. Therefore, only 82,596 protons should have been simulated, requiring scaling down of the proton events to 15.6%. Table 6.3 shows the event reduction table for the +60 A DDMC samples, with the +100 A DDMC event reduction table in table 6.4. As stated previously, given the final proton background in the +60 A sample is only 0.006%, if the reconstruction effects causing a high failure rate in the TPC existence cut for the protons is not present in data, with data having a pass rate not of 15% but of 90%, then the +60 A proton contamination in data would be 0.036%, which is still negligible. Given how few +60 A proton events are selected after these cuts are applied, the +60 A proton sample is ignored for the MC cross section.

6.6 Proton Contamination Comparison Between Data and DDMC

This event reduction table can be compared to data to infer what the proton contamination in the data set may be, at least for the +100 A sample. As few +60 A DDMC protons survived, cross section plots in the next chapter do not include proton contamination for this MC sample. However, protons in the +100 A would be included given DDMC suggests a 1.4% contamination.

From 5.1, the number of events due to the PIDA cut is reduced from 56,635 to 53,555; 3,080 events are removed. From table 6.4, 4.4% of pions, 24.7% of positrons, 96.3% of protons, and no

Species/Cut (Cut Survival %)	Pion	Muon	Positron	Proton
Initial Events	453,000	46,000	44,000	544,000
TPC Upstream Track Exists	391,005 (86%)	45,702 (99%)	31,339 (71%)	455,419 (84%)
TPC Pileup Filter	388,103 (99%)	45,700 (100%)	25,928 (83%)	455,398 (100%)
Unique WC-TPC Match	315,679 (81%)	45,257 (99%)	13,613 (53%)	375,209 (82%)
Shower Filter	308,348 (98%)	45,199 (100%)	807 (6%)	375,158 (100%)
Proton PIDA Filter	294,899 (96%)	45,199 (100%)	608 (75%)	13,759 (4%)
Scaling of Protons	294,899 (100%)	45,199 (100%)	608 (100%)	4,770 (35%)

Table 6.4: Event reduction table for +100 A DDMC pions, muons, positrons and protons. The final row scales the proton events to match the beamline composition.

muons are rejected by the PIDA filter. The shower filter removes almost all DDMC positron events from the sample, so it is assumed no positrons reach the PIDA filter in data. Finally, from table 6.4, it is assumed the relative fraction of muons to pions reaching the PIDA filter in data matches simulation, such that muons are 14.7% of pions. This sets up a set of linear equations:

$$N_{\pi} + N_{\mu} + N_e + N_p = 56,635 \quad (6.14)$$

$$.044N_{\pi} + 0N_{\mu} + .247N_e + .963N_p = 3,080 \quad (6.15)$$

$$N_e = 0 \quad (6.16)$$

$$N_{\mu} = .147N_{\pi} \quad (6.17)$$

Solving for N_p returns 981 of the 56,635 events reaching the filter were protons, or 1.7% of the sample. With a 96.3% rejection rate, only 36 proton events should remain in the data set, or .07%. When the DDMC is generated, it assumed the proton composition in the DDMC matches the global beamline composition from beamline simulation. However, data enforces a mass cut to remove protons. Therefore, while data has already removed most protons, DDMC is weighted to reflect the case where no mass cut exists, because the mass cut could not be applied to the beamline composition due to the disagreement in the TOF.

By using the proton PIDA filter as a secondary method of rejection for the DDMC, and comparing the effect to data and simulation, the overweighting of protons in the DDMC becomes

1979 evident. Moreover, by comparing the event reduction due to the PIDA filter, an estimate of the
1980 contamination of protons in data after the mass cut can be derived. Under the assumption that
1981 other cuts operate similarly in data and simulation, the difference in the proton contamination
1982 between data and DDMC is solely due to the mass cut being applied in data, but not DDMC. In
1983 data, .07% of the sample are protons after the PIDA cut. For DDMC, 1.4% of the final sample are
1984 protons. This implies the mass cut in data reduces the proton contamination by 95.2%. Given data
1985 suggests such a low percentage of protons in the +100 A sample, and DDMC suggests a similarly
1986 low percentage of protons in the +60 A, it is assumed the final cross section samples in data and
1987 MC are only comprised of pions, muons, and positrons.

Chapter 7

Cross Section Analysis

7.1 Thin Slice Method

1991 Once the data and MC events are selected, the cross section can be calculated. Though LArIAT
 1992 is 90 cm long, by using information from individual wires, the track used for the cross section
 1993 measurement can be sampled approximately every 4 mm. This allows LArIAT to become a series
 1994 of thin slice experiments, where a high statistics measurement can be made from a small sample
 1995 of tracks. Figure 7.1 shows how the thin slices are made. Using this method, the cross section
 1996 calculation can be simplified. For a particle traveling through a medium of number density, n , and
 1997 thickness, z , the probability of survival and probability of interacting is given by:

$$P_{Survival} = e^{-\sigma(E)nz} \quad (7.1)$$

$$P_{Interacting} = 1 - P_{Survival} = 1 - e^{-\sigma(E)nz} \quad (7.2)$$

1998 $P_{Interacting}$ can also be given by $\frac{N_{Interacting}}{N_{Incident}}$, the number of times the particle interacts divided
 1999 by the number of times the particle was fired at the target. The two can be combined, and by
 2000 expanding the exponential:

$$\frac{N_{Interacting}}{N_{Incident}} = 1 - (1 - \sigma(E)n\delta z + \dots) = \sigma(E)n\delta z \quad (7.3)$$

2001 For a thin target, higher order powers of δz can be ignored. We retrieve an equation for the cross
 2002 section:

$$\sigma(E) \approx \frac{1}{n\delta z} \frac{N_{Interacting}(E)}{N_{Incident}(E)} \quad (7.4)$$

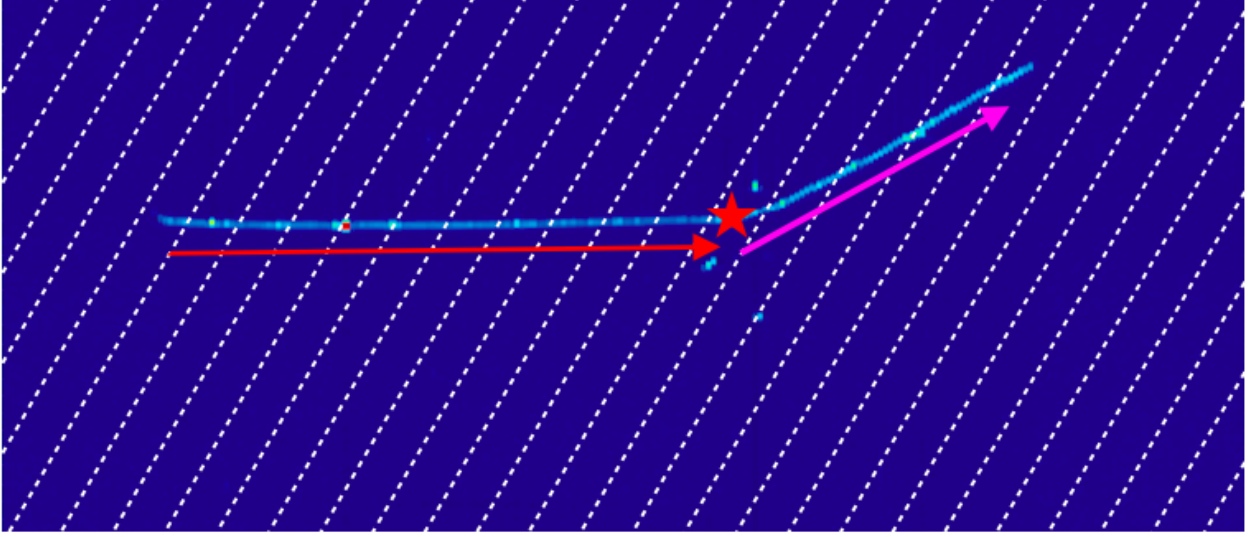


Figure 7.1: Each wire plane divides the TPC into many 4 mm thick, 60° rotated slabs of argon. The cross section candidate track (red) penetrates many slabs before it interacts (star), each representing a thin slice experiment.

2003 The following sections discuss how the energy is calculated, and how $N_{Interacting}$ and $N_{Incident}$ are
 2004 populated.

2005 7.2 Calculation of Energy for a Given Slice

2006 From the beamline reconstruction of momentum (section 4.2), energy loss estimation from simula-
 2007 tion (section 6.2), and the assumption that the cross section candidate is a pion, the kinetic energy
 2008 when the track begins in the TPC can be given by the following equation:

$$KE_{initial} = \sqrt{p^2 + m_\pi^2} - m_\pi - E_{Loss} \quad (7.5)$$

2009 Obviously, this is not the energy of the particle throughout its path through the TPC. As the pion
 2010 travels through the argon, it will lose energy as it ionizes electrons from the surrounding argon
 2011 nuclei. Each wire of the TPC measures this energy loss by collecting this charge and converting
 2012 to an energy gradient, $\frac{dE}{dX}$. This is combined with the geometry of the detector to find dx , and by
 2013 extension, the energy loss, dE . For each slice of argon the track travels, the energy loss in that slice
 2014 is calculated and subtracted from the total energy of the particle, and that new energy stored in a

2015 histogram for $N_{Incident}$. Therefore, the energy at any given slice, i , that is stored in this histogram
 2016 is given by:

$$KE_i = KE_{Initial} - \sum_{j=0}^{j<i} \frac{dE_j}{dx_j} dx_j \quad (7.6)$$

2017 This process iterates until the track ends. For that slice, the incident histogram is filled with the
 2018 energy at that slice, as well as an interacting histogram. Therefore, a track will make many entries
 2019 into the $N_{Incident}$, one for each wire that measured energy deposition for that track, and if the track
 2020 ends inside the TPC, one entry of an $N_{Interacting}$ histogram for the energy measured at the final
 2021 wire associated with the track. If the track is thorough-going, $N_{Interacting}$ will receive no entries,
 2022 as no interaction was found.

2023 7.3 Underlying Data and MC Plots

2024 In this section, the various plots and comparisons between data and the MC admixture are shown.
 2025 These plots build on one another to create the incident and interacting histograms in the next
 2026 section.

2027 7.3.1 $\frac{dE}{dX}$ and Pitch Comparisons

2028 For each hit along the track, a measurement of $\frac{dE}{dX}$ and dX , or track “pitch”, is returned. These
 2029 are shown for both the +60 A and +100 A samples in figures 7.2 and 7.3. The $\frac{dE}{dX}$ distribution is
 2030 described by a Landau function for the underlying physics, convolved by a gaussian for electronics
 2031 response. A fit is applied to both data and MC and the fit parameters shown on the plot. Though
 2032 the pitch agrees between the +60 A samples, there is a disagreement between the $\frac{dE}{dX}$ for data and
 2033 MC. As data has a higher $\frac{dE}{dX}$ profile, the 6% higher MPV means 6% more energy will be subtracted
 2034 per slice. For the +60A data, this means entries of the incident and interacting histograms will be
 2035 at lower KE bins compared to the MC.

2036 7.3.2 $\frac{dE}{dX}$ vs Residual Range Comparison

2037 If a particle stops inside the detector, it should increase how much energy it loses to ionization. This
 2038 is the Bragg peak for a stopping particle, and can be observed by plotting $\frac{dE}{dX}$ as a function of the

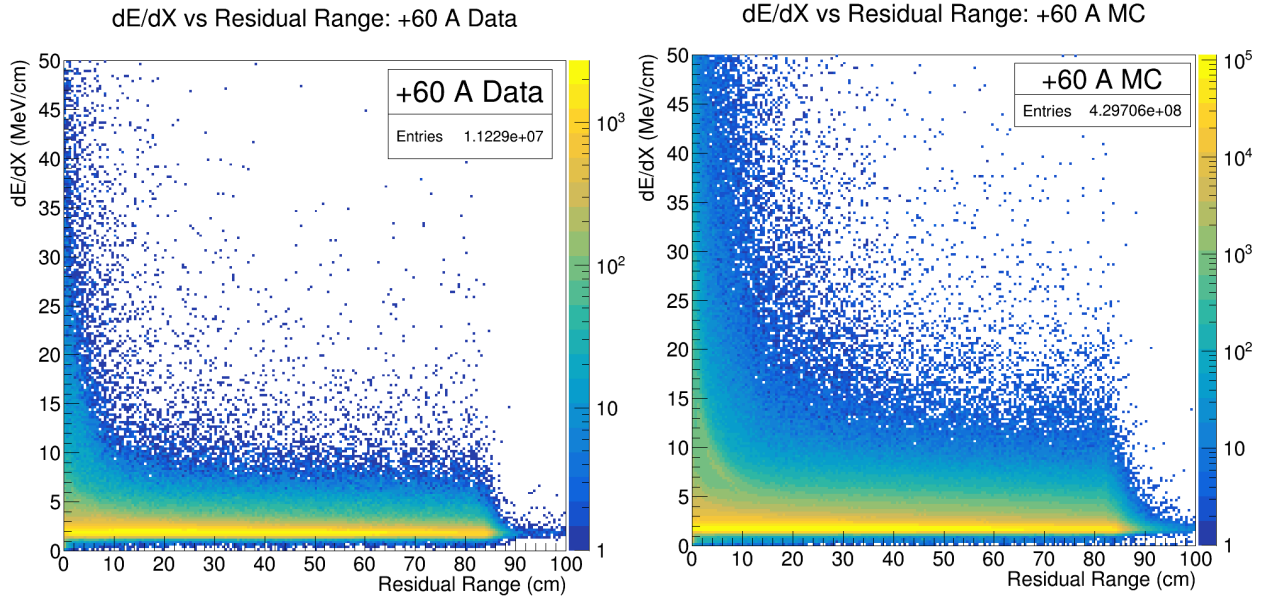


Figure 7.4: $\frac{dE}{dX}$ vs residual range for +60 A data (left) and +100 A MC (right). Color is in log scale.

distance from the end of the track, or residual range. If a particle is not stopping, instead ending a track because of an interaction, this peak will not be visible for that particular track. However, even if a track is not stopping, the comparison of $\frac{dE}{dX}$ vs residual range is helpful for locating proton backgrounds in the sample, if any survived the PIDA cut, or to access a systematic on the proton contamination. The plots of $\frac{dE}{dX}$ vs residual range for data and MC are given in figures 7.4 and 7.5.

7.4 Calculating the Cross Section

As shown in equation 7.6, with a measurement of $\frac{dE}{dX}$ and dX for each hit along a track, the total kinetic energy can be calculated for that point. With that energy, the incident and interacting histograms can be filled for the MC and data set, and are shown in figures 7.6 and 7.7. The “pion secondaries” in each plot are events where the initial DDMC particle was a pion, but interacted before the TPC, creating a secondary particle. These events are discussed in section 7.5.1.

The scaling factor to translate from the ratio of the incident and interacting histograms to a cross section is to divide by the number density of target argon nuclei and the thickness of the slab,

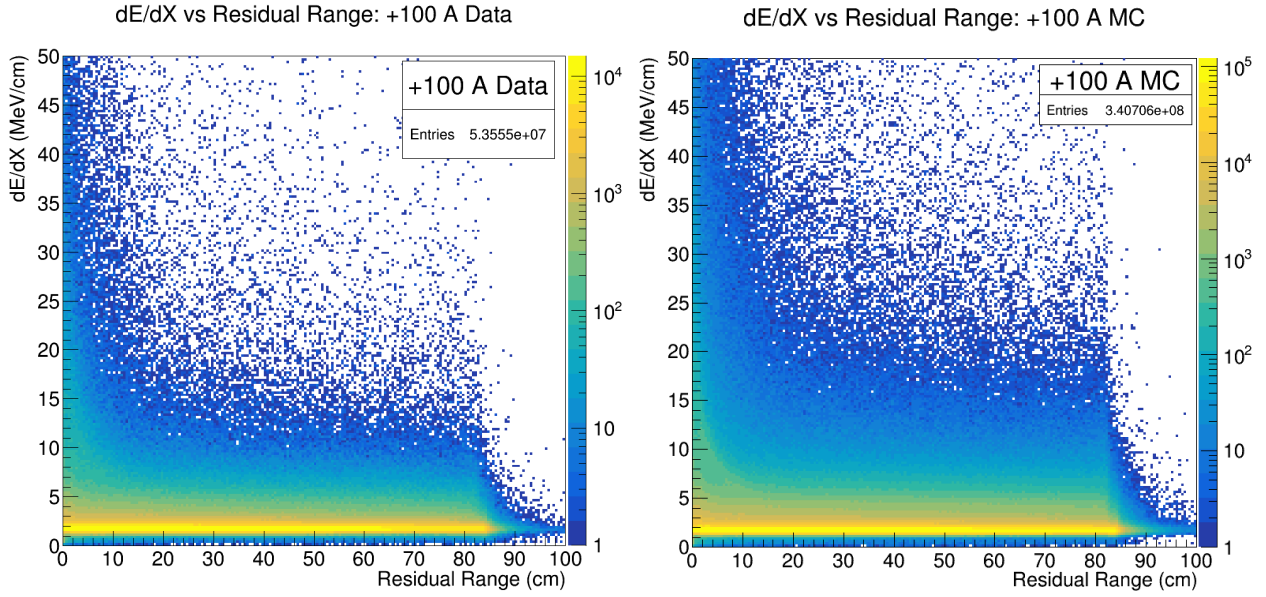


Figure 7.5: $\frac{dE}{dX}$ vs residual range for +100 A data (left) and +100 A MC (right). Color is in log scale.

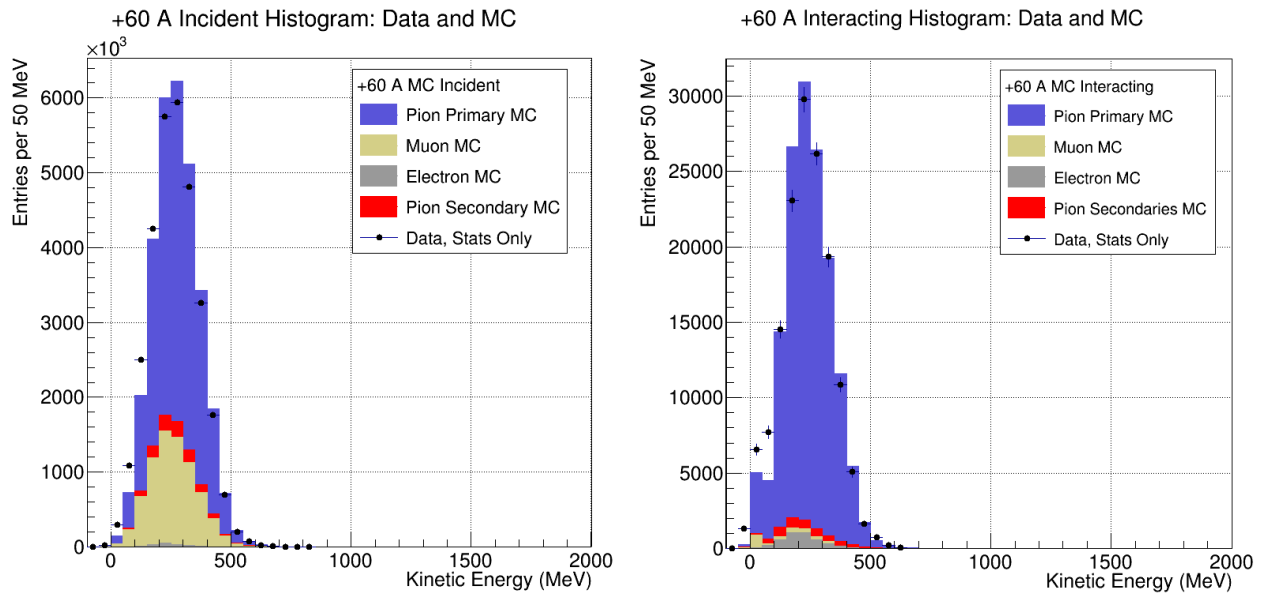


Figure 7.6: Left: Incident histogram for data (black points) and MC (histogram, colored by species). Right: Interacting histogram for data (black points) and MC (histogram, colored by species). Data is scaled to match the number of MC fills.

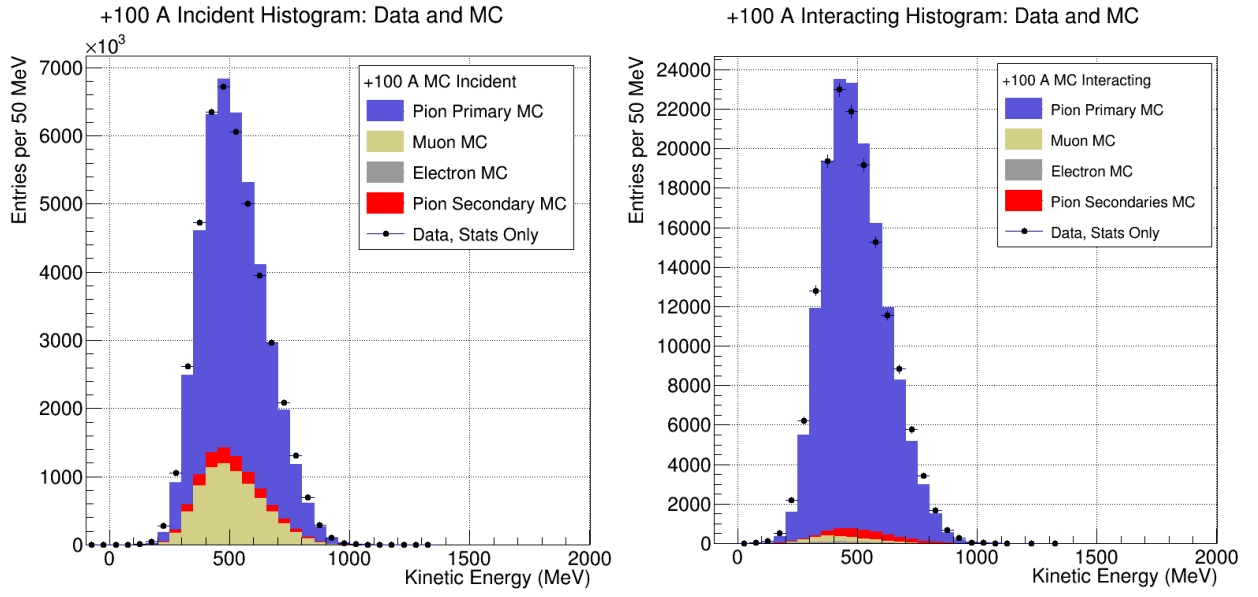


Figure 7.7: Left: Incident histogram for data (black points) and MC (histogram, colored by species). Right: Interacting histogram for data (black points) and MC (histogram, colored by species). Data is scaled to match the number of MC fills.

which is the pitch. For liquid argon, given the mass density (ρ), molar mass (M), and Avogadro's number (N_A), the number density of nuclei in liquid argon is:

$$n = \frac{\rho * N_A}{M} = \frac{1.396 * 10^6 \frac{\text{g}}{\text{m}^3} * 6.022 * 10^{23} * \frac{1}{\text{mol}}}{39.95 \frac{\text{g}}{\text{mol}}} = 2.104 * 10^{28} \text{m}^{-3} \quad (7.7)$$

Given the pitch distributions in figures 7.2 and 7.3, though larger measurements of pitch are possible, the peak of the distributions are used for all slices, 4.7 mm. Therefore this conversion factor is:

$$\frac{1}{n\delta z} = \frac{1}{2.104 * 10^{28} \text{m}^{-3} * 4.7 * 10^{-3} \text{m}} = 1.011 * 10^{-26} \text{m}^{-2} = 101.1 \text{ barn} \quad (7.8)$$

The ratio of the histograms in figures 7.6 and 7.7, with a scaling factor, would be the “observed” cross section. However, due to background contamination and reconstruction effects, further analysis is necessary to return a more realistic cross section.

7.5 Corrections to the Cross Section

Just showing the ratio of the histograms in figures 7.6 and 7.7 with the scaling factor in equation 7.8 would not produce a realistic cross section, as there are corrections that need to be applied.

The equation for the observed cross section is given by Eq. 7.4:

$$\sigma(E) \approx \frac{1}{n\delta z} \frac{N_{Int}^{TOT}(E_i)}{N_{Inc}^{TOT}(E_i)} \quad (7.9)$$

However, this equation corresponds to the true cross section only in the case where both N_{Int} and N_{Inc} are filled only by pions and if there were no inefficiencies due to reconstruction effects. Unfortunately, this is not true for LArIAT. Though filters are in place to remove as many background particles as possible, there is a contamination of muons, along with a small amount of positrons and protons. Moreover, reconstruction effects may create an inefficiency or over-efficiency in the number of entries of both histograms. In combination, these corrections provide a true cross section measurement:

$$\sigma_{True}^{\pi^+}(E_i) = \frac{1}{n\delta z} \frac{\epsilon^{Inc}(E_i)}{\epsilon^{Int}(E_i)} \frac{C_{Int}^{\pi MC}(E_i)}{C_{Inc}^{\pi MC}(E_i)} \frac{N_{Int}^{TOT}(E_i)}{N_{Inc}^{TOT}(E_i)} \quad (7.10)$$

where ϵ is the reconstruction efficiency correction for each sample, and C is the pion content for a given energy bin, informed from background subtraction studies. Because a reconstruction inefficiency ($\epsilon < 1$) corresponds to a loss of events, to correct for it requires dividing by ϵ , compared to multiplying to correct for the pion content, C . This explains why the superscripts for ϵ appear inverted.

7.5.1 Background Subtraction

A background event is defined as any WC-TPC matched track that is used in the cross section that did not come from a primary pion. There are four possibilities where this could occur:

- positrons
- muons
- secondary particles from a primary pion interacting in the beamline
- WC-TPC matched pileup track

The first and second possibilities account for inherent background due to the beam. The third possibility accounts for events that were pions in the beamline (primaries), but either decayed or interacted between WC4 and the start of the TPC, creating a secondary particle that became the

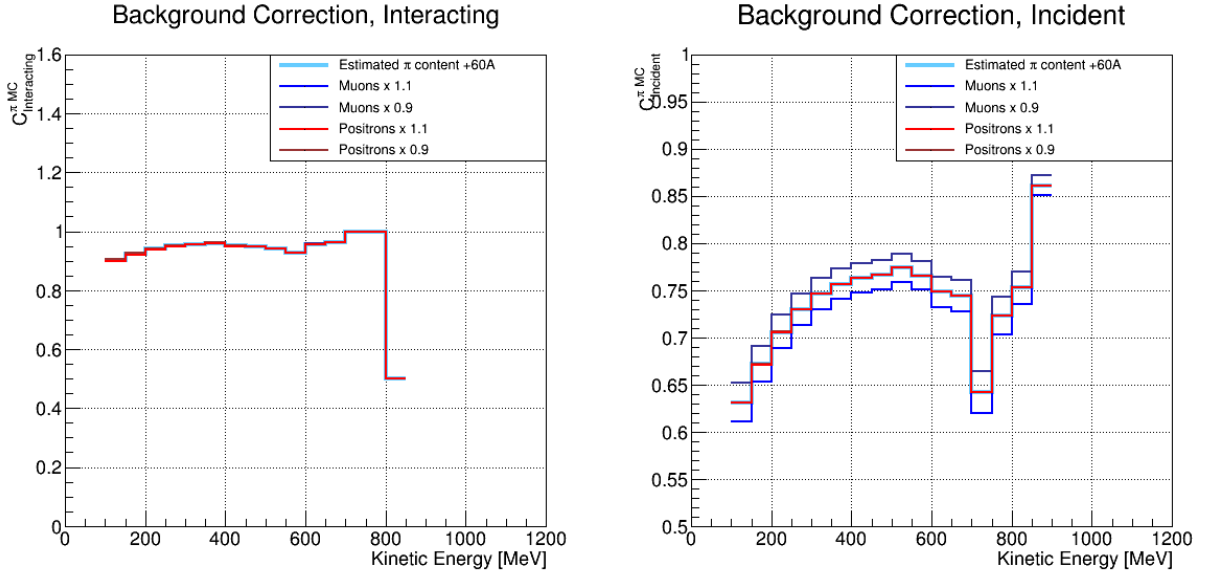


Figure 7.8: For +60 A DDMC, correction factors $C_{Int}(E_i)$ (left) and $C_{Inc}(E_i)$ (right), assuming a 10% uncertainty on the muon and positron composition.

cross section track. The final possibility accounts for the WC-TPC match algorithm choosing a pileup track as the track to match instead of the primary pion. Given the WC-TPC match requires a unique match of one TPC track to the WC track, it is unlikely this case would occur. If there was a possible match with the primary pion and another possible match with a pileup track, the event would be rejected outright. Therefore, the background due to a matched pileup track is negligible and is ignored.

We can account for the first three backgrounds using the DDMC. Using the truth information for the tracks used in the MC sample, the incident and interacting histograms can be separated by background type. Figures 7.6 and 7.7 already provide the underlying distributions for muons, positrons and pion secondaries. The primary pion content per bin can be calculated by taking the ratio of primary pion entries in that bin to the total entries in that bin, which provides the correction factor, $C(E_i)$. Figures 7.8 and 7.9 show the background correction factors, $C(E_i)$, assuming a 10% uncertainty in the muon and positron composition. The 10% uncertainty is discussed in chapter 8.

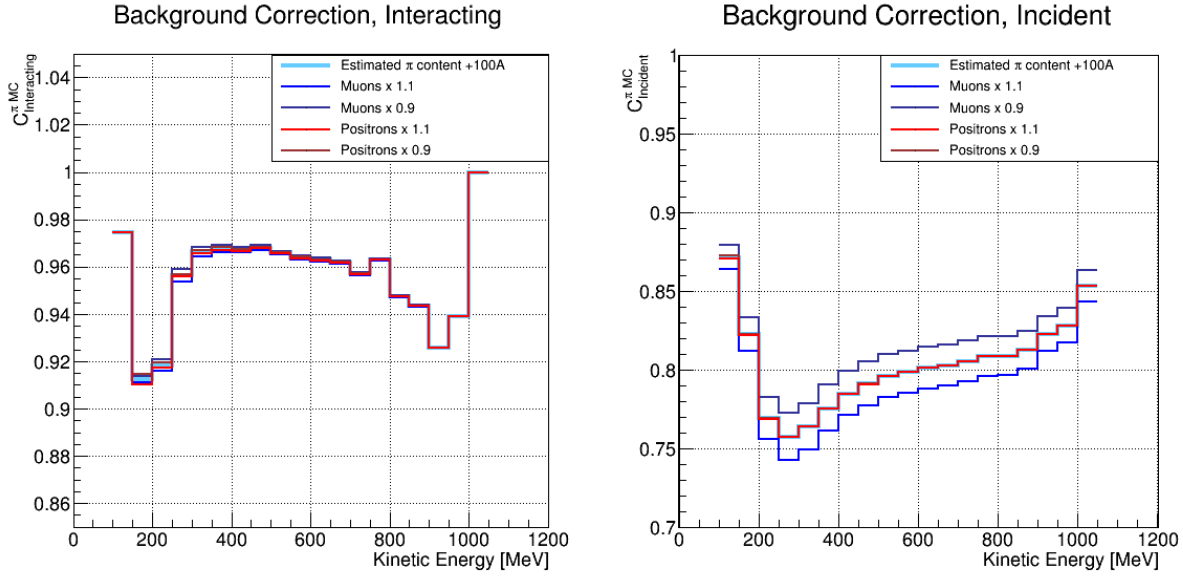


Figure 7.9: For +100 A DDMC, correction factors $C_{Int}(E_i)$ (left) and $C_{Inc}(E_i)$ (right), assuming a 10% uncertainty on the muon and positron composition.

7.5.2 Tracking Resolution and Reconstruction Efficiency

A reconstruction inefficiency occurs when the reconstruction does not terminate a track once a true interaction has occurred or terminates a track prematurely. Using the elastic scattering event from figure 1.3 as example, figure 7.10 illustrates these two cases. When the reconstruction misses the interaction (figure 7.10 left) both the incident and interacting histograms are affected. Because the interaction is tagged late, there are superfluous fills of the incident histogram, one for every point between the true interaction and the reconstructed end of the track. The interacting histogram will still be filled once, but because of the energy loss from the true interaction point to the reconstructed interaction point, the interacting histogram will be filled at a lower energy than expected. This would explain why there are entries at negative kinetic energy in the incident and interacting histograms. A similar explanation exists for the case where reconstruction stops short (figure 7.10 right). The incident histogram will now be underfilled and the interacting histogram will be filled at a higher energy than expected. Finally, there is also the possibility that the reconstruction never tags the end of the track, in which case there will be many more fills of the incident histogram, but no fill of the interacting histogram.

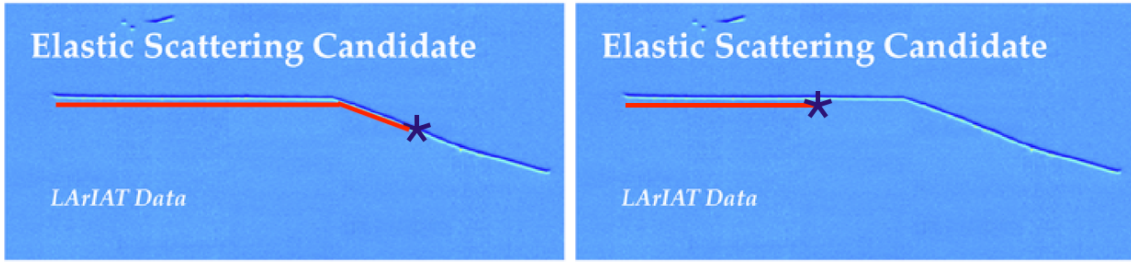


Figure 7.10: Track reconstruction missing an elastic scatter (left), which overfills the incident histogram and fills the interacting histogram at a lower energy. Track reconstruction terminating the track early (right), which underfills the incident histogram and fills the interacting histogram at a higher energy.

7.5.3 Angular Resolution

To account for this inefficiency, the first step is to understand what interaction angles can cause the reconstruction to end a track. For example, an elastic scatter of 0.1° will not be distinguishable by the track reconstruction, but a scatter of 20° should be. Using the prescription described in [18], an angular resolution can be found.

The study begins with the data and MC tracks used for the cross section analysis. Each track has associated to it a series of 3D-space points which provide a discretized view of the track trajectory. A straight line fit is applied to these points and the average distance between each space point and the fit line is calculated:

$$\bar{d} = \frac{\sum_i^N d_i}{N} \quad (7.11)$$

Note this method is similar to Eq 4.5, the only difference being Eq 4.5 uses $N-2$ in the denominator, as is necessary when applying a fit to a few points. A TPC track can have up to 240 points, which is enough sampling points to use N in the denominator. Using this as a figure of merit, we can check that the reconstruction of data tracks and MC tracks are producing similar results. Figure 7.11 compares the combined +60 A and +100 A MC and data. These plots show relatively good agreement between the two samples, which suggests track reconstruction is performing similarly on data and MC.

With that, the next step is to find the angular resolution. Figure 7.12 shows a visualization of the procedure [18]. The cross section track is separated into two halves. From the end of the first

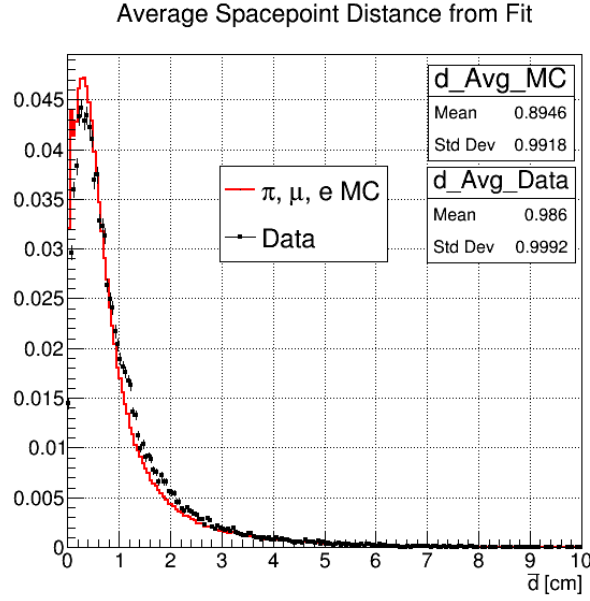


Figure 7.11: Comparison of tracking resolution between MC (red histogram) and data (black points) cross section tracks. Both +60 A and +100 A samples are combined and area normalized.

half and the beginning of the second half, four gap points are removed, for a total of eight (panel b) points. The truncated halves of the track are fit individually (panel c). Using the fit from each half, the angle between the two, α is calculated (panel d), which provides the angular resolution for the reconstruction. As this method is used on a single track, α provides how much of a “kink” can be allowed in the track without the track being broken by the reconstruction. Figure 7.13 compares the combined MC and data. Though data disagrees with MC in the trailing edge of the distribution, the mean of the distributions agree to within a degree. From the mean and deviation in each stat box, the angular resolution for data and MC is:

$$\bar{\alpha}_{Data} = 6.4 \pm 6.1^\circ \quad (7.12)$$

$$\bar{\alpha}_{MC} = 5.8 \pm 6.2^\circ \quad (7.13)$$

$$(7.14)$$

When GEANT4 simulates interactions in the detector, it has the ability to tag interactions at any angle. However, given the reconstruction cannot distinguish tracks below 5.8° , when considering true variables for the reconstruction efficiency, only interactions above this threshold should be considered. Therefore, when comparing the corrected cross section to the cross section returned by

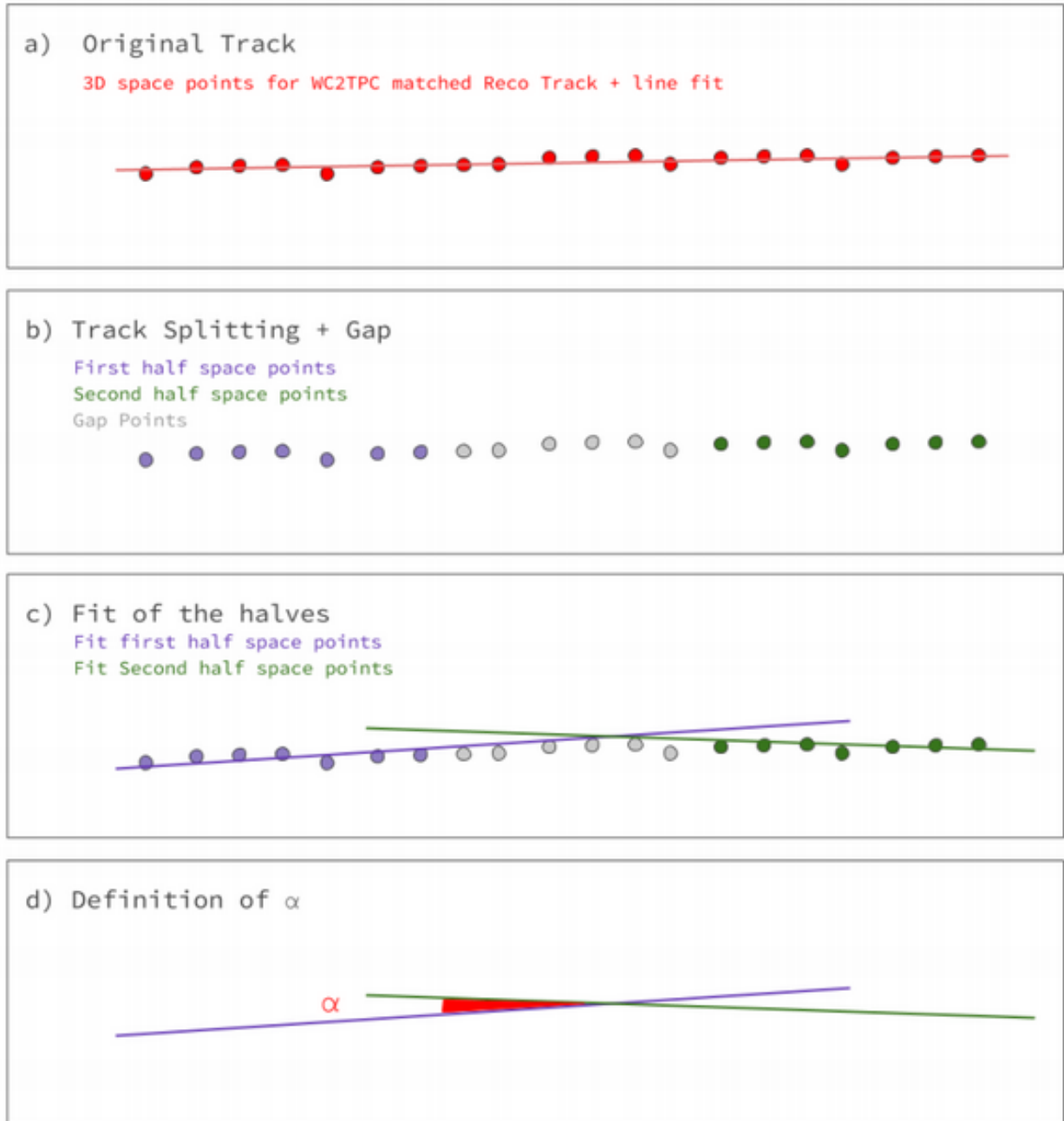


Figure 7.12: A visual diagram of the method used to find the angular resolution of the track reconstruction [18].

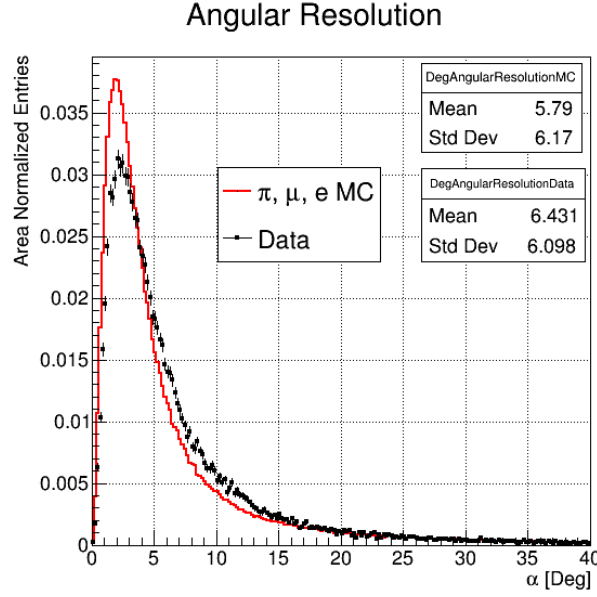


Figure 7.13: Angular resolution track by track for data (black points) and MC cross section tracks (red). Plots are area normalized.

GEANT4, similar to figure 1.4, GEANT4 events with an interaction angle greater than 5.8° should be used.

7.5.4 Defining Reconstruction Efficiency

The correction factor $\epsilon^{Int}(E_i)$ can be found using the MC cross section tracks and the GEANT4 truth information for those tracks, subject to the interaction angle being greater than the tracking resolution angle α . Using only the pion MC sample, the reconstructed interacting histogram, $N_{Int}^{\pi RecoMC}(E_i)$ is found, using the reconstructed energy deposition and defining the interaction point as the end of the reconstructed track. Using the GEANT4 information for those tracks to obtain the true energy deposition and interaction point, the true interacting histogram $N_{Int}^{\pi TrueMC}(E_i)$ is obtained for events where the true interaction angle is greater than 5.8° . The reconstruction efficiency is given by:

$$\epsilon^{Int}(E_i) = \frac{N_{Int}^{\pi RecoMC}(E_i)}{N_{Int}^{\pi TrueMC}(E_i)} \quad (7.15)$$

with a similar method for $\epsilon^{Inc}(E_i)$. The uncertainty on this correction can be estimated by varying the value of α from 0° to 5.8° and propagating into the cross section. The reconstruction efficiency

2157 corrections, $\epsilon^{Inc}(E_i)$ and $\epsilon^{Int}(E_i)$ for both the +60 A and +100 A are given in figures 7.14 and
2158 7.15, with statistical uncertainty in blue and systematic uncertainty in red.

2159 7.6 Corrected Cross Section

2160 Combining the background subtraction and the reconstruction efficiency, a cross section is obtained.
2161 Figure 7.16 shows the stats observed cross section for the combined +60 A and +100 A data
2162 samples, accounting for the background and reconstruction and efficiency corrections. Assessment
2163 and propagation of the systematic uncertainty is given in chapter 8.

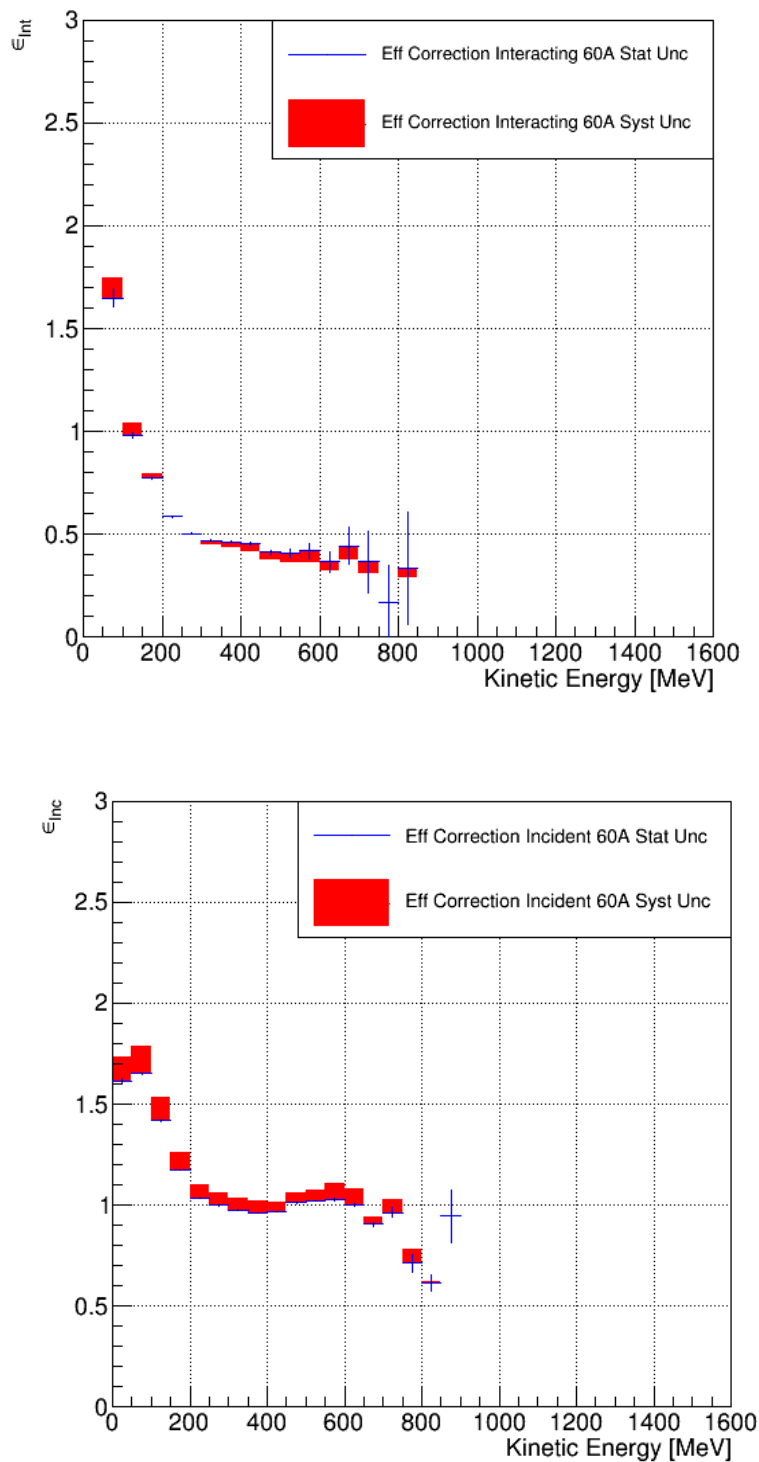


Figure 7.14: For the +60 A pion MC samples, the calculation of the reconstruction efficiency for the interacting histogram (top) and the incident histogram (bottom). For both plots, statistical uncertainty is given with blue error bars and systematic uncertainty in red shaded bars.

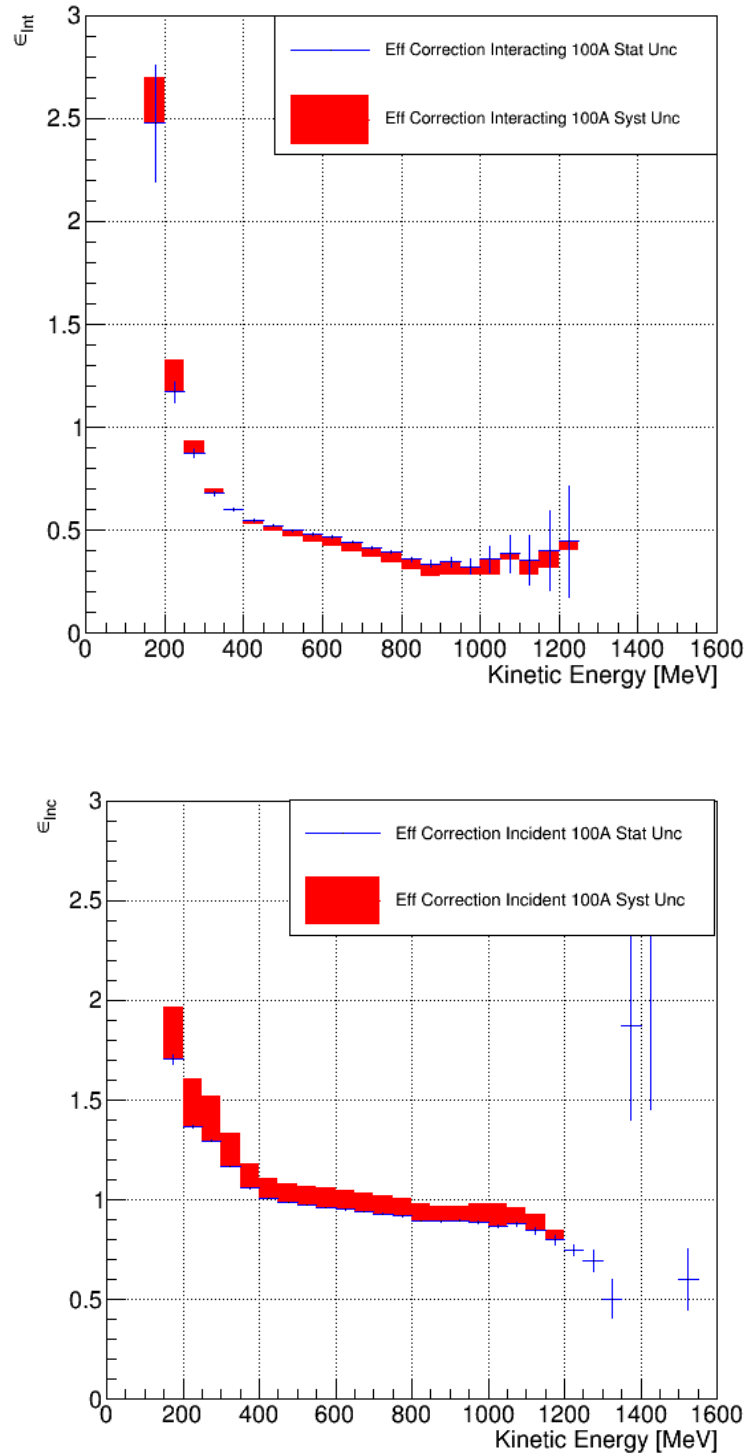


Figure 7.15: For the +100 A pion MC samples, the calculation of the reconstruction efficiency for the interacting histogram (top) and the incident histogram (bottom). For both plots, statistical uncertainty is given with blue error bars and systematic uncertainty in red shaded bars.

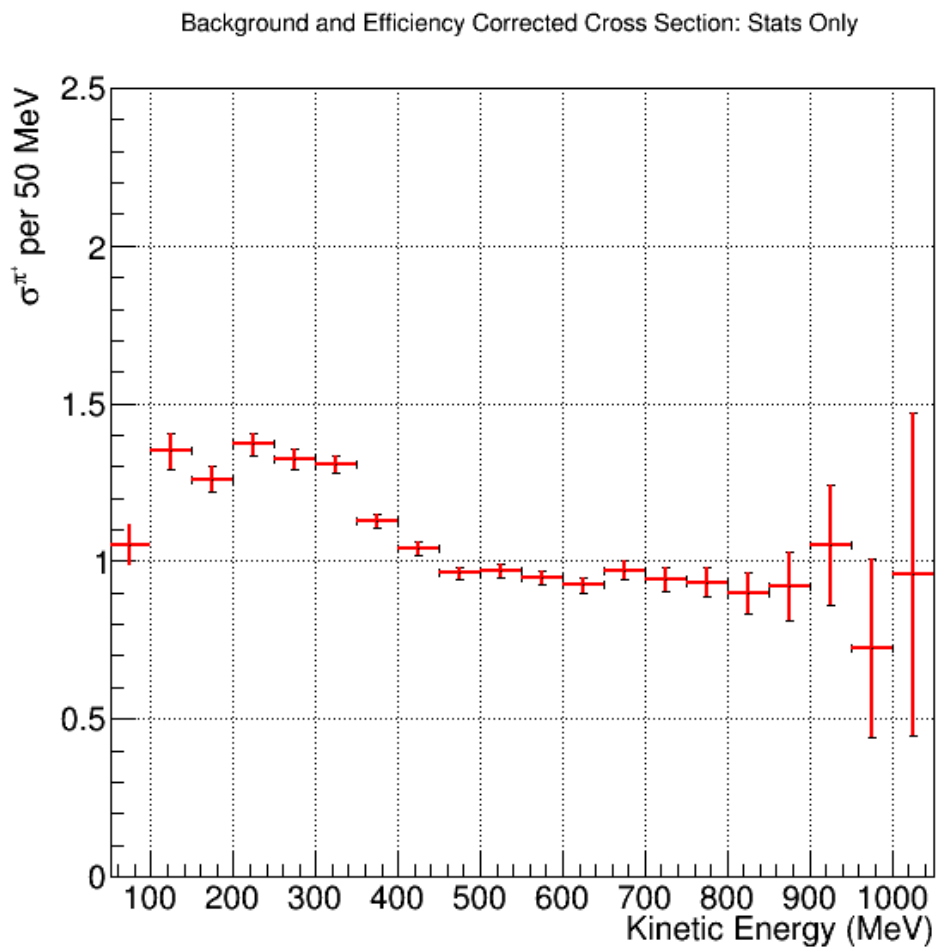


Figure 7.16: Using the background and reconstruction efficiency corrections, the combined +60 A and +100 A cross section is shown with statistical uncertainty only.

Chapter 8

Systematic Uncertainty and the Final Cross Section

This chapter assesses some of the systematic uncertainties associated with the cross section measurement. As the systematic analysis is still in progress, while some have been calculated, others are still being studied. Therefore, the systematic uncertainty given in this chapter is a lower bound; the total systematic uncertainty will increase as new sources are discovered or more fully understood. After the assessment of the systematics, the combined cross section, with statistical and systematic uncertainty is given, with a comparison to the cross section obtained from simulation.

8.1 Systematic Uncertainty

8.1.1 Uncertainty on Reconstructed Energy

For any given slice of the TPC, j , the kinetic energy of the particle entering that slice is given by:

$$KE_j = \sqrt{p_{beam}^2 + m_\pi^2} - m_\pi - E_{Loss} - E_{dep,FF-j} \quad (8.1)$$

where $E_{dep,FF-j}$ is the cumulative energy deposited in all previous slices. Therefore, the uncertainty on the kinetic energy in this slice is given by:

$$\delta KE = \sqrt{\frac{(p^2)}{p^2 + m^2}(\delta p^2) + \delta E_{Loss}^2 + \delta E_{dep,FF,j}^2} \quad (8.2)$$

The analysis assumes all events contributing to the cross section are from pions, and given the mass of the pion is known to high precision, δm_π is assumed to be zero and does not contribute to the total uncertainty. From the discussion on E_{Loss} in section 6.2, δE_{Loss} is given as 6 MeV for data, and 4 MeV for MC pions that hit the halo paddle and 3 MeV for MC pions that go through the hole in the center of the paddle. The calculation of $\delta E_{dep,FF,j}$ requires more explanation.

The energy loss up to a given slice of argon, j , is calculated by the summation of the energy loss in all previous slices:

$$E_{FF-j} = \sum_{i=0}^{i<j} E_i \quad (8.3)$$

As the energy in each slice is subtracted, and the total energy loss accumulates, the total uncertainty on the energy loss in the TPC also accumulates. To be conservative, it is assumed that the uncertainty from slice to slice are fully correlated. Therefore:

$$\delta E_{FF-j} = \sum_{i=0}^{i<j} \delta E_i = (j-1) \delta E_i \quad (8.4)$$

where δE_i is the uncertainty in the energy measurement in one slice. Figure 8.1 shows the total energy loss per slice for the +60 A and +100 A data and MC sets using a landau-gaussian convolution fit. Again, the +60 A data has a higher energy deposition than the +60 A MC, similar to figure 7.2. From the width of the landau, the uncertainty on an individual slice is 0.06 MeV for the +60 A data and 0.05 MeV for the +100 A.

8.1.2 Systematic on the Momentum

Next, an analysis of the uncertainty associated to the momentum is given. Currently, there are two known effects of the the momentum reconstruction which can lead to a systematic uncertainty.

The first effect is the uncertainty on the momentum scale. By using the time of flight, the kaons and protons from the +100 A data set can be separated. For those samples, the momentum is binned in increments of 50 MeV/c, and for those bins, using the known mass for the particle species, a fit using a modified version of equation 5.1, is applied, allowing a multiplicative scaling of the momentum and an offset in the time of flight, δt :

$$m_p = \frac{\alpha p_p}{c} \sqrt{\left(\frac{c(TOF_p - \delta t)}{l}\right)^2 - 1} \quad (8.5)$$

$$m_k = \frac{\alpha p_k}{c} \sqrt{\left(\frac{c(TOF_k - \delta t)}{l}\right)^2 - 1} \quad (8.6)$$

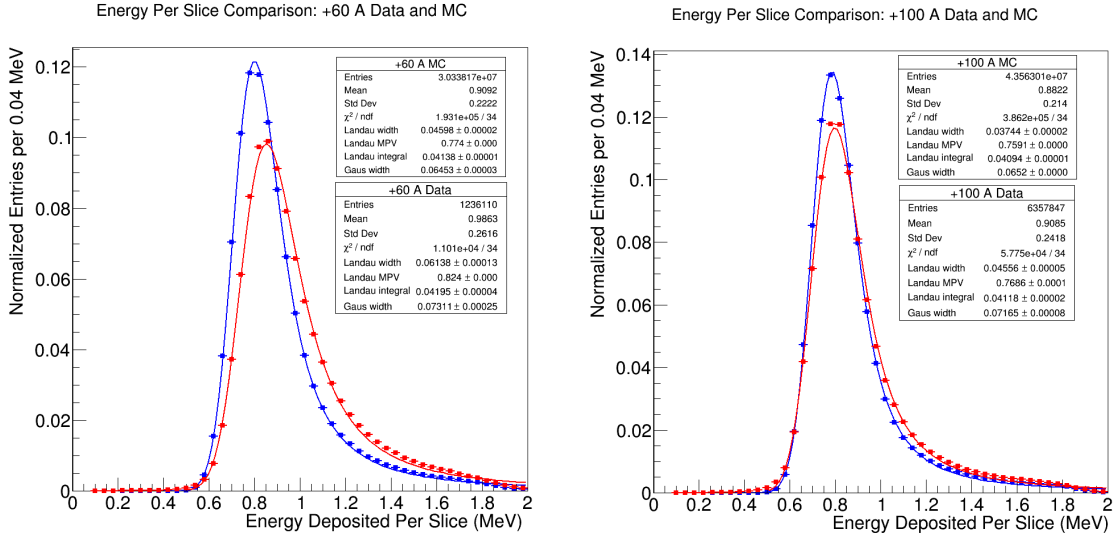


Figure 8.1: Comparison of energy loss per slice for +60 A Data and MC (left) and +100 A (right). In both plots, data is in red, and simulation is in blue, with a landau-gaussian convolved fit applied to both. Using the landau width from both plots, +60 A data has an uncertainty of 0.06 MeV per slice, and +100 A data has an uncertainty of 0.05 MeV per slice.

Using both equations, the scaling factor and offset can be found simultaneously. From the uncertainty of the fit parameter for momentum, the systematic on the momentum scale is given as 0.5%. Though not used for systematics, for reference, the TOF offset is 310 ps.

The second effect is on the hit reconstruction due to noise in the wire chambers. Noise effects are replicated in simulation by smearing the position of each hit by 2 mm. However, it is possible that the noise effects are smaller or larger than that. To account for this systematic, the smearing is changed to 1 mm and again to 3 mm. This assumes a possible uncertainty on the smearing of 1 mm. The +100 A simulation is reconstructed at 1 mm, 2 mm and 3 mm smearing. Using the reconstructed momentum distribution for each, the ratio $\frac{P_z^{3mm}}{P_z^{2mm}}$ and $\frac{P_z^{1mm}}{P_z^{2mm}}$ is calculated. These ratio plots are shown in figure 8.2, over the whole momentum range, the high statistics range of 600-1000 MeV/c, and a rebinning of the high stats region into 40 MeV/c bins to reduce the statistical fluctuations. Though there are large statistical uncertainty bars for these plot, most values are within 1% of the nominal value. Therefore, a systematic of 1% on the momentum is applied.

These two systematics, 0.5% from the momentum scale, and 1% from the hit misreconstruction

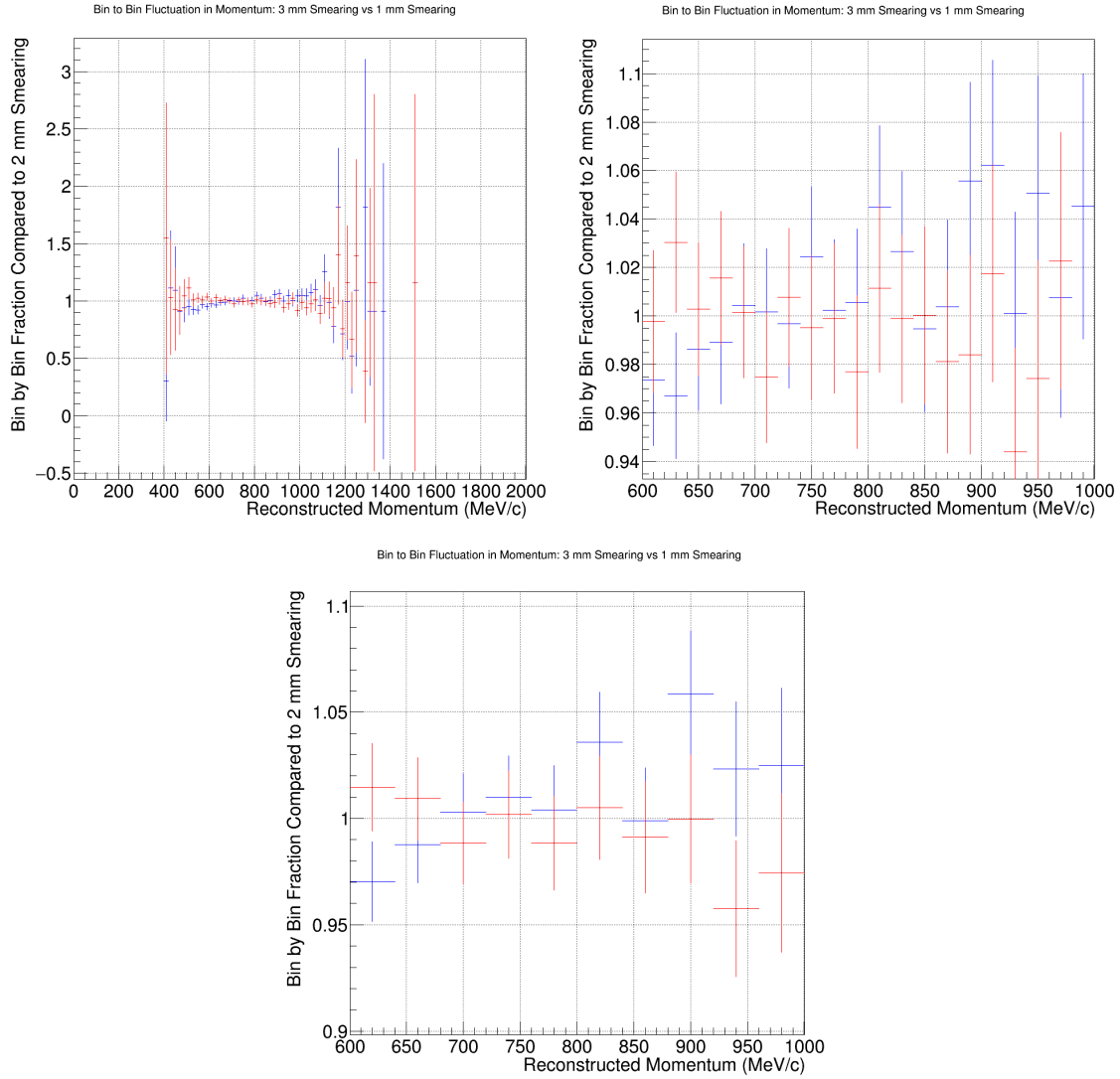


Figure 8.2: Using a 1 mm (red) and 3 mm smearing (blue), the ratio of the momentum plots of each relative to the nominal 2 mm smearing over the entire range (top left), in the high statistics region (top right), and in the high statistics region with $40 \frac{\text{MeV}}{c}$ bins (bottom).

due to noise are assumed to be non-correlated, and therefore combine in quadrature:

$$\delta p = \sqrt{(0.005p)^2 + (0.01p)^2} = 0.011p \quad (8.7)$$

With that, we can complete the measurement for the uncertainty on the kinetic energy. The uncertainty at a given slice is given by:

$$\delta KE_j = \sqrt{\frac{p^2}{p^2 + m_\pi^2} (0.011p)^2 + (6 \text{ MeV})^2 + (j - 1)^2 (0.06 \text{ MeV})^2} \quad (8.8)$$

This is propagated into the analysis by varying the KE_j at each slice by this amount. N_{Int} , N_{Inc} and the cross section are calculated in three cases: using the nominal measurement of KE_j , then with $KE_j + \delta KE_j$, and finally with $KE_j - \delta KE_j$. Using the difference between the maximum and minimum of these three values, bin to bin, determines the systematic uncertainty. Figures 8.3 and 8.4 show the energy systematics for the +60 A and +100 A data cross section tracks, using a 1.1% systematic in momentum, 6 MeV systematic from the energy loss, and 0.06 MeV/slice for the +60 A and 0.05 MeV/slice systematics for the +100 A.

8.1.3 Systematic on Beamline Composition

Part of obtaining the cross section plot in figure 7.16 is an understanding of how much of the data cross section is from background species. This is dependent on how well the beamline composition is known, as each species fills the cross section plots differently. Though there have been multiple studies to calculate a systematic on the beamline composition, no robust method has been formulated. However, there are some studies which can suggest what range this systematic might be. For example, from the discussion of figure 6.18, there is approximately a 10% false rate of +60 A protons due to TOF accidentals, suggesting a proton analysis would have about a 10% uncertainty from these accidentals.

Another gauge of the systematics is on the muon content. As muons are the primary background, given the event reduction in table 6.4, the uncertainty on the muon content will have the largest effect on the composition systematic. The WCQuality cut from 6.11, and the residual cut from 6.9, particularly affects muons. As most muons in the beam come from pion decay, the change in trajectory of the muon from the decay can affect the midplane projections and the residual fitting, as the decay will produce a kink in the trajectory and skew these calculations.

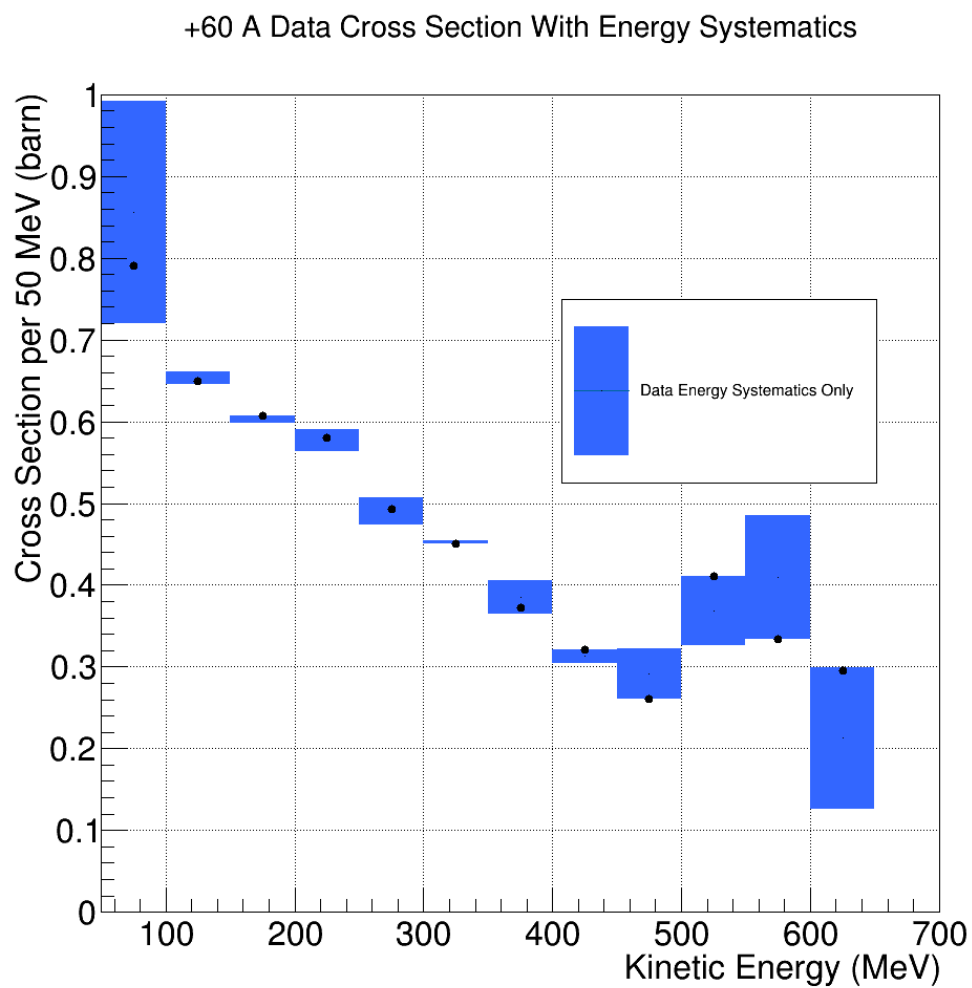


Figure 8.3: Energy systematics for +60 A data in black points with energy systematics in blue uncertainty bars.

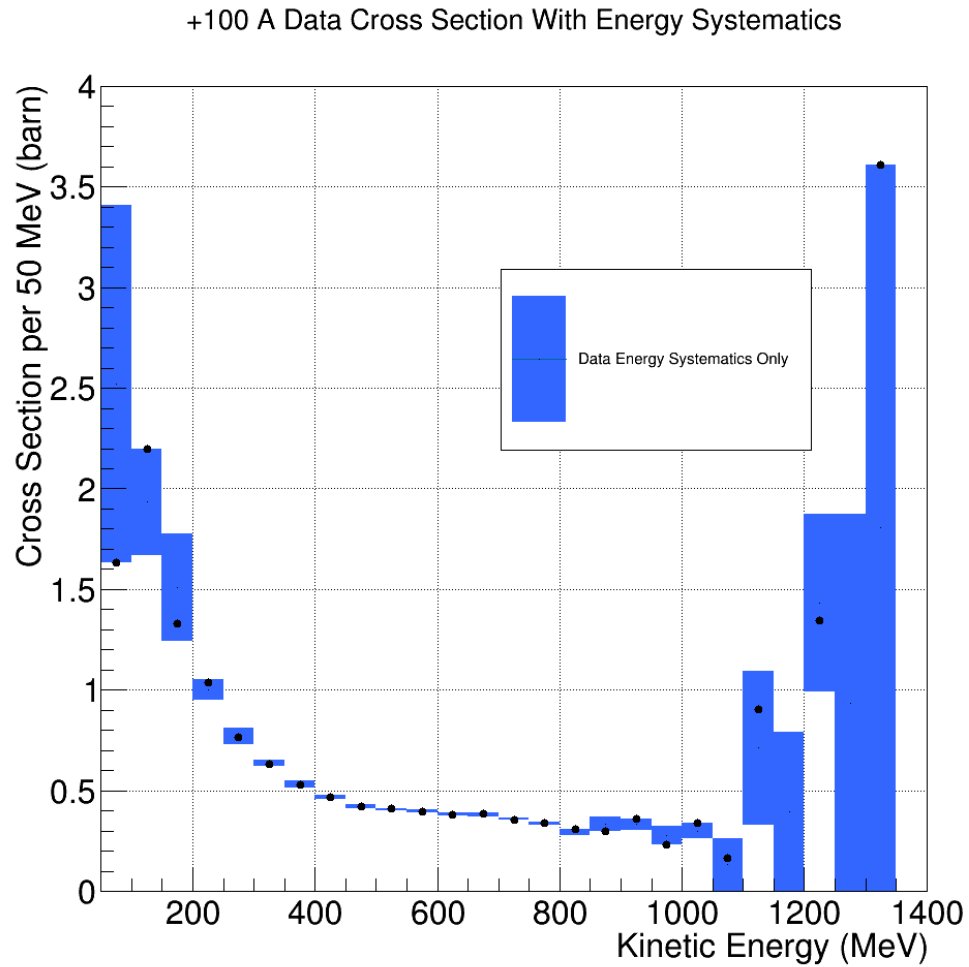


Figure 8.4: Energy systematics for +100 A data in black points with energy systematics in blue uncertainty bars.

Particle Species/Cut	π	proton	μ	positron
Nominal Cut	62.2%	25.8%	5.6%	5.9%
Loose Cut	61.7%	25.6%	6.1%	5.9%
Tight Cut	62.8%	25.5%	5.1%	5.9%
Relative Deviation	1%	0.8%	9%	0%

Table 8.1: Using 3 mm as a test case, the change in global particle composition for +100 A simulation by changing the cut value for the residual and WCQuality cuts.

Therefore, a shift in the cut values used for the residual and midplane match can change the muon composition and introduce a systematic. Though knowing exactly how much of a shift to allow is still being studied, using a test value of 3 mm with the +100 A beamline composition sample can illustrate the effect. Moreover, as the underlying simulated and data distributions disagree, particularly in the ΔX and residual variables, varying the cut values can gauge the effect of this disagreement.

The nominal value for the residual cut for a WC track is 12 mm, and the midplane match cut is 15 mm for both the X and Y cuts, and produces a nominal muon content of 5.6%. By tightening and loosening the cuts by 3 mm and comparing the global content of each species, a measure of the systematic due to these cuts can be accessed. From table 8.1, though other particle species are not greatly affected by a change in cut values, the muon content varies on the order of 10%, implying a 10% systematic on the muon contamination. This explains why a 10% systematic was used in figures 7.8 and 7.9.

8.2 Final Cross Section

With the systematics from section 8.1, figure 7.16 can be updated to include the systematic uncertainty. Figures 8.5 and 8.6 show the cross section for the +60 A and +100 A samples, respectively.

When comparing the +60 A and +100 A cross sections in 8.5 and 8.6 in the kinetic energy range where both have statistics, a disagreement arises. Figure 8.7 overlays the cross sections in

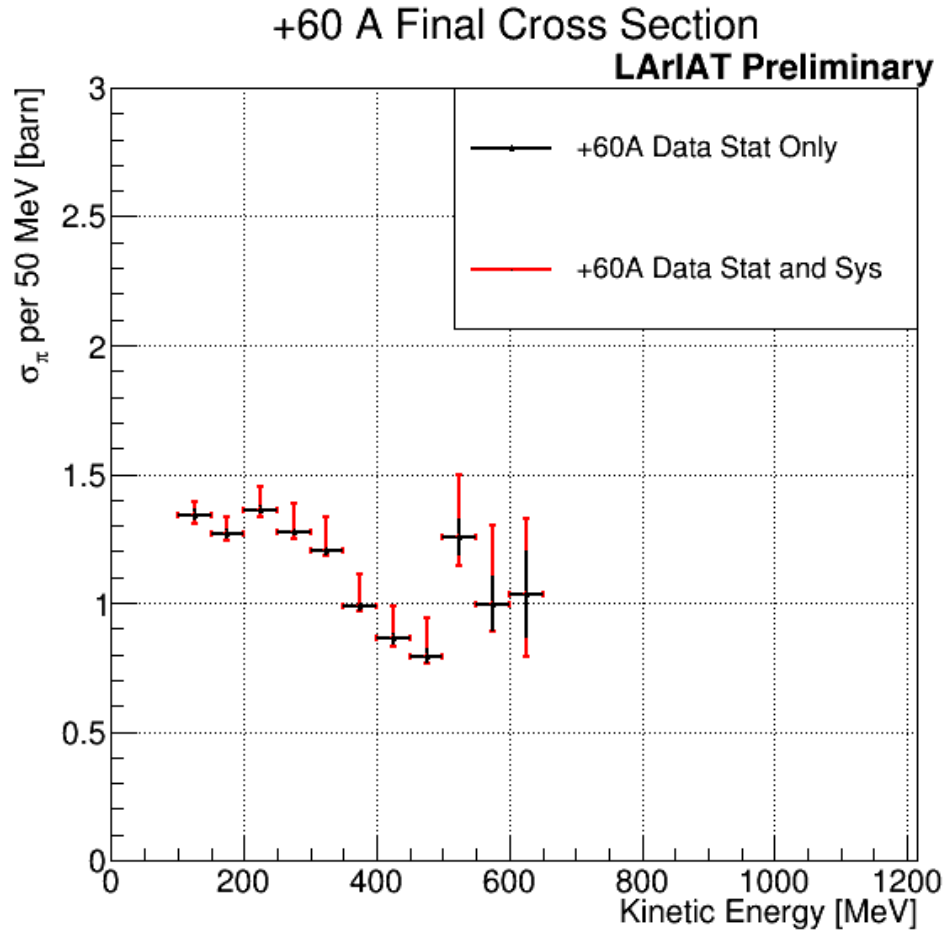


Figure 8.5: With background corrections, efficiency corrections and systematics applied, the +60 A cross section, with statistical uncertainty in black and statistical and systematic uncertainty in red.

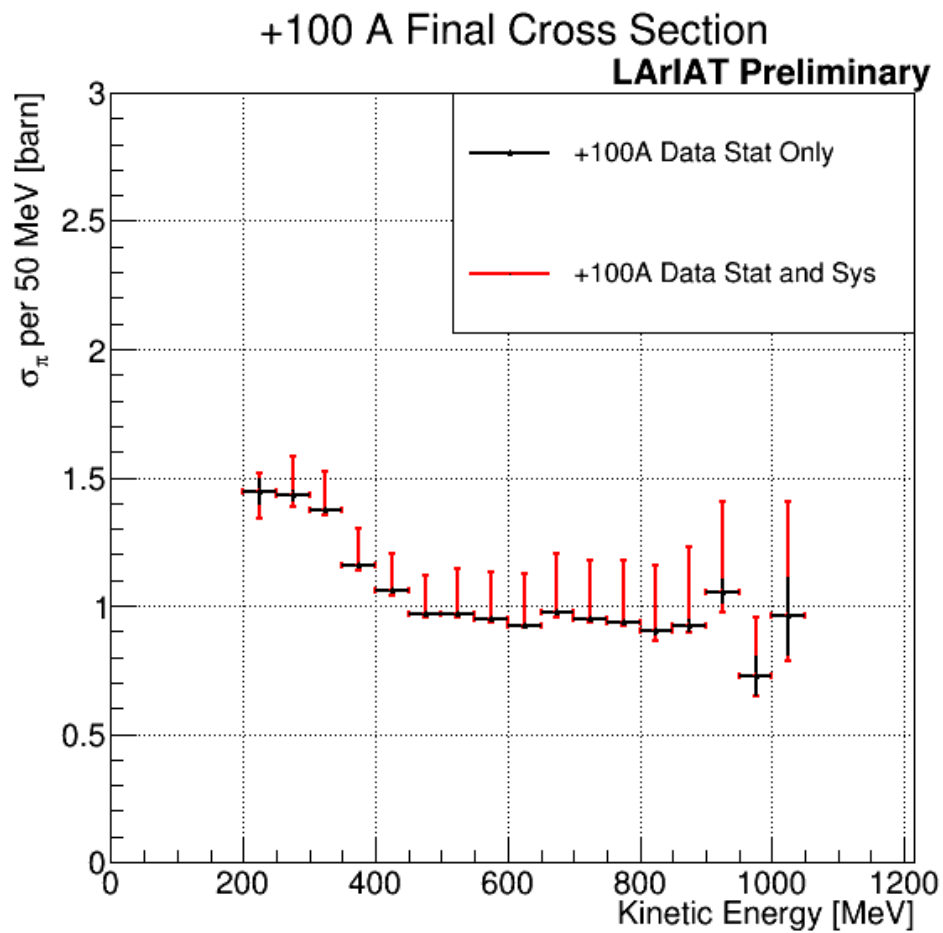


Figure 8.6: With background corrections, efficiency corrections and systematics applied, the +100 A cross section, with statistical uncertainty in black and statistical and systematic uncertainty in red.

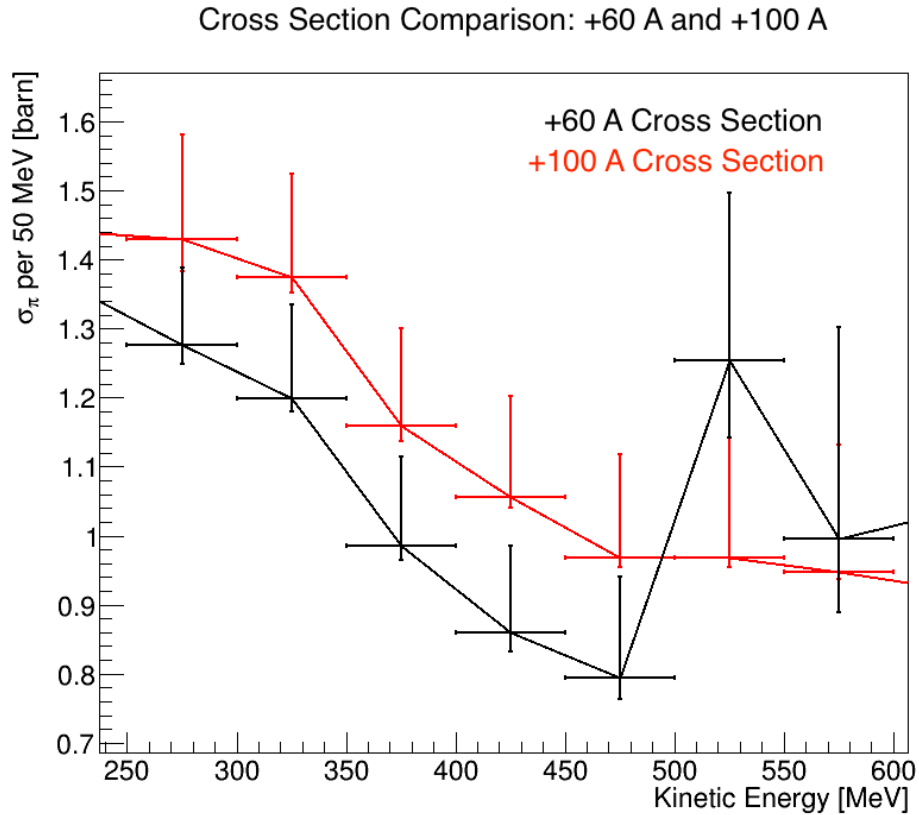


Figure 8.7: For the energy range where both samples overlap, the +60 A cross section (black) and +100 A cross section (red), both with stats and systematic uncertainty.

the energy range of 250-600 MeV. In the overlapping energy range, these cross section should agree. However, the +100 A cross section is about 20% higher than the +60 A cross section in these bins. Further analysis is needed to understand this discrepancy.

With both +60 A and +100 A cross section, a comparison can be made to the true cross section, as returned by GEANT4, subject to the angular resolution cut of 5.8° discussed in 7.5.4. Combining both samples, along with the systematics, the total π^+ -Ar cross section, with GEANT4's assumed cross section is shown in figure 8.8.

From this figure, the data is systematically higher than the predicted cross section returned from GEANT4, on the order of 20 %. The +100 A sample provides more than 80% of the events for the cross section (table 5.1), and from figure 8.7, the +100 A data returns a larger cross section. This suggests the +100 A data has some currently unknown effect that is inflating the cross section, while the +60 A data would agree better with the GEANT4 cross section.

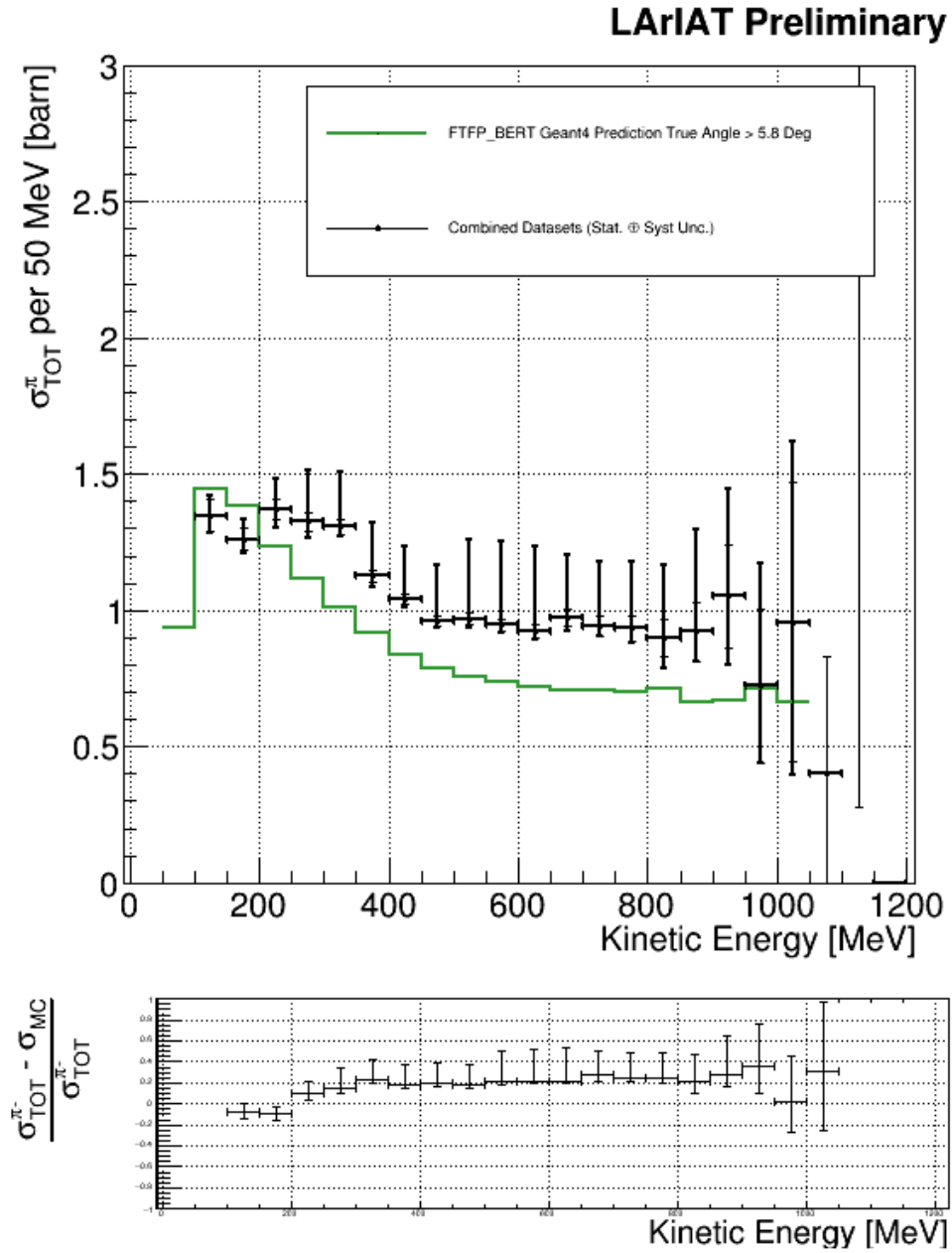


Figure 8.8: Top: Combining the +60 A and +100 A cross sections in figures 8.5 and 8.6, the total π^+ -Ar combined cross section is given in black with stats and systematic uncertainty, with GEANT4 prediction in green for interaction angles greater than 5.8° . Bottom: Comparing the two cross sections, the residual is given.

2271 It is possible the beamline composition for the +100 A sample is not an accurate reflection
2272 of the data. For example, using the DDMC event reduction rates for the various species and
2273 assuming data had similar particle rates, data suggests the proton contamination was negligible
2274 and only background from muons and positrons need to be considered. If this assumption is false,
2275 and there is a significant proton contamination in the cross section, even after the proton filter,
2276 then a significant proton contamination should be added as part of the background subtraction.
2277 Those protons in data but not in the DDMC will inflate the data cross section, as protons have a
2278 higher cross section. Similarly, if there are fewer muons in data than the DDMC suggests, the data
2279 cross section will also be inflated, given muons do not interact as often as pions.

Chapter 9

Conclusions and Future Improvements

The goal of this analysis is to measure a π^+ -LAr cross section, and provide a comparison to the predicted cross section as returned from GEANT4. From figure 8.8, the data used for this analysis disagrees with the predicted GEANT4 cross section, with the data cross section being 10-20% greater than that predicted by GEANT4.

This analysis provides upgrades from previous results from LArIAT. Using a high yield WC Track reconstruction over a picky track WC track reconstruction allows approximately a 50% increase in the available events for a cross section measurement. A more rigorous beamline simulation capable of better representing data-taking conditions, as well as being able to reconstruct high yield tracks lowered the overall beamline systematic from 100% on muons and positrons to approximately 10%.

Aside from a completed analysis of the systematics, there are still other upgrades to this analysis that could be implemented with further study. Moving from a picky track WC reconstruction to a high yield WC reconstruction comes with an increase in statistics, but a lower quality of some tracks. This is evident in figures 6.9 and 6.11. From those figures, there are still data based effects which are not yet understood and implemented into the simulation. Studying the timing information within the WCs may provide a way to, if not uniquely match hits across WCs, at least reduce the possible combinations of hits by rejecting hits that are well separated in time, even within the uncertainty introduced by clock drift. This should improve overall the quality of WC tracks.

For beamline simulation, most of the differences when compared to data can be explained by the variable intensity of the beam being sent from the accelerator. In particular, the TOF accidentals present in data but not replicated in simulation. For protons, this effect is significant in creating background events. The effect on pions is unknown, and makes placing a systematic on the mass cut difficult, as the simulated TOF cannot currently be brought into agreement with data. Data suggests the mass cut works well enough to make protons a negligible background, but confirming that in simulation would be beneficial. This is especially true if the disagreement between the data and GEANT4 cross sections is due to excess protons in the data sample.

The process for the energy calibration to convert charge on a wire to an energy deposition, while momentum dependent, should produce similar results when compared across the same momentum range. This is true for the MC energy deposition, where the landau MPV between +60 A and +100 A agree within 2%. Moreover, +100 A data agrees with the +100 A MC, with the same tolerance. However, the +60 A data has a 6% disagreement with the +60 A MC. Further study into the energy reconstruction is necessary to understand and correct this difference.

In conclusion, this analysis provides a π^+ -LAr cross section over the kinetic energy range of 50-1050 MeV. Bin by bin, the data cross section is consistently larger than the GEANT4 predicted cross section, with a larger disagreement in the region where the +100 A events dominate. There is also disagreement between the +60 A and +100 A data cross sections in the energy range both samples probe, suggesting further study is necessary in the reconstruction of each sample and the beamline composition that informs the background subtraction method. Finally, a more complete systematics analysis is needed to account for other unknown uncertainties.

Bibliography

- [1] [ATLAS collaboration], G. Aad *et al.*, Phys. Lett. **B716**:1–29 (2012). [arXiv:1207.7214]
- [2] D. Griffiths, *Introduction to Elementary Particles*, Wiley (2008).
- [3] C. Anderson *et al.*, JINST **7**:P10019 (2012). [arXiv:1205.6747]
- [4] [DUNE collaboration], A. Tonazzo, SciPost Phys. Proc. **1**:043 (2019).
- [5] [ArgoNeuT collaboration], R. Acciarri *et al.*, JINST **8**:P08005 (2013). [arXiv:1306.1712]
- [6] [Particle Data Group collaboration], M. e. a. Tanabashi, Phys. Rev. D **98**:030001, <https://link.aps.org/doi/10.1103/PhysRevD.98.030001> (2018).
- [7] B. T. Cleveland, T. Daily, R. Davis, Jr., J. R. Distel, K. Lande, C. K. Lee, P. S. Wildenhain, and J. Ullman, Astrophys. J. **496**:505–526 (1998).
- [8] [Super-Kamiokande collaboration], Y. Fukuda *et al.*, Phys. Rev. Lett. **81**:1562–1567 (1998). [arXiv:hep-ex/9807003]
- [9] C. Giganti, S. Lavignac, and M. Zito, Prog. Part. Nucl. Phys. **98**:1–54 (2018). [arXiv:1710.00715]
- [10] [LSND collaboration], C. Athanassopoulos *et al.*, Phys. Rev. Lett. **81**:1774–1777 (1998). [arXiv:nucl-ex/9709006]
- [11] [MiniBooNE collaboration], A. A. Aguilar-Arevalo *et al.*, Phys. Rev. Lett. **110**:161801 (2013). [arXiv:1303.2588]
- [12] S. Pascoli, S. T. Petcov, and A. Riotto, Nucl. Phys. **B774**:1–52 (2007). [arXiv:hep-ph/0611338]

- [13] A. Cervera, A. Donini, M. B. Gavela, J. J. Gomez Cadenas, P. Hernandez, O. Mena, and S. Rigolin, Nucl. Phys. **B579**:17–55, [Erratum: Nucl. Phys.B593,731(2001)] (2000). [arXiv:hep-ph/0002108]
- [14] C. Jarlskog, Z. Phys. **C29**:491–497 (1985).
- [15] J. A. Formaggio and G. P. Zeller, Rev. Mod. Phys. **84**:1307–1341 (2012). [arXiv:1305.7513]
- [16] D. Casper, Nucl. Phys. Proc. Suppl. **112**:161–170, [161(2002)] (2002). [arXiv:hep-ph/0208030]
- [17] A. S. Carroll, I. H. Chiang, C. B. Dover, T. F. Kycia, K. K. Li, P. O. Mazur, D. N. Michael, P. M. Mockett, D. C. Rahm, and R. Rubinstein, Phys. Rev. **C14**:635–638 (1976).
- [18] E. Gramellini, *Measurement of the Negative Pion and Positive Kaon Total Hadronic Cross Sections on Argon at the LArIAT Experiment*, Ph.D. thesis, Yale U., <http://lss.fnal.gov/archive/thesis/2000/fermilab-thesis-2018-24.pdf> (2018).
- [19] D. H. Wright and M. H. Kelsey, Nucl. Instrum. Meth. **A804**:175–188 (2015).
- [20] D. R. Nygren, eConf **C740805**:58 (1974).
- [21] H. J. Hilke, Rept. Prog. Phys. **73**:116201 (2010).
- [22] C. Rubbia (1977).
- [23] G. Jaffe, Ann. Phys. **42**:303 (1913).
- [24] J. B. Birks, Proc. Phys. Soc. **A64**:874–877 (1951).
- [25] J. Thomas and D. A. Imel, Phys. Rev. **A36**:614–616 (1987).
- [26] M. Mooney, *Proceedings, Meeting of the APS Division of Particles and Fields (DPF 2015): Ann Arbor, Michigan, USA, 4-8 Aug 2015* (2015).
- [27] E. Morikawa, R. Reininger, P. Gütler, V. Saile, and P. Laporte, **91**:1469–1477 (1989).
- [28] B. J. P. Jones, *Sterile Neutrinos in Cold Climates*, Ph.D. thesis, MIT, <http://lss.fnal.gov/archive/thesis/2000/fermilab-thesis-2015-17.pdf> (2015).

- [29] N. Ishida, M. Chen, T. Doke, K. Hasuike, A. Hitachi, M. Gaudreau, M. Kase, Y. Kawada, J. Kikuchi, T. Komiyama, K. Kuwahara, K. Masuda, H. Okada, Y. Qu, M. Suzuki, and T. Takahashi, Nuclear Instruments and Methods in Physics Research Section A: Accelerators, Spectrometers, Detectors and Associated Equipment **384(2)**:380 – 386, <http://www.sciencedirect.com/science/article/pii/S0168900296007401> (1997).
- [30] W. M. Burton and B. A. Powell, Appl. Opt. **12(1)**:87–89, <http://ao.osa.org/abstract.cfm?URI=ao-12-1-87> (1973).
- [31] V. M. Gehman, S. R. Seibert, K. Rielage, A. Hime, Y. Sun, D.-M. Mei, J. Maassen, and D. Moore, Nuclear Instruments and Methods in Physics Research A **654**:116–121 (2011). [arXiv:1104.3259]
- [32] B. Baller, *Trajcluster User Guide*, <https://cdcv.s.fnal.gov/redmine/documents/1026> (2018).
- [33] M. A. Leigui de Oliveira, *Expression of Interest for a Full-Scale Detector Engineering Test and Test Beam Calibration of a Single-Phase LAr TPC*, Tech. Rep. CERN-SPSC-2014-027. SPSC-EOI-011, CERN, Geneva, <https://cds.cern.ch/record/1953730>, a formal spokesperson has not yet been selected. In the interim Thomas Kutter serves as the official contact person. (2014).
- [34] [LArIAT collaboration], F. Cavanna, M. Kodorsky, J. Raaf, and B. Rebel <https://arxiv.org/pdf/1406.5560.pdf>, in preparation for submission to JINST (2019).
- [35] H. Fenker, *A Standard Beam PWC for Fermilab* (1983).
- [36] M. Adamowski *et al.*, JINST **9**:P07005 (2014). [arXiv:1403.7236]
- [37] G. De Geronimo *et al.*, IEEE Trans. Nucl. Sci. **58**:1376–1385 (2011).
- [38] C. J. Z. M. Berger, M.J. and J. Chang, *ESTAR, PSTAR, and ASTAR: Computer Programs for Calculating Stopping-Power and Range Tables for Electrons, Protons, and Helium Ions (version 1.2.3). [Online]*, <http://physics.nist.gov/Star>, accessed Apr 15, 2019 (2005).